Laser Induced Fluorescence Studies of Dispersion by Breaking Waves

Alan E Marson

A thesis submitted in fulfilment of the requirements

for the degree of Doctor of Philosophy

The University of Edinburgh

2004

Abstract

The technique of Planer Laser Induced Fluorescence (PLIF) was applied to investigate the dispersion of surface films by breaking waves. The mixing caused by both isolated single breaking waves and pairs of identical breaking waves was examined. The results have a direct application to the study of dispersion of surface pollutants in the sea.

PLIF was used to obtain images of the concentration distribution of a dispersing methanol-rhodamine solution used to mimic a surface film. Experiments were carried out on seven different non-dimensional amplitudes of single breaking wave and three different non-dimensional amplitide of pairs of breaking waves, ranging from mild spilling to large plunging breakers. Spatial and temporal information was extracted from the recorded images in order to quantify the dispersion in terms of maximum depth reached, area covered, centre of mass motion, dispersion coefficents and fractal dimension of the water-dye boundary.

The result expanded significantly upon, and compared favourably with, previous work carried out on isolated single breaking waves.

Declaration

I do hereby declare that this thesis was composed by myself and that the work described within is my own, except where explicitly stated otherwise.

Acknowledgements

I would like to thank my supervisor Professor Clive Greated for his continual support, help and ability to raise my spirits. Thanks also to Ted Schlicke for helping me get started and solving all my C problems; Frank Morris for helping to set up and repair all the equipment, as well as keeping things in perspective for me and Dawn Rippener for providing a sympathetic ear and invaluable advice. I would also like to thank the rest of the Acoustics and Fluid dynamics group for generally helping me complete this research.

A special thank you to my family: my parents for allowing me the freedom to achieve everything I have; my brother James for his more than welcome distractions; My uncle Alec, and Pat, for providing breaks in the country, and my grandmother and late grandfather for their never wavering faith in my abilities.

My final and most important thanks go to my wife, Moira. Without her support I would never have been able to complete my work and I cannot express how grateful I am for her love. She also writes my acknowledgements.

Contents

List of Figures

List of Tables

Nomenclature

Chapter 2

λ	Wavelength
f	Frequency
H	Local wave height
a	Wave amplitude
k	wavenumber, $\frac{2\pi}{\lambda}$
MWL	Mean Water Level
η	Free surface elevation
SWL	Still Water Level
ω	Angular frequency, 2πf
h	Local water depth
d	Still water depth
ak	Non-dimensional wave slope
β	Beach slope
ϕ	Velocity potential
σ	Surface tension
C	Phase Speed
ρ	Density (water)
A	Surface area
ϵ	Surface dilation modulus
δ	Width of viscous surface layer
μ	Kinematic viscosity

	Chapter 3	
$\mathbf{u}$		Fluid velocity
μ		Coefficient of viscosity
LDA		Laser Doppler Anemometry
HWA		Hot Wire Anemometry
PIV		Particle Image Velocimetry
(P)LIF		(Planar) Laser Induced Fluorescence
f_c		Central frequency of breaking wave packets
Δf		Frequency spread of breaking wave packets
CCD		Charge Coupled Device
	Chapter 4	
λ		Wavelength of light
	Chapter 5	
$m_{i,j,k}$		Moment
$\mathbf{q}$		Mass flux
C		Concentration gradient
D		Diffusion coefficent
M		Total diffusing mass
σ		Standard deviation (size of dispersion cloud)
H		Hurst exponent
	(Section 5.6)	
D		Dimension
n		Number of split pieces used to calculate D
r		Reduction in size of each piece
s		Side length for box-counting dimension
	Chapter 6	
C.o.m.		Centre of mass

Chapter 1

Introduction

All life on Earth depends on water. Whether for cleaning, drinking or living in, water is essential for survival. However, every day more and more pollution is released into environment [65, 66]. Pollution takes many forms: human waste, oil, detergents, chemicals, even nutrients such as nitrogen and phosphorus [34].

Large-scale oil spills, such as the Exxon Valdez disaster in 1989 and Braer in 1993, attract a large amount of publicity and do a massive amount of damage to the environment. However, accidents such as these contribute only a small percentage of the total oil pollution in the oceans. A Smithsonian Institution travelling exhibition in 1995 reported that 706 million gallons of oil enter our oceans each year [71], of which only 37 million, just over 5%, actually comes from large oil spills. Over half comes from simply being washed down the drain.

Other forms of pollution, such as human waste and detergents, often used to disperse spills as well as in everyday life, cause environmental damage. Man-made products which do not degrade naturally or harmlessly are constantly being introduced into the oceans, and power stations and industry can produce heat pollution which can affect the ecosystem if not carefully controlled and monitored [33].

It is said that "The solution to pollution is dilution" [69]; by spreading any pollutant, the effect on the environment can be reduced. However, when chemicals enter the food chain the process of biomagnification by repeated predation can cause concentrations to rebuild, such as the devastating effect of DDT on bird of prey populations first noticed by Derek Ratcliff in 1967 [53].

A lot of the pollution released into the environment goes unseen, and can only be detected by specialist equipment. One of the forms of pollution that can be seen are surface films. Chemicals known as surfactants (short for surface active agents) will form on the water's surface and, by damping the shorter, rougher, surface waves, make the surface smoother and reflect more light. These films can be seen in ports, harbours and shipping lanes, but the main cause of surfactants is natural biodegrading [84].

These films will spread largely undisturbed on the surface of the water unless broken by a passing ship, breaking wave or rain. In this Thesis, the mixing effect of breaking waves is considered, with particular reference to how the size of the

wave affects the dispersion.

1.1 Aim and Contents of Thesis

The aim of this work was to examine the dispersion of a surface film caused by breaking waves of different sizes. This research differed from previous work as a comparison was made between single and double breaking waves and a wider range of breakers has been examined.

The specific objectives of the research were to look in greater detail at the dispersion of surface films by single breaking waves, covering a wider range of amplitudes and placing more emphasis on obtaining relationships between amplitude and dispersion parameters and, for the first time, to examine the effect of a second breaking wave on the mixing process, in specific whether it resulted in a significant change to the parameters measured for the single breaking wave.

The work in this Thesis is split into 2 parts: discussion of theory and introduction of experimental method in chapters 2 to 5, and then results and conclusions in chapters 6 to 8, starting with the single breaking wave results followed by those for the double breaking wave.

Chapter 2 gives a description of the properties of water and the formation of water waves. A mathematical description of wave motion is presented with reference to phase and group speed of waves. Classification of breaker type is

explained with a review of previous work carried out studying breaking waves and mixing of surface films. Finally, the formation and dispersion of surface films are discussed.

In Chapter 3, the experimental facilities used at The University of Edinburgh are reviewed. Details of the wave flume, wave generation, laser illumination, lightsheet formation and cameras used to record the experiment are given. The chapter ends with a presentation of the experimental set-up.

Chapter 4 describes the theory of Planar Laser Induced Fluorescence and why it was chosen for these experiments. An outline of the technique is provided followed by the specific application to this research. The limitations and important considerations are also discussed. Finally in chapter 4, the steps necessary to process the raw data before analysis are explained.

The method of analysis and calculating results from the experimental data is discussed in chapter 5. This looks at, in turn, depth reached by the dispersing film, area covered by the dispersing film, the centre of mass motion, dispersion and fractal dimension.

Chapter 6 contains the results and analysis for the single breaking wave experiments. A qualitative description of the dispersion of a surface film by a breaking wave is presented followed by a discussion of the amplitudes used. The results are then presented for the maximum depth, area, centre of mass motion, dispersion

and fractal dimension for a range of breaking waves.

A similar analysis for the second breaking wave experiments is found in chapter 7. The results for the same parameters over a wider sample of spilling breakers is presented, with comparisons to the similar amplitudes of single breaking results.

Finally, in chapter 8, conclusions and further work suggestions are presented.

Chapter 2

Breaking Waves and Surface Films

2.1 Introduction

In this chapter, the basic properties of water are discussed as well as the formation of waves and surface films. First, both deep and shallow water waves are examined and then a formal mathematical description of wave motion is given. The process of classifying wave breaking is explained, and finally the formation and effect of surface films is examined.

2.2 Properties of Water

Most people consider water to be rather boring; familiarity breeds contempt, it's the most common substance in the biosphere. We drink it, wash in it, cook in it and much more. However, simple H_2O is one of the most interesting compounds on Earth. As shown by its chemical formula, water consists of two hydrogen atoms and one oxygen atom joined by covalent bonds, seen in figure 2.1

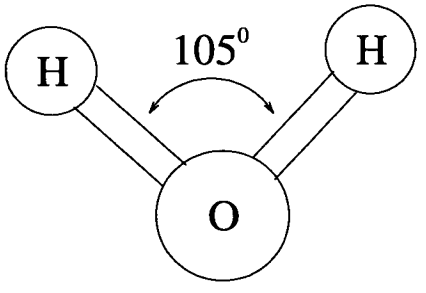

Figure 2.1: Water molecule

Some of the most important properties of water are its anomalies [12]. Water is the only naturally occurring inorganic substance and the only chemical compound found on the planet in all three states [30] .Water has a large heat capacity, enabling the thermal regulation required for sustaining life; both internally, human beings consist of nearly two-thirds water, and externally, for example, by stabilising the temperature of the oceans. Its excellent solvent properties make it very useful for washing and cleaning. Also, water has a melting point around 100^0C higher than similar substances and a boiling point almost 200^0C higher (see table 2.1); usually these values decrease with molecular mass [72].

Molecule	Molar mass	Melting Point (^{0}C)	Boiling Point (^{0}C)
H_2Te	128.6	-51	-1.8
H_2Se	81	-60.4	-41.5
H_2S	34	-85.6	-60
H_20	18	0	100

Table 2.1: Melting and boiling points of water (H_2O) and similar substances

All solids and liquids have a force of attraction between molecules. The force in water is known as *Hydrogen Bonding.* Water is a polar molecule in which there is a positive ($H^{\delta+}$) and negative ($0^{\delta-}$) pole. The attraction between the hydrogen of one molecule and the oxygen of another forms an intermolecular bond. These bonds are unusually strong, and although water is not the only substance to show hydrogen bonding, it is the most significant and commonly occurring. The special features of water which make it so important to life have even lead to it being used as an argument for the existence of a Creator.

2.3 Water Waves

One of the reasons we take water for granted is the vast quantities that we see it in. Around 70% of the Earth's surface is covered with water. For most of us, our experience of this is limited to watching the waves breaking or occasional adventures in the sea, like the North Berwick Rat Race held every year to raise money for the RNLI, shown in figure 2.2. Whilst the actual molecules of water in the waves rarely leave the coastal area, the waves themselves probably came

Figure 2.2: North Berwick rat-race, 2003

from many miles out to sea.

Waves are formed in three different ways, the most familiar of which is wind generation. Fluctuations in the pressure on the water surface caused by the winds result in tiny ripples. The wind "catches" these tiny ripples causing them to grow further, producing bigger waves. The disturbances continue to grow until an equilibrium is reached.

Another form of wave are the tides. Tides are very large scale waves caused by the gravitational attraction of the moon and sun. Since the orbits of these bodies are not geocentric, there are times when their attractions are stronger or weaker, depending on the distance from the ocean. Tides have periods of 12 or 24 hours, semi-diurnal and diurnal respectively. There are also longer period tides which produce higher or lower tide lines than normal, such as the spring or neep tides.

The third cause is displacement, for example the ripples caused by throwing a stone into a pond. When the stone strikes the surface, the water underneath is pushed out of the way causing a disturbance. The size of the waves produced obviously depends on the size and speed of the object hitting the surface. Very large displacements such as earthquakes or landslides can cause huge waves, called tsunamis. The island of La Palma in the Canaries is home to the volcano Cumbre Vieja. Instabilities on the side of the volcano have led specialists to believe in the potential for a giant landslide in the event of another eruption. A slide on this scale would produce a wave approximately 600m high [7], almost entirely destroying the Canary islands. Although events like this are very rare, they should not be underestimated, with waves reaching heights of 30 metres they are considered highly dangerous [43, 79] Most waves are much smaller, of the order of decimetres. In order to discuss waves in more detail, it is essential to define the terms involved.

2.3.1 Deep Water Waves

Simple waves are defined in terms of *wavelength* λ, *frequency* f, *local wave height* H and *amplitude* a, as shown in figure 2.3. The wavelength λ is the distance between two successive wave crests. Related to the wavelength is the *wavenumber,* $k = \frac{2\pi}{\lambda}$. For small, linear waves, λ is well defined. However, this distance is less easy to pin-point for non-linear waves or waves prior to breaking. H is the distance

between wave crest and trough, and a, the amplitude, is the distance between the *Mean Water Level, MWL* and the wave crest. For linear waves, this is equivalent to $\frac{H}{2}$. The *free surface elevation*, often denoted by η, is the height of any part of the wave above the *Mean Water Level.*

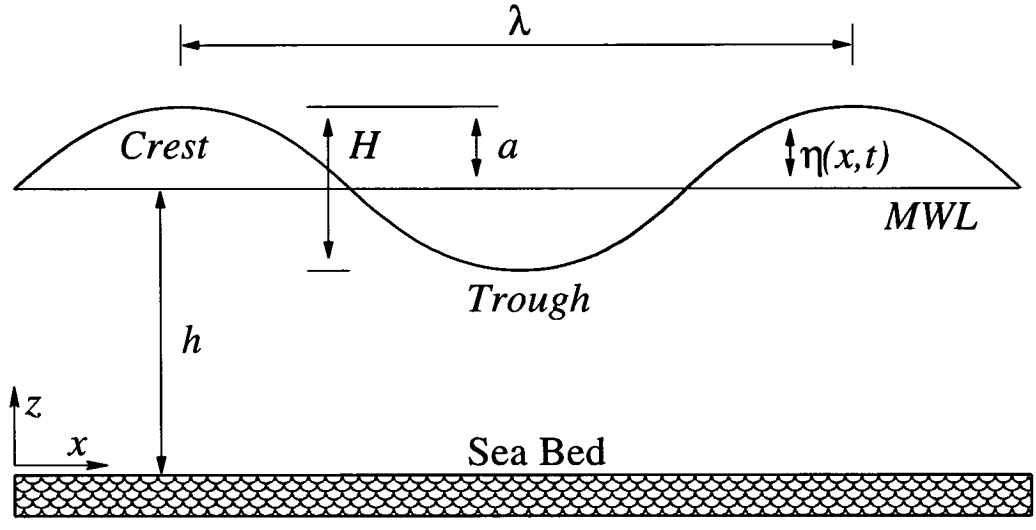

Figure 2.3: Wave parameters in deep water

The frequency, f, is defined as the number of waves passing a fixed point every second and is often quoted as the *angular frequency*, $\omega = 2\pi f$. Another important quantity is h, the *mean* or *local water depth.* This is defined as the distance between the sea bed and the *MWL.* For water undergoing a net average motion, such as up and down a beach slope, it may be necessary to define the *Still Water Level* seperate from the *MWL.* The *SWL* is the level the water would sit at if there was no wave motion, as opposed to the average of the peaks and troughs. The *still water depth*, d is the distance between the sea bed and the

Still Water Level. For small linear waves, d and h are equivalent, as are *MWL* and *SWL.*

For linear waves, it is possible to define a mean slope between a wave crest and node (where $\eta = 0$) as $\frac{4a}{\lambda}$ or $\frac{2ak}{\pi}$ [4]. Therefore, the parameter ak can be thought of as a non-dimensional slope. For the deep water experiments carried out in this Thesis, the central k value is kept at 3.17ms^{-1}, in effect reducing ak to a non-dimensional amplitude describing the wave.

2.3.2 Shallow Water Waves

As waves approach a beach, they begin to feel the effect of the sea bed. This causes them to become asymmetric, slow down and increases the height of the crest; an effect known as *shoaling.* The final effect of shoaling is breaking, and the different kinds of breaking will be discussed in section 2.5.

Two important factors in determining the breaking of a wave approaching the shore are the beach slope β, shown in figure 2.4, and the wave height. The non-linearity of shoaling waves means that the MWL is no longer the same as the *SWL.*

A fuller discussion on shallow water waves and factors causing breaking can be found in Emarat [26].

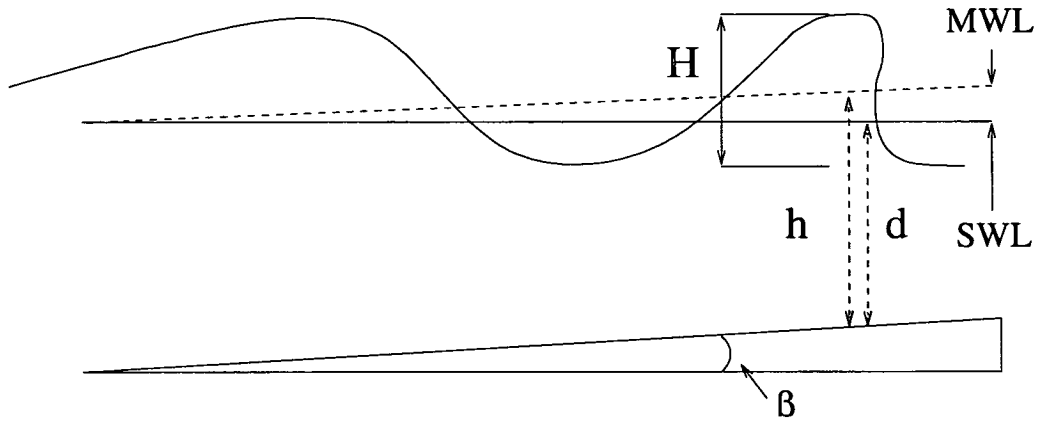

Figure 2.4: Wave parameters on a beach

2.4 Mathematical Description of Wave Motion

Regardless of the initial cause, waves are driven by two factors: gravity and surface tension. Provided the amplitude of the wave is small enough for linear theory to apply, both can be described using potential theory by solving LaPlace's equation, 2.1, with correct boundary conditions [16];

$$\nabla^2\phi = 0 \tag{2.1}$$

where ϕ is the *velocity potential*

The angular frequency of the wave motion is dependent on the wavenumber k, the surface tension σ, density ρ, and the water depth d. The relationship is given by the *dispersion equation*:

$$\omega^2 = \left(gk + \frac{\sigma k^3}{\rho}\right) \tanh(kd) \tag{2.2}$$

where g and σ are $9.81 ms^{-2}$ and $0.0728 Nm^{-1}$ at room temperature, respectively.

2.4.1 Phase Speed

The phase speed, or celerity C, of the wave is the speed that a wave crest appears to move on the water. It can be calculated from ω by dividing by the wavenumber. Therefore, the celerity is given by:

$$C = \frac{\omega}{k} = \sqrt{\left(\frac{g}{k} + \frac{\sigma k}{\rho}\right) tanh(kd)} \tag{2.3}$$

Of the three terms containing k in equation 2.3, $\frac{g}{k}$ and $\frac{\sigma k}{\rho}$ will be examined first. The former depends on gravity, the latter on surface tension (assuming constant density). This is the basis of saying waves can be driven by either gravity or surface tension. The distinction comes from the position of the wavenumber, which appears on the denominator of the first term and the numerator of the second. This implies that large wavenumbers, corresponding to small wavelengths, are primarily driven by surface tension. Conversely, waves with large wavelengths are gravity driven.

The third term containing k is $tanh(kd)$. kd is in essence a non-dimensional measure of water depth. As kd increases, that is to say the shorter wavelengths in the same depth or the same wavelength over greater depths, tanh (kd) tends to 1. For a kd value of π, $tanh(kd)$ is 0.996, and therefore the celerity is assumed to be independent of depth at this point. This corresponds to $\frac{d}{\lambda} = \frac{1}{2}$, when the depth is half the wavelength.

Assuming the case of deep water, the celerity reduces to

$$C_{deep} = \frac{\omega}{k} = \sqrt{\left(\frac{g}{k} + \frac{\sigma k}{\rho}\right)} \tag{2.4}$$

which is dependent on wavenumber alone. A graph of celerity against wavelength, intuitively easier to understand than wavenumber, is shown in figure 2.5. For short wavelengths, where k is large, the term in equation 2.4 containing surface tension dominates and these waves are called *capillary waves.* The celerity has a minimum at $0.23ms^{-1}$, corresponding to a wavelength of approximately 0.017m. If the wavelength is longer than this, the gravity term dominates and the celerity increases as $\sqrt{\lambda}$.

However, in shallow water $tanh(kd)$ can no longer be approximated to 1. It is possible to perform a MacLaurin expansion on $tanh(kd)$:

$$tanh(kd) = kd - \frac{1}{3}(kd)^3 + \frac{2}{15}(kd)^5 + O(7) \tag{2.5}$$

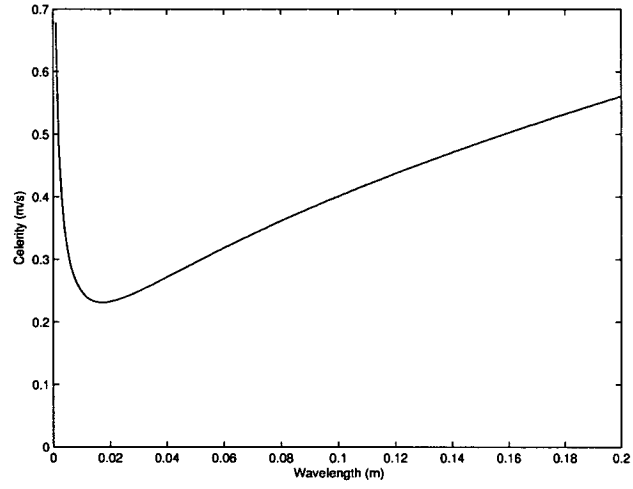

Figure 2.5: Celerity against wavelength

If $kd = 0.05$, the 3rd and 5th order terms are $4.17\text{x}10^{-5}$ and $4.17\text{x}10^{-8}$ respectively. Therefore $tanh(kd)$ can be approximated to kd to greater than 0.1% accuracy. Hence, the definition of shallow water is when $kd < 1/20$ (anything in between this and deep water is called *intermediate.*) Replacing $tanh(kd)$ with kd reduces equation 2.3 to

$$C_{shallow} = \sqrt{\left(g + \frac{\sigma k^2}{\rho}\right) d} \tag{2.6}$$

Gravity driven waves are no longer dependent on wavelength whereas capillary waves now vary as k^2. Since the surface tension driven element falls off so rapidly, most waves longer that 1.7cm are dominated by the gravity term and travel at the same speed, $\sqrt{gh}$, in shallow water, regardless of length. This is summarised in table 2.2.

Wave length	Shallow water celerity	Deep water celerity
$\lambda < 1.7cm$	$\frac{1}{\lambda}$	$\sqrt{\frac{1}{\lambda}}$
$\lambda > 1.7cm$	$\sqrt{gh}$	$\sqrt{\lambda}$

Table 2.2: Celerity of capillary and gravity waves in shallow and deep water

2.4.2 Beating

Ocean waves consist of a spectrum of wavelengths. However, in the seas or deep coastal waters, only very long waves or tides may be treated as shallow. It is therefore reasonable to treat any given wave packet in deep water by examining it as if it exists solely of deep water waves using equation 2.4.

Defining two arbitrary waves with angular frequencies ω_1 and ω_2 and wavenumbers k_1 and k_2 respectively, each with amplitude $\frac{a}{2}$, the two waves can be combined using linearity, to give

$$\eta(x,t) = \frac{a}{2}(cos(\omega_1 t - k_1 x) + cos(\omega_2 t - k_2 x)) \tag{2.7}$$

where η is the free surface elevation, defined in section 2.3.1. Rearranging gives:

$$\eta(x,t) = acos\left(\frac{\omega_1+\omega_2}{2}t - \frac{k_1+k_2}{2}x\right) cos\left(\frac{\omega_1-\omega_2}{2}t - \frac{k_1-k_2}{2}x\right) \tag{2.8}$$

This is the multiple of two waves, the first with frequency $\omega_1+\omega_2$, the second with frequency $\omega_1 - \omega_2$, and similarly for k. If ω and k for waves 1 and 2 are

similar, then $\omega_1 + \omega_2 >> \omega_1 - \omega_2$. The first term in equation 2.8 will therefore be of a far higher frequency than the second term. This means η will have the appearance of a high modulation wave in the envelope of a much slower varying wave, as shown in figure 2.6 where $\omega_1 = 10$, $\omega_2 = 9$ and $a = 5$.

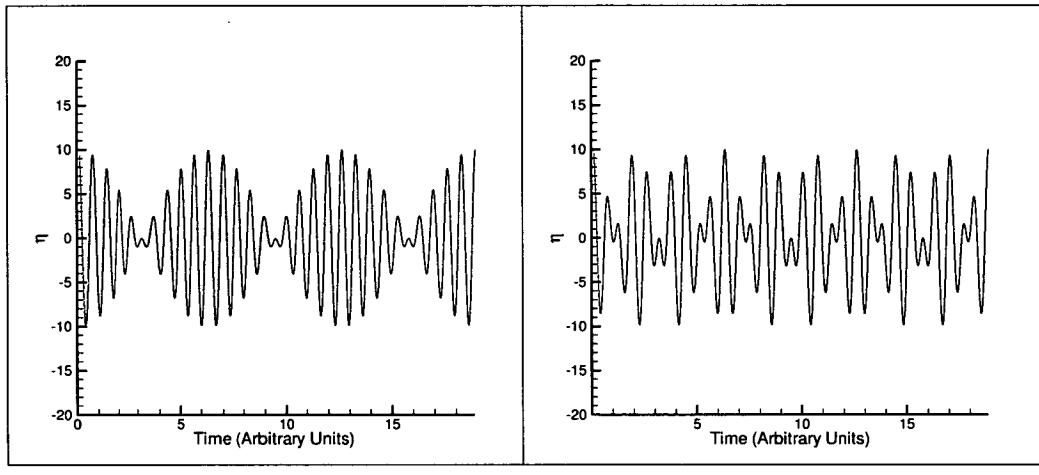

Figure 2.6: Beating effects with $\omega_1 = 10$ and $\omega_2 = 9$ (left) and $\omega_2 = 7$ (right)

When two sound waves of similar frequencies are played simultaneously, they add in the same manner as described above. The resulting sound appears to beat, getting louder and softer with a rate equal to the difference between the two frequencies. This effect is known as beating.

However, it is important that the two frequencies are close together. If $\omega_1 - \omega_2$ is not a lower order of magnitude than $\omega_1 + \omega_2$, then beating does not occur cleanly or at all, as shown on the right of figure 2.6.

2.4.3 Group Speed

Although water waves will be made up of a range of frequencies, often these frequencies are close together. Therefore the effects seen in figure 2.6 can be seen in ocean wave packets. The high frequency component travels at a speed $\frac{\omega_1+\omega_2}{k_1+k_2}$ or $\frac{\omega_m}{k_m}$, where ω_m and k_m are defined as the mean values of ω and k respectively. The envelope travels at $\frac{\omega_1-\omega_2}{k_1-k_2}$. The *group speed*, C_g is defined as the limit as k_1 tends to k_2. This is the derivative of equation 2.2 with respect to k:

(A) (B)

$$C_g = \frac{d\omega}{dk} = \frac{C}{2}\left[1 + \frac{2\sigma k^2}{g\rho + \sigma k^2} + \frac{2kd}{sinh(2kd)}\right] \tag{2.9}$$

$$A = \frac{2\sigma k^2}{g\rho + \sigma k^2}$$
$$B = \frac{2kd}{sinh(2kd)}$$

There are four cases to consider, combining deep or shallow water, with gravity or capillary waves. Term A in equation 2.9 includes wavenumber, and will therefore be affected by changing wavelength. Term B contains kd, the non-dimensional water depth, and will therefore change for deep or shallow water.

As g and ρ are both constant, the value of term A will depend on the size of σk^2 relative to this value. If σk^2 is much smaller than $g\rho$, then term A will be very small as the denominator will be far larger than the numerator. However, if σk^2 is much greater than $g\rho$, term A will simplify to $\frac{2\sigma k^2}{\sigma k^2} = 2$. For capillary waves, λ is small, and therefore k, and k^2 are large, and term A is therefore virtually 2. For longer gravity waves, k is smaller and term A becomes zero.

A graph of term B against deepening water, increasing kd for constant k, is shown in figure 2.7.

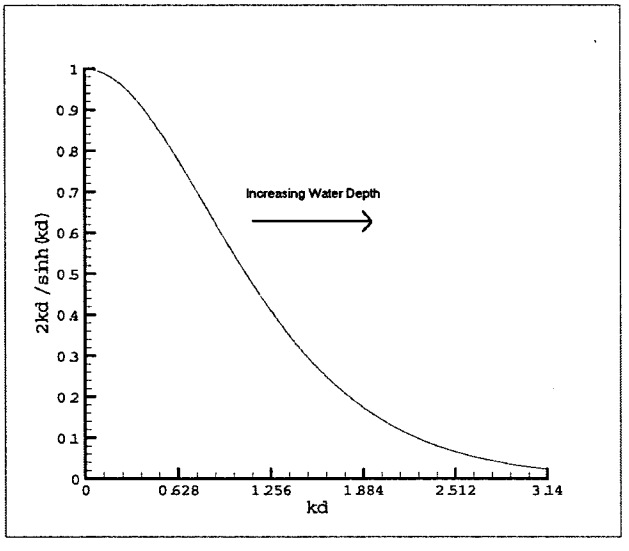

Figure 2.7: Graph of $2kd/\sinh(2kd)$ against kd for 0 to π

The definition of deep water is when kd > pi. As the figure shows, term B will be virtually zero in this region. For shallow water kd is $< \frac{1}{20}$ and therefore $\frac{2kd}{sinh(2kd)}$ can be approximated to 1.

The resulting group velocities, in terms of a multiple of the phase velocity C, are shown in table 2.3.

Wave	Deep Water (B = 0)	Shallow Water (B = 1)
Gravity (A = 0)	$\frac{C}{2}$	C
Capillary (A = 2)	$\frac{3C}{2}$	2C

Table 2.3: Group velocity as a multiple of phase velocity

2.4.4 Water Trajectories

The actual particles of water do not move with the group velocity. The trajectories of the particles can also be calculated from equation 2.1 [78]. In deep water, the individual water elements move in circles, which have a maximum radius of a at the surface and decrease with depth as shown in figure 2.8. For intermediate and shallow waves, the particles move in ellipses, getting smaller and flatter as they approach the bottom.

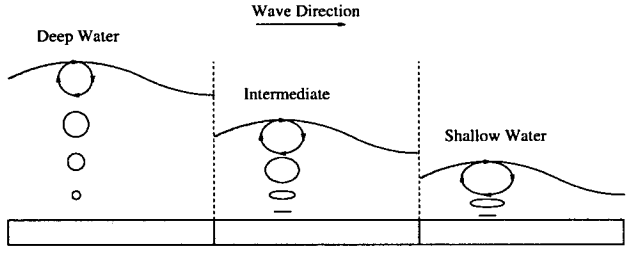

Figure 2.8: Water motion under a wave

2.4.5 Shoaling

As waves approach the shore they will change from deep to shallow water. As discussed in the previous sections, this will change the celerity of the wave. If the wave train is coming in at an angle, then this change in celerity will cause the wave fronts to bend as one side will be in shallow water, and therefore travelling slower than the other, which will be in deep water. This is a very similar process to the refraction of light changing from one medium to another, which is discussed in section 4.6.2. The wave fronts will become closer together as the celerity decreases, and hence the amplitudes will become higher. Assuming no reflection, conservation of energy predicts that the amplitude will increase as

$$H_r = H_o K_r K_s \tag{2.10}$$

where H_r is the amplitude caused by refraction, H_o is the original amplitude and K_r and K_s are the refraction and shoaling coefficients. The refraction coefficient depends on the angle of the wave relative to the beach while the shoaling coefficient is defined as $\sqrt{\frac{C_d}{2C_g}}$, where C_d is the deep water celerity and C_g is the local group velocity, as defined in section 2.4.3. The group velocity can tend to zero with decreasing depth, which implies that H_r can approach infinity. However, long before the wave amplitudes become too large non-linear effects become important. The wave no longer has a clear sinusoidal shape; the front face becomes

gradually steeper until eventually breaking occurs.

2.5 Wave Breaking and Classification

As the wave approaches the point of breaking, the waves can no longer be described accurately by linear approximations. As the mathematics becomes more complicated for non-linear waves and requires greater explanation, it is not presented here. Examples and descriptions can be found in a number of fluid dynamics textbooks [16, 17, 73].

There are many definitions of breaking [5, 8, 31, 55]. One commonly used definition is that breaking occurs at the point where the tip curls over and entrains air. It is generally accepted that there are four types of breaker; spilling, plunging, collapsing and surging. Of these, collapsing and surging only occur on beaches. A brief diagram of each type can be seen in figure 2.9.

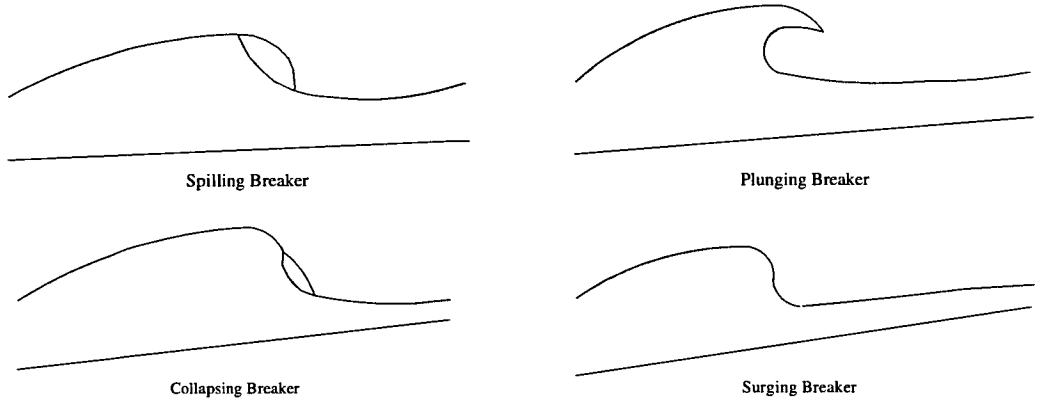

Figure 2.9: Breaker classification

Spilling breakers occur when the tip of the wave crest becomes unstable and runs down the leading edge of the wave, creating foam. On beaches, the wave crest may have travelled a number of wavelengths towards the sand during this process. Plunging breakers are larger and more violent than spilling breakers. The wave crest turns over, trapping air between it and the front face of wave. When the crest strikes the leading edge, the enfolded air is mixed with the water and a large splash forward is created. This process disperses the energy far quicker [26], and therefore takes place over only one wavelength. Collapsing is when the crest and upper front face of the wave remain intact but the lower face breaks, entraining air. The resulting foam continues up the beach in a similar manner to a spilling breaker. Surging breakers occur on the steepest beaches and the wave crest does not actually break. Here the base of the wave rushes ahead of the crest, flattening the wave again, with mild breaking and reflection.

The classification of breakers into each type is usually done visually, although a number of methods have been devised to define a breaker from the conditions under which it occurs [36]. A large number of these conditions are dependent on beach slopes or shallow water, but breaking is still evident in deep water [21, 37]. These breakers are always spilling or plunging. Breaking can also be observed and studied from ship wakes [6].

The linear theory discussed in section 2.4 is unable to predict wave shapes prior to breaking. Non-linear theory was first attempted by Stoke using a perturbation

method to include up to third order terms [73]. Higher order solutions have been attempted since. In addition to this numerical methods such as time stepping, the Boundary Integral and Boussinesq models have been developed. These methods can predict the wave motion up to the point of breaking, but breaking itself and the onset of turbulence means the models are unable to predict the water's motion after this [22].

Therefore, most work on post-breaking waves has been done experimentally [13, 26, 67]. As the breaking process is largely unpredictable in the ocean environment [37], most experiments are performed in laboratory wave tanks.

The formation and dynamics of turbulence beneath breaking waves has been studied before; In 1995, Ting and Kirby looked at the turbulence created by a plunging breaker on a beach using Laser-Doppler Anemometry [77].

Research on breaking waves using Particle Image Velocimetry, PIV, and Digital PIV to calculate flow patterns has also been carried out. Mocke [50] studied the structure of surf-zone turbulence due to wave breaking. Emarat [26] also studied the development of turbulence beneath breaking waves; single plungers, a train of weak plungers and a train of spilling breakers.

Specifically in the area of mixing of a surface film caused by breaking waves, previous work has been carried out by Rapp and Melville [59] and Schlicke [67]. Rapp and Melville studied the mixing effect of a single plunging breaker on a

surface layer of blue vegetable dye. Schlicke also studied the dispersion of a surface film caused by a breaking wave. Schlicke examined five single breakers varying from mild spillers to plungers. This was the inspiration to carry out the work in this Thesis, expanding the number of single breakers examined and looking at the effect of a second breaking wave.

2.6 Surface Films

Despite the apparently huge size of many lakes and rivers, they account for only a very small percentage of the water on Earth. As can be seen in table 2.4, the vast majority of water is present in the oceans and seas.

Location	Percentage of water on Earth
Oceans and seas	97.13%
Ice caps and glaciers	2.24%
Groundwater	0.61%
Lakes and Rivers	0.02%

Table 2.4: Percentage of water in different locations on Earth [30]

The oceans themselves are approximately 96.5%, by weight, water molecules; the rest made up of dissolved solids, as shown in table 2.5

Although they make up a small percentage of the total volume, the solutes can make a large difference to the nature of the water [72]. Certain substances, called *surfactants*, are attracted to fluid interfaces, including the water's surface.

Dissolved Solid	Percentage by weight of ocean
Sulfates (SO_4^{2-})	0.27%
Sodium (Na^+)	1.05%
Chloride (Cl^-)	1.90%
Other	0.28%

Table 2.5: Percentage of dissolved solids in oceans [72]

Surfactants - *surface active agents* will affect the formations and evolution of the waves. Organic molecules often contain either carboxyl (COOH) or hydroxyl (OH) groups. These groups are *hydrophilic*, easily assimilated into water. The opposite effect, *hydrophobic*, is exhibited by long carbon chains. A molecule which contains both types will tend to be surfactant, the hydrophobic part drawing it towards the water's surface and the hydrophilic remaining in the water body, as shown in figure 2.10.

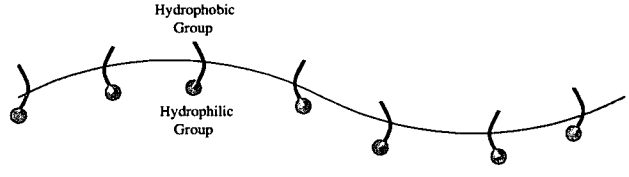

Figure 2.10: Surfactants at the water's surface

There are a large number of sources of surfactants [65], ranging from natural productions by phytoplankton, or decaying vegetation to man-made sources like petroleum or detergent. As these molecules push to the surface, they reduce the number of hydrogen bonds and therefore the surface tension. It can be seen from equation 2.3 that altering the surface tension will have a more significant direct

effect on capillary waves than gravity waves.

2.6.1 Damping of Capillary Waves by Surface Films

The effects of surface films can be seen clearly in any harbour or shipping lane. By damping the shorter capillary waves the smoother surface reflects more light and appears brighter, as can be seen in the photograph of Kinghorn harbour, on the Firth of Forth in figure 2.11.

Figure 2.11: Surface films on the Firth of Forth

The damping effect of surface films has been known for many years, hence the expression "*Pour oil on troubled waters*" to mean calming down a situation, although the first scientific investigation on the effect was carried out by Benjamin Franklin nearly 230 years ago [29]. The boundary condition on the water's surface states that the sum of surface stresses must be equal and opposite to the sum of viscous stresses. If the water were pure and clean then the surface tension would

be uniform and therefore the surface stress, and subsequently the viscous stress, would be virtually zero. When there is a film on the surface, the contractions and expansions at the front and rear of the waves cause the surface tension to vary, and therefore produce viscous stresses. These in turn are responsible for significant velocity gradients, large enough to result in damping.

The change in surface tension σ, caused by a change in a given surface area, A, is given by the surface dilation modulus, ϵ:

$$\epsilon = \frac{d\sigma}{d(lnA)} \tag{2.11}$$

If the surface is perfectly clean then changing the area has no effect on the surface tension, and therefore ϵ is zero. However, for an inextensible surface, it would be impossible to change the area, and therefore ϵ would be ∞.

To account for the possibility of damping over both distance and time, Lucassen-Reynolds and Lucassen[41] defined a complex wavenumber and frequency, given by $k = k_0 - i\beta$ and $\omega = \omega_0 + i\alpha$ respectively. The β term corresponds to damping occurring over distance, with the α term accounting for damping over time. This definition refines the surface elevation to

$$\eta_{complex}(x,t) = ae^{ikx+i\omega t} \tag{2.12}$$

$$= ae^{\beta x}e^{-\alpha t}e^{i(k_0 x+\omega_0 t)} \tag{2.13}$$

For low viscosity, the ratio of α to β is given by the group velocity.

The temporal damping coefficient α can be approximated as [24]:

$$\alpha = \frac{1}{2}k\delta\omega\frac{1+2k\delta\gamma(\gamma-1)}{(\gamma-1)^2+1} \tag{2.14}$$

where δ is the width of the viscous shear layer and γ is a dimensionless parameter, defined as

$$\gamma = (2\nu)^{\frac{1}{2}}\rho C_s\omega^{\frac{3}{2}}k^{-2} \tag{2.15}$$

where ν is the kinematic viscosity and C_s is proportional to $\frac{1}{\epsilon}$. Taking δ to be $\sqrt{\frac{2\nu}{\omega}}$ [57], then equation 2.14 can be written again in terms including ν and ω:

$$\alpha = \sqrt{\frac{\nu\omega k^2}{2}}\frac{1+\sqrt{\frac{8\nu k^2}{\omega}}\gamma(\gamma-1)}{1+(\gamma-1)^2} \tag{2.16}$$

When there is no surface film the values of ϵ and γ will be 0 and ∞ respectively. As γ tends to ∞, the second term in equation 2.16 is dominated by $\frac{\gamma}{\gamma-1}$ which rapidly becomes 1. Therefore, α reduces to

$$\begin{aligned} \alpha_{\gamma=\infty} &= \sqrt{\frac{\nu\omega k^2}{2}}\sqrt{\frac{8\nu k^2}{\omega}} \\ &= \sqrt{4\nu^2 k^4} \\ &= 2\nu k^2 \end{aligned} \tag{2.17}$$

If, however, γ is set to 0, representing a film of infinite dilation modulus, then α becomes

$$\begin{aligned} \alpha_{\gamma=0} &= \sqrt{\frac{\nu\omega k^2}{2}}\frac{1}{1+1} \\ &= \frac{1}{2}\sqrt{\frac{\nu\omega k^2}{2}} \end{aligned} \tag{2.18}$$

These results had already be obtained by Lamb [38] independently.

It can be seen that the maximum damping will occur when γ is around 1, and

$$\alpha_{\gamma=1} = \sqrt{\frac{\nu\omega k^2}{2}} \tag{2.19}$$

This is twice the value for the inextensible film. Longitudinal disturbances, called Marangoni waves, caused by variations in surface tension are responsible for this maximum value [3]. When γ is approximately 1, the perpendicular wave mo-

tions have equal wavelengths but opposite phases and therefore there is resonant damping.

If the ratio of the damping coefficients for a surface with finite dilation modulus to that with a clean surface is plotted against wavelength it shows that damping increases with longer wavelengths [67]. However, equation 2.15 shows that as wavelength increases, by necessity C_s would have to decrease to maintain maximum damping at $\gamma = 1$. A decrease in C_s means an increase in ϵ, which is of the order of $20mNm^{-1}$ or less. The value of ϵ is simply too small to accommodate the decrease in C_s required and γ can no longer remain at unity, hence in real situations surface films can only significantly damp capillary waves.

However, gravity waves can still be affected by surface films. As discussed in section 2.3, wind waves are formed largely by the force of the wind on the surface ripples. By removing these capillary waves, the effect is to inhibit the formation of the gravity waves.

Although some field tests have been carried out to confirm this [2, 29], the deliberate release of surfactants is not generally used.

2.6.2 Dispersion of Surface Films

A surfactant substance is most stable on the surface of the water, and therefore will not naturally disperse below the surface unless otherwise disturbed. Without

disruption, films are more likely to spread on just the air-water interface. Previous work has been carried out on the dispersion of these films on the surface, both experimentally, using tracers [32, 35], or computationally [10], and has shown that the rate of dispersion increases with time on large scales with random variations caused by Stokes drift on smaller scales.

Previous experiments have attempted to show the fate of the massive amount of surfactants released or formed every year. However, they either do not account for losses due to mixing below the surface, or else estimate these values. By obtaining a connection between the roughness of the sea and the amount of dispersion of surface films vertically, it will be possible to make more accurate predictions for the future of these pollutants and surfactants.

2.7 Conclusions

In this chapter the basic properties of water were discussed, followed by a description of water waves in deep and shallow water. A formal mathematical description of wave motion was presented and the different forms of breaking wave and their classification was given. Finally, the formation and dispersion of surface films was reviewed.

Chapter 3

Experimental Facilities

3.1 Introduction

In this chapter, the experimental facilities employed for this research are presented. The reason for applying an experimental approach to investigating film dispersion is discussed, followed by a description of the processes of wave generation, laser illumination and data collection necessary to perform the Planar Laser Induced Fluorescence (PLIF) experiments. The chapter ends with a presentation of the final experimental set-up used in the experiments reported.

3.2 Background

There are three approaches to research; *Experimental, Theoretical* and *Computational.* Each of these methodologies has it own advantages and disadvantages.

Theoretical physics began when the first scientists thought about the world around them, and continues to this day albeit assisted by more and more advanced technology. This advancing technology also opened up the relatively new field of computational simulation. Situations that are too complex to treat theoretically, or impractical to re-create experimentally, can often be investigated using computational simulations. However, because these simulations often require calibration to experimental results, the first step is to explore experimentally.

Ever since the renaissance mankind has been learning through experiment. There are no equations too complex for nature to follow, and all the calculations are carried out in real-time; the problem is interpreting what we see. In circumstances where the theory is unsolvable analytically, progress by any method is extremely hard. This applies especially to fluid dynamics, governed by the Navier-Stokes eqauation(3.1):

$$\rho\frac{D\mathbf{u}}{Dt} = -\nabla\rho + \mu\nabla^2\mathbf{u} + \mathbf{F} \tag{3.1}$$

where ρ is the density, $\mathbf{u}$ is the fluid velocity, μ the coefficient of viscosity and

F any body forces acting on the fluid, such as gravity. The non-linearity of this equation means it can only be solved directly for the simplest cases [78].

Advances in technology, such as the invention of lasers and digital cameras, and the improvement of computers, have meant that more experiments, with greater accuracy, can be carried out on fluid flows. Although recent theoretical and computational work has been able to predict wave motion leading up to breaking, models cannot carry through to post-breaking [26]. Therefore, an experimental approach was necessary for the study of the post-breaking dispersion of surface films.

3.3 Selection of Experimental Method

Innumerable attempts have been made to measure fluid flow. Leonardo Da Vinci attempted to study turbulence by drawing the famous image of swirls and eddies, shown in figure 3.1.

More recently, many experimental techniques have been developed to obtain qualitative and quantitative flow measurements. Laser Doppler Anemometry (LDA) and Hot Wire Anemometry (HWA) methods can be used to obtain velocity measurements within a flow [14]. Particle Image Velocimetry (PIV), a full-field instantaneous technique employed to record velocities in a fluid, can be used to study a wide range of flows [26, 63, 81]. In PIV experiments, a flow is seeded

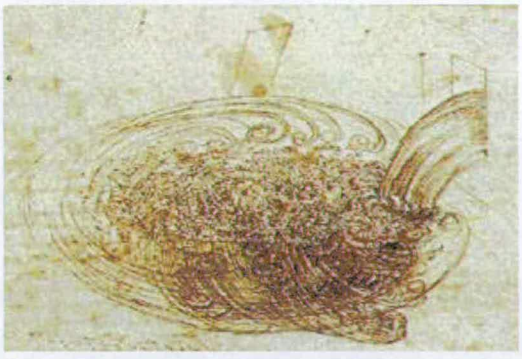

Figure 3.1: Leonardo Di Vinci's sketch of turbulence [61]

with small particles and a cross section of the fluid is illuminated. By recording and analysing the positions of the particles at different times, velocity maps can obtained. Laser Induced Fluorescence (LIF) is a full field optical technique which yields concentration measurement, described in detail in chapter 4. Whereas PIV, LDA and Hot Wire Anemometry are excellent methods for the study of fluid flow or velocity, LIF makes it possible to distinguish between two similar fluids, and is therefore better suited to dispersion measurements.

3.4 Wave Tank and Wave Generation

All the breaking wave experiments in this thesis were carried out at the University of Edinburgh in a wave tank, shown in figure 3.2, built by David Skyner [70]. The tank is $9.77m$ long, $0.4m$ wide with a working water depth of $0.75m$. Only fresh water can be used, to prevent corrosion on the structure.

The tank is equipped with a paddle at one end for generating waves, and an absorbing foam beach at the far end to prevent reflections. The wave paddle is capable of generating waves with a user-specified amplitude, phase and frequency. Breaking waves are created using the dispersion properties discussed in chapter 2. The user specified a desired size of breaking wave and breaking position as a distance from the paddle. A range of frequencies was also chosen. The software used to run the wave paddle automatically calculated the phase and amplitude of each wave in the packet required to produce a breaking wave with these criteria [64]. Any reflections were detected by transductors and accounted for during operation. The paddle was able to produce frequencies in the range 0.5 to 1.6 Hertz with a minimum wavelength of 0.6 metres. This meant all waves were gravity driven.

Figure 3.2: Photograph of wave tank used for experimental studies

The wave packets used in these experiments had a central frequency f_c, of 0.88Hz, corresponding to a wavelength of approximately 2 metres, with a fre-

quency spread Δf, of 0.64Hz. This give a frequency bandwidth, $\frac{\Delta f}{f_c} = 0.73$.

A series of tests were performed to ascertain the repeatability of the breakers. There was only a slight difference, a few centimetres, between breaking positions on each wave.

Seven different amplitudes of breaking wave were investigated: 9.9, 10.1, 10.3, 10.5, 10.7, 10.9 and 11.1cm, allowing comparisons with Schlicke [67] and Rapp and Melville [59]. The repeatability of the amplitude was also tested and found to be consistent.

As the tank is capable of running a series of waves, the effect of a second breaker on the mixing process was also examined at various amplitudes.

The wavemaker is capable of sending electronic trigger pulses at set times during the experiments. For these experiments, only one pulse was used, just before breaking. This pulse was sent via a relay switch to start a pulse generator. The pulse generator then sent the regular signals used to control the camera timing, as discussed in section 3.7.

3.5 Laser Illumination

Illumination for the experiment was provided by a Class 4 Argon Ion laser. The laser is capable of a maximum power output of approximately 17W over a number

of wavelengths, the strongest of which are 488nm and 514nm, corresponding to a blue-green light. As with any laser, safety was an important consideration and this is discussed further in section 4.5.2.

The beam left the laser with a radius of 0.79mm and a divergence θ, of 0.56mrad. As discussed in section 4.5.2, the laser was in a separate room to the wave tank and had to travel approximately 9m before reaching the experiment. The beam spread to approximately 10mm before being collimated as it entered the Scanning Beam Box.

3.6 Scanning Beam Box

A *Scanning Beam Box* was used to created a pseudo lightsheet by reflecting the laser beam off a rotating octagonal mirror, as shown in figure 3.3.

The mirror was capable of rotating at frequencies from 25Hz to 250Hz. Each revolution swept the beam through an arc of 90^0 eight times, producing a fan of light, approximately 2m across at the water surface. As the water depth is 0.75m, the illuminated area had a width-to-height ratio of approximately 2.66. The SBB was placed under the middle of the tank, equi-distant from both tank walls.

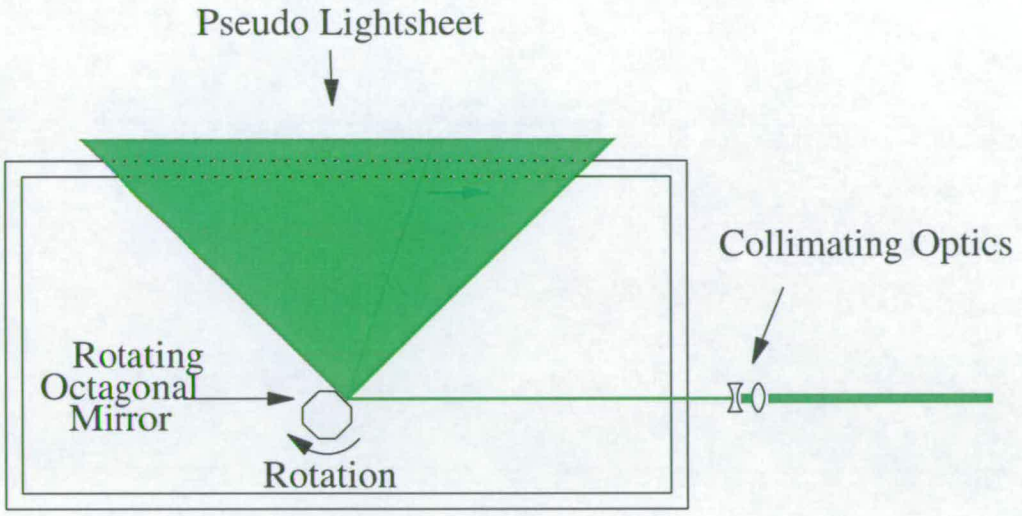

Figure 3.3: Scanning beam box

3.7 Cameras

Since all the images were analysed computationally, it was more efficient to use digital CCD (*Charge Coupled Device*) cameras to record the illuminated flow than wet film. The data from the digitally recorded images can be transferred directly to computer and analysed faster than wet-film images, as they do not require processing and scanning.

All digital cameras rely on CCD arrays to obtain images. A CCD consists of a semi-conductor surrounded by an insulator, with a small voltage applied to create a potential well. When a photon of the correct frequency strikes the array, an electron-hole pair is formed. The electron is attracted to the potential well where it is stored, and effectively counted, whilst the hole is absorbed into the

p-layer of the semi-conductor. While the array is exposed to light, the amount of charge in the well grows proportionally with the number of photons striking the CCD. Each CCD is known as a *pixel*, short for *pic*ture *el*ement, with modern digital still cameras having arrays of millions of such pixels.

The time taken to read the entire array is directly proportional to the number of pixels, and a new exposure cannot be started until all pixels have been read. This introduces a compromise between spatial and temporal resolution when measuring the flow.

3.7.1 Camera Noise

Electron-hole pairs within a pixel can also be produced by noise, such as random thermal noise which can produce extra electrons leading to an over-estimate of the amount of light received by a given pixel. Thermal noise reduces by 50% for every decrease in temperature of 6 - 7^0C, and specifically for this reason many newer CCD arrays are cooled [82]. However, cooled CCD cameras were not available for these experiments.

The clock frequency, which controls how fast pixel data can be processed with the camera and transferred, is another source of camera noise. To reduce this factor, many CCD cameras limit their clock speed to 20MHz [20].

Array Size	768(H) x 484(V)
Pixel Size	11.6μm (H) x 13.3μm(V)
Maximum Frame Rate	30fs^{-1}
Array Type	Full Frame Interline Transfer
Fill Factor	60%
Triggering	Asynchronous Reset
Memory per Pixel	8 bit

Table 3.1: Pulnix TM9701 camera specifications

3.7.2 Camera Arrangement

As discussed in section 3.6, the illuminated area was approximately twice as wide as it was high. In order to record this area as efficiently as possible, two CCD cameras were used side by side. The cameras were placed 3.25 metres away from the tank and had a field of view of approximately 18 degrees.Therefore they were placed just over 1 metre apart to cover the dispersion area.

3.7.3 Camera Specification

Two Pulnix TM9701 cameras were used for these experiments. Their details are listed in table 3.1 [58].

Although the cameras could capture at a maximum of 30 frames per second, in the experiments reported here the frame rate was set to twenty. This enabled a longer period after breaking to be available for recording since the amount of available computer RAM limited the number of images that could be recorded,

as discussed further in section 3.7.5.

The array type was *Full Frame Interline Transfer* (FFIT), where each pixel has a dedicated individual area for storing charge. Rather than store the charge over the course of the entire exposure, it is transferred quickly ($1\mu s$) to the storage area before being processed. This means FFIT arrays have a high maximum frame rate, as well as insuring that the pixels are exposed simultaneously, which is very important for flow measurements.

The *fill-factor* is the proportion of each pixel that is actually sensitive to light, not including the area designated to storage or transfer. Although only one fifth of the actual pixel is sensitive to light in the Pulnix TM9701, a microlens placed in front of each CCD in these cameras increases the fill factor by a factor of three.

Another important feature of these cameras is the asynchronous reset. This means the exposure could be controlled by an external trigger pulse. The cameras had undergone a factory modification to enable the exposure to be started on the falling edge of a TTL pulse and last the width of the pulse.

As each pixel is assigned 8 bits of memory, the cameras recorded 256 grey-scales, from 0 (black) to 255 (white). Since each exposure was approximately 3 $\times$ $10^3 Kb$ in size, dedicated hardware was required to process all data received at sufficiently high speed.

3.7.4 Lenses

The lenses used with the cameras were 28mm *Micro-Nikkor* with a maximum aperture of f/2.8 (see section 4.7.5). A square of specialised laser filter, permitting only the fluorescent wavelengths (see section 4.2), was placed in front of each lens to prevent any laser light entering the camera.

3.7.5 Frame Grabber

A Coreco Viper Quad frame grabber was used, running on a Windows NT PC. The frame grabber was capable of acquiring data from up to four asynchronous cameras, each using an independent channel with individual analogue to digital converter and synchronisation circuitry. The system is also able to provide power to the cameras and produce trigger signals via a 12 pin Hirose cable.

In order to operate Viper Quad, customised software had been written by Tim Dewhirst using the high-level "C" based library called Sapera in a *Graphic User Interface* (GUI). This software allowed the user to record or display images in real-time, set the exposure time and save the image data to the hard disc on the Windows NT PC. The software was triggered by a pulse generator, setting the frame rate and start time, synchronised to the wave maker. As both cameras were triggered by the same pulse, there was no need for further synchronisation.

As each camera was recording at twenty frames per second, over $28Mb$ of

memory is required every second. All data must be stored in the computer RAM before it can be saved to the hard-disc. The computer used had $1Gb$ of RAM which enabled 1000 images to be recorded from each camera.

3.8 Experimental Set-up

The final set-up of the experiment is shown on figure 3.4 where the blue values represent dimensions.

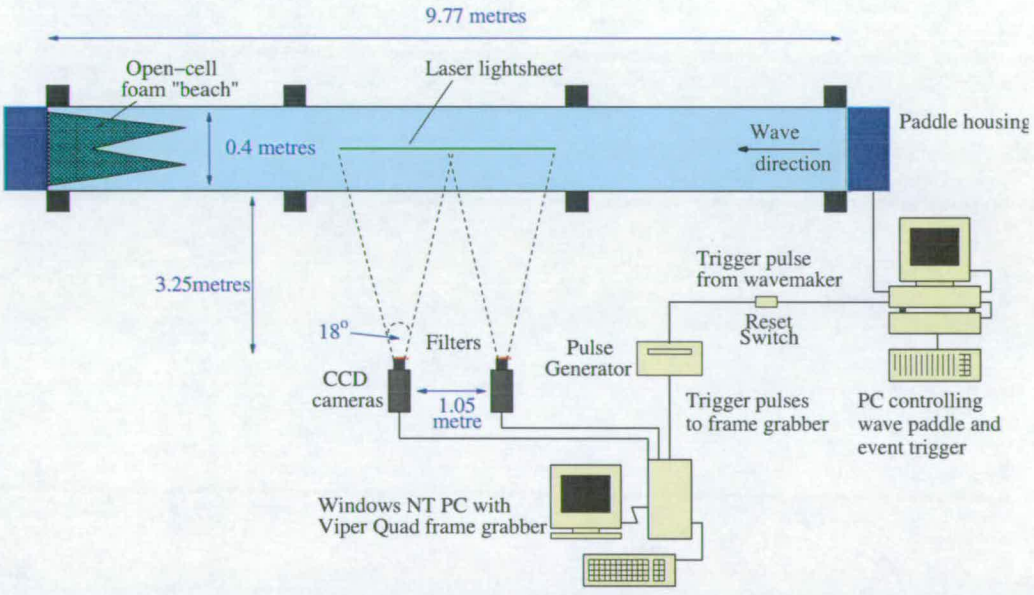

Figure 3.4: Experimental set-up

3.9 Summary

In this chapter the experimental facilities were reviewed. The process of wave generation, laser illumination, and recording equipment were discussed. Finally, a plan of the final set-up was presented.

Chapter 4

Planar Laser Induced Fluorescence

4.1 Introduction

As discussed in section 3.3, there are many available techniques for measuring fluid flow.

The work described in this Thesis uses Planar Laser Induced Fluorescence (PLIF). In this chapter, a review of the method of PLIF is presented with a description of how it was applied to the study of surface film dispersion by breaking waves.

4.2 Principle of Planar Laser Induced Fluorescence

PLIF is a full-field, non-intrusive, optical technique yielding concentration measurements. The method relies on the absorption and subsequent emission of photons by a fluorescent chemical. When a photon collides with an atom of the given chemical, it will either be scattered or absorbed. If the photon is absorbed, as illustrated in figure 4.1, an electron of the atom is raised to an unstable higher energy level. When the electron falls to a lower energy level another photon will be emitted. In an isolated state, or one with very small interactions such as a low density gas, the frequency of the emitted photon is identical to that of the absorbed photon. However, in circumstances where there are interactions, such as a fluid or solid, the frequency of the emitted photon will be changed.

When these frequencies fall into the visible spectrum, the material will appear to glow. If the absorption and emission process is of the order of 10^{-7} seconds or less, the process is said to be *fluorescence.* If the process takes longer, it is referred to as *phosphorescence.*

PLIF has been used in a number of mixing experiments for a range of different applications using either fluorescent tracer particles or dye [15, 18, 19, 52, 80, 83]. Experiments carried out by Catrakis [11] and Prasad and Sreenivasan [56] examined area-volume properties of fluid interfaces and turbulent jets respectively

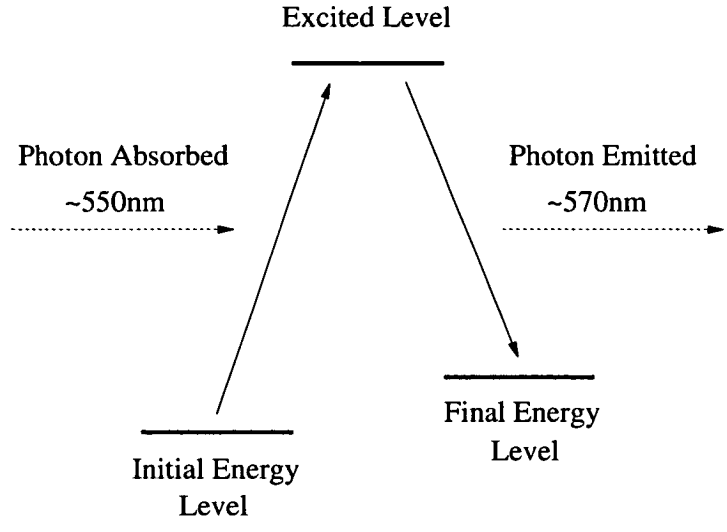

Figure 4.1: Process of LIF

using PLIF.

Three dyes are commonly used for PLIF experiments: fluorescein, rhodamine 6G and rhodamine B [75]. The organic dye rhodamine B, $C_{28}H_{30}N_2O_3Cl$, shown in figure 4.2, was chosen for all the experiments presented in this Thesis due to its absorption and emission spectra, comparatively low cost and duration of fluorescence.

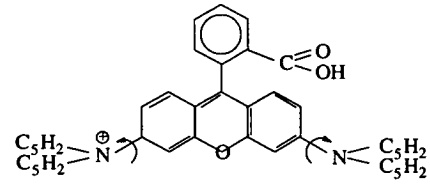

Figure 4.2: Chemical diagram of rhodamine

Rhodamine B absorbs light in the blue green wavelength, approximately $\lambda =$

$550nm$ as shown in figure 4.3. This corresponds to the wavelength of an Argon Ion laser. Rhodamine B fluoresces in the orange wavelength, $\lambda = 570nm$, as shown in figure 4.4. This enabled the separate recording of fluoresced dye using filters as discussed in section 3.7.4.

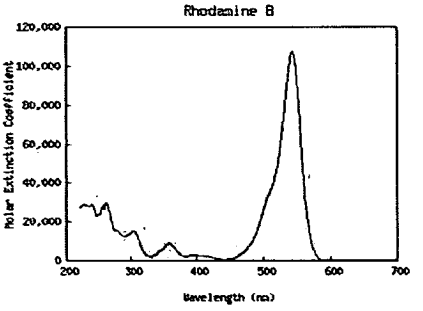

Figure 4.3: Absorption spectrum of rhodamine B[23]

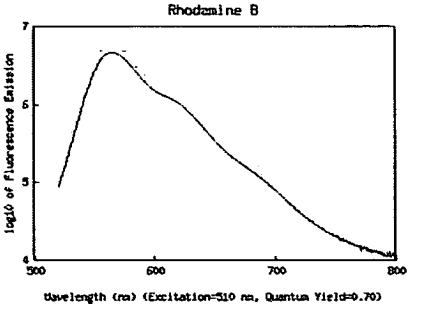

Figure 4.4: Fluorescence spectrum of rhodamine B[23]

4.3 Surface Film

Whilst it is very important that the films used for the experiment mimic the films that occur naturally, it is not practical, nor particularly environmental-friendly, to use oil or detergent. Instead, methanol was used as it has many similar properties as well as being miscible in water, buoyant and inexpensive. It also has a half-life of 1-7 days so degrades rapidly, into carbon dioxide and water, unlike similar chemicals such as Benzene [47, 49].

It should be noted that methanol is not a surfactant. However, it acts as a passive tracer, following the fluid flow rather than actively effecting it and shares

many qualities with surfactant films; forming a thin surface layer and spreading only on the water-air interface unless disturbed. Since the waves in these experiments were formed using a wave-paddle, the wind-damping effects of surfactants were unimportant and the dispersion of the surface layer was considered sufficiently similar to surfactant dispersion provided the motion is still dominated by the turbulent motion rather than buoyancy or chemical effects.

The rhodamine B was mixed with methanol, 0.001kg in 1 litre, to provide the solution for films. This concentration was used in previous PLIF experiments [67]. In addition to imitating naturally occurring surface films, the applied film must also be repeatable. This means it must be the same thickness, over the same area with the same total volume and position.

Before the film was applied, the surface had to be cleaned. Overfilling a tank is a common method for ensuring a clean surface. Since this was not possible in the tank used for these experiments, any surface dirt was removed by skimming.

Two film application methods have previously been used with this tank, each with advantages and disadvantages. The first method is simply to apply the film using a syringe. Although this ensures accuracy in the volume of film applied, it is difficult to control the position, thickness or area of the film and can lead to a small amount of dye mixing below the surface.

The second method, used by Schlicke [67], involves soaking pieces of foam,

applying the dye to the foam and "washing" the dye onto the surface. This method is faster, and the position is better defined, but it can lead to uncertainty in the quantity of dye applied and the film can be disturbed by removing the applicators.

In order to maintain the control over position, thickness and area obtained from the second method whilst enabling an accurate amount of dye to be applied, a combination of the two methods was employed. Two floats were placed on the surface of the water at the edges of where the film should spread. The dye was then applied by syringe to the surface between the floats and allowed to settle. This allowed the position and total area of the film to be kept constant whilst maintaining the accuracy of the volume achievable by the syringe method. Provided the dye was applied slowly enough, there was no mixing beneath the surface.

The area to be covered was chosen by running test experiments with films covering the entire water line and examining where the film was undisturbed following breaking. Since films do not significantly effect displacement formed gravity waves, it was unnecessary to apply a film to areas which would not be disturbed.

4.4 Illumination

In order to illuminate the working section of the tank, an Argon Ion laser was used in conjunction with a Scanning Beam Box (SBB). A more detailed explanation is given in section 3.6. The laser beam diverged as it left the source, and had to travel approximately 9 metres before reaching the SBB. By this point the beam was approximately 10mm in cross-section. In order to focus the beam again, collimating optics were used as shown in figure 4.5. The beam first passed through a converging lens then a diverging lens in order to create a narrow beam. The optimal position of the lenses was found by trial and error.

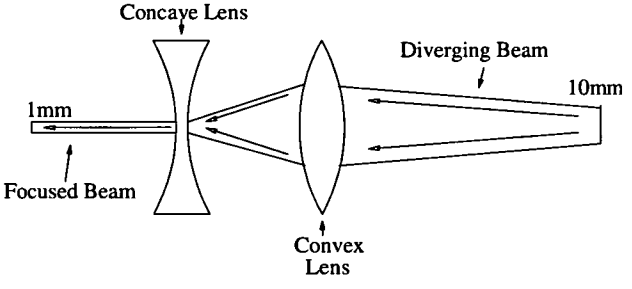

Figure 4.5: Collimating the laser beam (not to scale)

The beam width was of great importance to the experiments as the fluorescence recorded by the cameras was in fact an integral over the width of the beam. Too thick a beam may include variation over the width whereas too thin a beam would be over sensitive to out of plane motion developing after breaking. This motion is small shortly after breaking [46, 68], but with too narrow a lightsheet, these effects could have been sufficient to affect measurements. A thickness of

approximately 1mm was found to be correct.

4.5 Safety

As with any experiment, safety was of vital importance. There were three main areas of concern with these experiments in particular, as well as general safety rules that must be observed.

4.5.1 Electrical Safety

One of the greatest hazards in the laboratory environment is faulty or damaged electrics [76], particularly when combining electrical equipment with large quantities of water. The apparatus was set up with all electrical equipment held at least a few centimetres above the floor, in order to keep them clear of any spillage. The SBB was mounted on rails above the floor and the power cables were insulated and also raised at least 2cm above the floor.

By far the largest electrical current was drawn by the laser, approximately 45 amps. The laser was placed 1 metre above the floor in a separate room, adjacent to the lab, because of the restricted space available.

4.5.2 Laser Safety

The Argon Ion laser was a Class 4 laser, the most dangerous classification. Hence every precaution was taken to make the use of the laser as safe as possible. The two main areas of concern with laser safety were ensuring safety when switching on the laser, and minimising any danger from the beam itself.

Before the laser could be switched on, laser locks had to be activated on all the laboratory doors, which could only be opened from the inside or with a specific key. Activating the locks automatically illuminated the laser warning lights situated outside the laboratory. In addition, the laser could not be switched on without a laser key which only authorised users had.

Two beam dumps were positioned between the laser and the tank. The first was directly in front of the laser, inside an enclosed box, which was operated by an external handle. Once that was opened, the beam passed through copper pipes before reaching a second beam dump just before entering the room with the wave tank. The remote switch to open this dump was next to the tank, ensuring that under no circumstances could the laser be switched on and the beam travel directly into the other room. Having passed the second dump the laser travelled through more copper pipes until being reflected by a series of mirrors to run underneath the middle of the tank in the direction of the waves, as illustrated in figure 4.6. The beam was then shielded by a telescopic tube to the SBB. After the beam had been formed into a lightsheet it travelled upwards into the tank.

Any stray reflections under the tank were stopped by heavy black curtains, and once it has passed through the water the beam was stopped by a beam dump mounted over the tank.

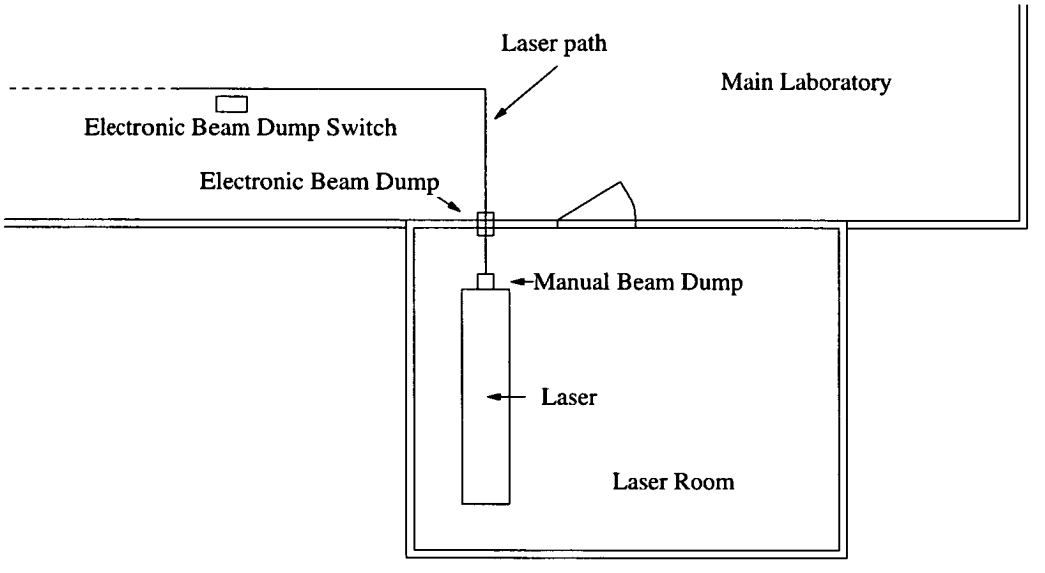

Figure 4.6: Diagram of laser path (not to scale)

4.5.3 Rhodamine Safety

Rhodamine B is classified as a "harmful" chemical if swallowed, inhaled or absorbed through the skin [48]. Therefore gloves were worn at all times when handling the solutions. As discussed is section 4.3, since the dye was mixed with methanol, it was also flammable. However, the small quantities of both rhodamine and methanol used for each experiment meant that it was never required to store a large amount of either.

4.6 Limitations and Considerations in LIF

4.6.1 Limitations of SBB

One effect of using a Scanning Beam Box was a non-integer number of sweeps per image. The motor in the SBB was accurate to only $\pm 1Hz$, creating a variation in the number of lightsheets per image as the speed varied. This resulted in certain areas receiving one more sweep of the image than others, causing a striping effect which can be seen in figure 4.7, where the red box represents the area affected by the additional sweep of the laser on the top image. The additional intensity was found to be directly proportional to the extra illumination.

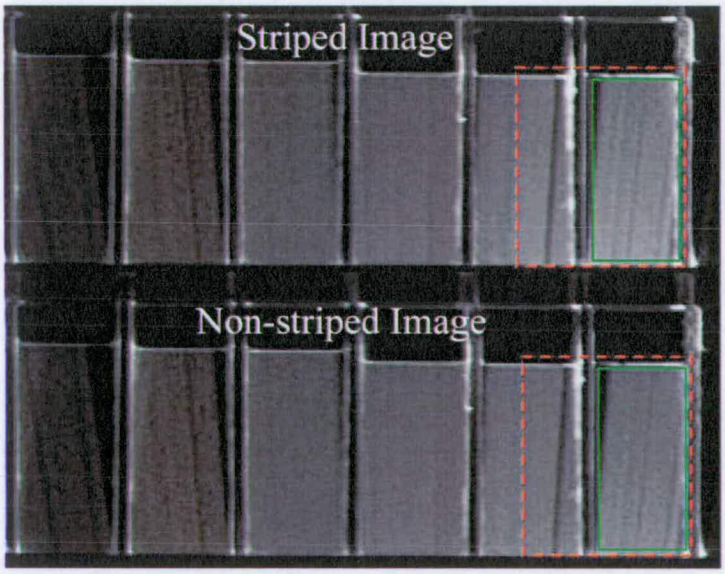

Figure 4.7: Example of striped image showing greater illumination inside red box

In figure 4.7 the mean pixel value in the green square of the top image, which

received six sweeps during the exposure, is 20% higher than the mean pixel value in the same green box of the non-striped imaged which received five sweeps. Therefore it was necessary to ensure that there were sufficient lightsheets per image to reduce the effect to a minimum.

Synchronising the camera to the start of a sweep would have also removed the problem, but would have meant the time of each image would vary from experiment to experiment. This would have created uncertainties in the time of the images and made comparisons difficult.

The SBB ran at 150Hz, corresponding to 1200 lightsheets per second and the exposure time was increased. The combination of these two steps reduced the difference in intensity of an extra sweep of the laser beam to a value comparable with camera noise and much smaller than the size of one concentration band. Therefore it did not have a significant effect on the recorded image.

4.6.2 Refractions

Air-Glass-Water

After reflecting off the rotating mirror in the SBB, the laser beam entered the bottom of the tank at an angle, causing two refractions. Refraction is the bending of light caused by a change in media, governed by Snells Law:

$$n_1 sin\theta_1 = n_2 sin\theta_2 \tag{4.1}$$

where n_1 and n_2 are the refractive indices of the original and final media respectively and θ_1 and θ_2 the angles of incidence and refraction.

The refractive index for air is 1.00, and the refractive indices for the glass and water were 1.53 and 1.33 respectively.

The change from air to glass as the beam struck the bottom of the tank caused the beam to be refracted slightly toward the normal and therefore narrowed the lightsheet. The beam was also refracted at the glass-water boundary, but this had a smaller effect than the narrowing caused by the first boundary as the difference in refractive indices was smaller. The overall effect was therefore to produce a lightsheet with a slightly more acute angle than leaves the SBB.

Water-Glass-Air

The other, more important, refraction effect was on the path of the fluorescence. The light emitted from the rhodamine must pass through two changes of media before reaching the camera: water-glass and glass-air. The overall effect was opposite to that above, and caused the angle to be increased as illustrated in figure 4.8. This means the images were slightly stretched at the edges.

This distortion was quantified by comparing the image of a $1cm^2$ grid above

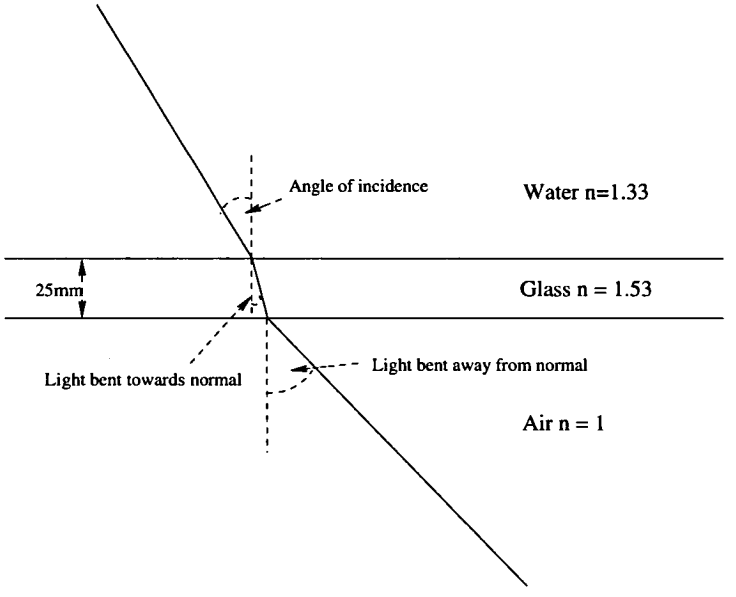

Figure 4.8: Refraction of fluorescent light

and below the water level, as shown in figure 4.9. It should be noted there is a small translation above the water caused by the air-glass-air boundaries. The total stretching effect across the image is approximately 1 cm, or 10 pixels difference between above and below the waterlevel. The percentage error introduced by this effect was far smaller than the random variations in the experiment as can be seen from the results in chapters 6 and 7.

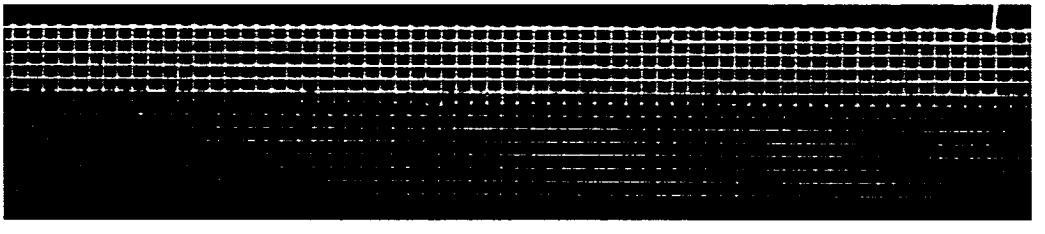

Figure 4.9: Refractive distortion of a 1cm grid above and below waterline

4.7 Camera Arrangement

The Pulnix cameras used in this study, discussed in section 3.7, were mounted to give three degrees of freedom: pitch, yaw and roll as shown in figure 4.10. They also had to be focused in the plane of the lightsheet.

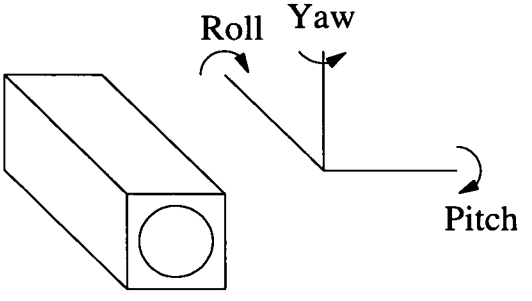

Figure 4.10: Yaw, pitch and roll of camera

4.7.1 Yaw

The 1cm^2 grid used to ascertain the distortion due to refraction in section 4.6.2 (figure 4.9) was also used to align the cameras. Where the grid lines in the figure line up vertically above and below the water, there is no refraction, which implies a zero angle. Therefore, this point is perpendicular to the camera. By making sure this point was in the centre of the image, the cameras could be positioned exactly perpendicular to the tank. A schematic showing an aligned and unaligned camera can be seen in figure 4.11. The aligned camera would show an image similar to that in figure 4.9; the image from the unaligned camera would

have the point of no distortion slightly to the right of centre (from the vertical grid line just to the right of the "line of centre of image").

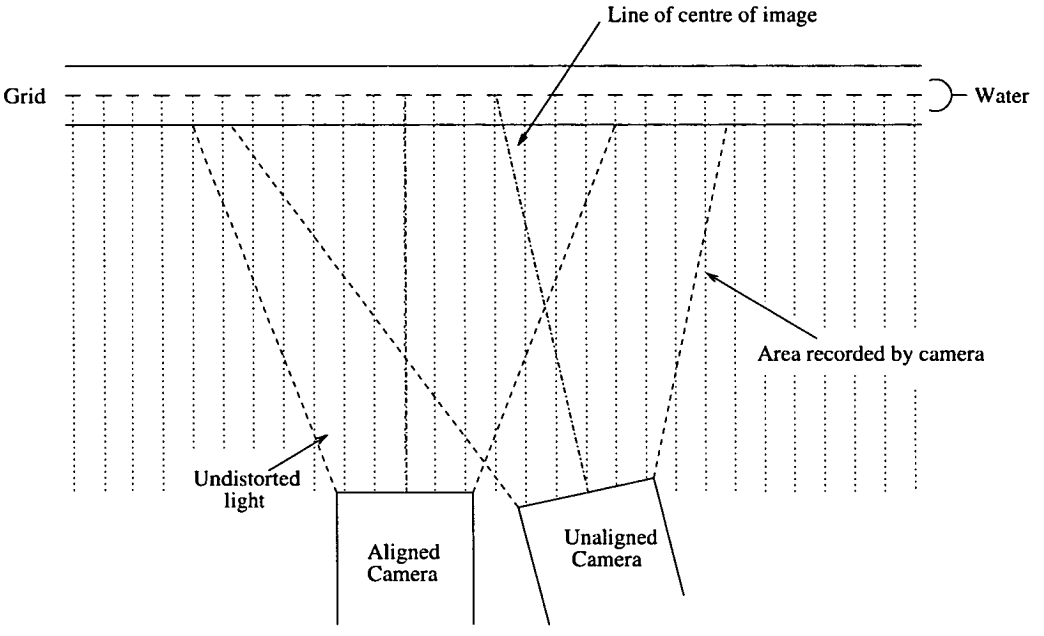

Figure 4.11: Aligning the cameras

4.7.2 Pitch

The pitch of the camera was more difficult to control. A spirit level placed on top of the camera provided one method, but this assumed the case was fitted perfectly to the camera. Additionally, a reflective surface was placed in the view of the camera. If the reflection of the lens recorded on the camera was in the in the centre of the image, then the pitch angle must be zero.

4.7.3 Roll

The roll could also be measured from the grid images. If the roll angle was zero, the vertical pixel value would remain the same for each horizontal bar of the grid, as should the water level.

4.7.4 Focus

In order to obtain sharp images, it was vital the cameras were focusing in the plane of the lightsheet. There are a number of variables involved in creating bright, sharp images; focal length, f-number, exposure time, pixel size, camera noise and sensitivity. The 28mm *MicroNikkor* lens has a focal range of 20cm to infinity and therefore could be easily focused in the plane of the lightsheet. Also, these lenses provided a broad enough angle to obtain a good compromise between distance from the experiment and resolution.

4.7.5 F-number and Exposure Time

The exposure time is the length of time the array is exposed to light. The f-number, the ratio of the focal length to the diameter of aperture, controls how much light reaches the array during this time. Both these values must be used together to ensure the images have the desired brightness. If the images were too dark then information would be lost about the lower concentration levels and,

similarly, if the images were too bright there would be a loss of separation of the higher concentrations. There were limits on both exposure time and f-number. The exposure time had to be long enough to collect sufficient light whilst being short enough not to blur the image.

The f-number had a maximum limited by the size of the lens and a minimum based on letting enough light through. Due to diffraction, a larger f-stop, that is to say smaller aperture, allows a greater depth-of-field. A narrow depth-of-field means only objects at exactly the focal distance from the camera are recorded clearly, a larger depth-of-field means objects both slightly closer and slightly further away would also be clearly recorded. In order to keep the exposure time as short as possible, and because depth-of-field is unimportant from such a narrow lightsheet, the smallest f-stop available was used, f/2.8. With this value the exposure time was set to 10,000 μs.

4.8 Preparing Images

Before the images can be analysed, they need to be pre-processed. There were three stages to this; correction for background and lightsheet variation, banding the images and joining them together. Two thousand images were recorded from each experiment, one thousand from each camera. Due to the large number of images taken, all processing and pre-processing was done computationally. A flow

diagram to represent the process is shown in figure 4.12.

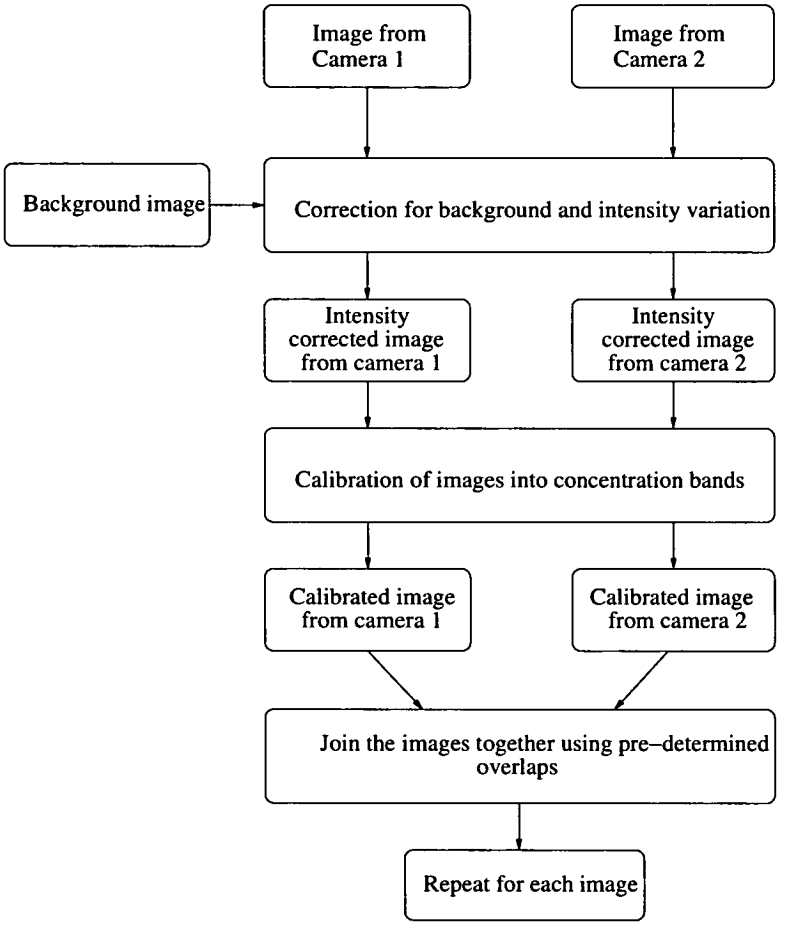

Figure 4.12: Flow Diagram for image preparation

4.8.1 Lightsheet Correction

The first stage of pre-processing was correcting for variation in the lightsheet. Initially, the pre-processing computer program loaded the images from the left camera along with a background image. Background images were taken after

each experiment to show the variation of the lightsheet and the concentration of dye in the thoroughly mixed water. There was a slight over-estimate in the background levels, since the background image also includes the additional dye which had been on the surface prior to the experiment but does not contribute before the wave breaking occurs. However, this slight discrepancy did not affect the shape of the lightsheet variation, primarily caused by the decrease in power depending on distance from source. The grey-level of each pixel was taken and scaled according to the background image using the following formula:

$$Level = \frac{RawLevel}{BackgroundLevel} * Scale \tag{4.2}$$

The scale factor was chosen to ensure the final image was neither too bright nor too dark, with the smallest concentrations corresponding to nearly black and the largest measured concentrations white. Having swept through one image like this, the image from the second camera received the same processing so both had been corrected for background. Since different CCD arrays have slightly different characteristics, the scale factor could be different for each camera.

4.8.2 Calibration

The next stage in pre-processing was to calibrate the images into bands. Although having removed the variation in lightsheet intensity the fluorescence of the dye

should be purely related to the concentration of the dye, there are still a few causes of deviation. Camera noise could cause the recorded grey-level to fluctuate, as described in section 3.7, even though the actual fluorescence is constant. Also, the scanning beam nature of the illumination means certain areas could have received more or less sweeps of the beam, as discussed in section 4.6.1.

Since the cameras record in 8-bit grey-scale, each pixel was assigned a value from 0-255 depending on its intensity, with 0 corresponding to black and 255 white. As random effects could be reduced to ± 5 pixel intensity, the 12 band system used by Schlicke [67] was used, as explained below.

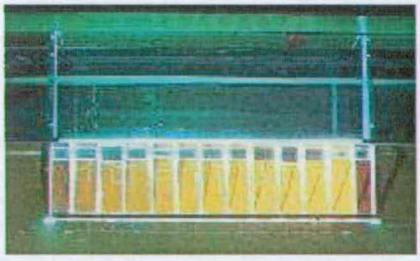

Figure 4.13: Photograph of calibration vessel

In order to make a direct connection between fluorescence and concentration, images were taken of a calibration vessel. The vessel, shown in figure 4.13, consists of 13 compartments each containing a known concentration of Rhodamine solution.

By recording the fluorescence of each section it was possible to calibrate the grey-scale images such that the largest concentration was shown as white and the

smallest as black, as can be seen in figure 4.14. Calibration was done by taking an average of a square of pixels illuminated directly by the laser beam within each compartment.

Figure 4.14: Image of calibration vessel

The levels in between could then be spaced evenly to represent the other concentrations, as shown in table 4.1.

Concentration / %	Pixel Level	Concentration / %	Pixel Level
<0.0005%	0	0.005 <= C < 0.0075	148
0.0005 <= C < 0.001	21	0.0075 <= C <0.01	170
0.001 <= C < 0.0015	42	0.01 <= C < 0.0125	191
0.0015 <= C < 0.002	63	0.0125 <= C < 0.015	212
0.002 <= C < 0.003	85	0.015 <= C < 0.02	233
0.003 <= C < 0.004	106	> 0.02	255
0.004 <= C < 0.005	127		

Table 4.1: Concentrations corresponding to each pixel value

4.8.3 Joining the Images

Once each image had been corrected for lightsheet variation and calibrated, it needed to be joined with its partner image taken at the same time on the other camera. This was done using custom written software in the language QT2. In order to allow accurate alignment, there was a small overlap between the two

images, typically of 8 pixels, which could be used to test by eye if the images lined up on a sample combined image. There may also have been a slight height discrepancy between the two images. By inputing the the overlap values, the software was able to account for both horizontal and vertical overlaps. The original images were 768 x 484 pixels, which means the final image was 1528 x 484 pixels.

Once this process had been completed, it was repeated for each of the 1000 images from an experiment. The final images were then fully pre-processed and ready for analysis.

4.9 Summary

In this chapter, the process of Planer Laser Induced Fluorescence (PLIF) was introduced and explained. A brief summary was given of the surface films and illumination used for these experiments along with a discussion of safety issues. The limitations and consequences of using PLIF were also discussed with explanations of how they were accounted for.

Chapter 5

Obtaining Results from PLIF

5.1 Introduction

In this chapter the process of obtaining results from PLIF is discussed. Five results were obtained: depth of the mixing for each concentration; area of mixing for each concentration; the motion of the centre of mass of the film; the dispersion of the film and the fractal dimension of the film, all as functions of time.

5.2 Depth

Of primary interest was how deep the mixing had penetrated following breaking. As with all the processes to extract information, measuring the depth was done

computationally. Each image was loaded into the analysing computer's RAM and scanned through pixel by pixel by the analysis program, recording the greatest depths reached by each of the 12 concentrations. In order to register a given point as the deepest, it had to be no greater than the values occurring either side of it. This ensured camera noise, or other random point sources near the bottom of the image, did not bias results.

The depth was measured relative to the MWL, as defined in section 2.3.1, rather than the moving surface in that image. This reduced the computational time and complexity significantly, as it did not require a correction for a moving surface, without affecting the results for more than a couple of seconds following breaking. From this information, it was also possible to calculate a rate of descent for the mixing.

5.3 Area

Another important measurement was the area covered by the individual concentrations as they spread. During the scan through the image described in the previous section, the number of pixels of a given intensity was also recorded. The total area for each concentration could then be measured. This could also be used to calculate the speed with which the dye patch was expanding and diffusing.

5.4 Centre of Mass

Once the area information for each concentration had been measured, it was possible to obtain a "2D" mass for the film; the *0th moment*, defining a moment as:

$$m_{i,j,k} = \int\int\int x^i y^j z^k f(x,y,z,t) dx dy dz \tag{5.1}$$

where f(x,y,z,t) is the concentration. This simplifies to f(x,y) as z is fixed by the position of the lightsheet and the time, t, is constant for each image.

More precisely, for these experiments, the moments were:

$$m_{i,j}^{expt} = \sum\sum x^i y^j f(x,y) \tag{5.2}$$

The centre of mass of the film could be obtained by dividing the 1^{st} moment by the 0^{th} moment, the 1^{st} moment having also been calculated during the original scan through the image. It was therefore possible to track the centre of mass and motion of the film as a whole.

It should be noted that there was dye entering and leaving the lightsheet due to the developing 3D motion after breaking. However, these motions are random in nature and therefore had a small effect on the total 2D mass of the film.

5.5 Dispersion

The images were taken from fixed cameras, meaning the measurements were Eulerian. It is usually better to measure dispersion from a Lagrangian frame of reference, moving with the particles that are dispersing. However, connecting the two reference frames in not a simple task [78].

The basis of dispersion is that particles starting very close together will follow different paths in space, getting further apart on average as time continues. There are a number of mechanisms that lead to this spreading; molecular diffusion, advection, shear dispersion and turbulent diffusion.

5.5.1 Molecular Diffusion

Molecular diffusion is the spreading of particles due to motions on an atomic scale. The random movement of molecules, caused by thermal excitation, means they travel further away from their starting position as time increases. This spreading is referred to as *diffusion* and can be described using either concentration gradients or a "random walk" model of the particles of fluid.

The relationship between the mass flux, $\mathbf{q}$, and concentration gradient in that direction is known as *Fick's equation*:

$$\mathbf{q} = -\mathbf{D}\nabla C \tag{5.3}$$

where **D** is the *diffusion coefficient* and C is the concentration. When combined with the conservation of mass, the diffusion equation (5.4) is obtained:

$$\frac{\delta C}{\delta t} = -D\nabla^2 C \tag{5.4}$$

Solving this equation in one-dimension gives:

$$C(x,t) = \frac{M}{\sqrt{4\pi Dt}} e^{\frac{-x^2}{4Dt}} \tag{5.5}$$

where M is the total mass of the diffusing substance. The above equation can also be derived from the probability distribution of a large number of particles obeying a random walk, combined with the central limit theorem.

It is important to demarcate an edge to the dispersion. This is defined as the point where the concentration falls to below $\frac{1}{e^2}$. When the process is entirely random, for example Brownian motion, its size is expressed in terms of the standard deviation, σ as:

$$\sigma = (2Dt)^{\frac{1}{2}} \tag{5.6}$$

where t is time.

When the motion is not entirely random, and particles have a tendency to either mimic or oppose the previous move, the exponent is no longer $\frac{1}{2}$. This is called *Fractional Brownian Motion* and is discussed in section 5.5.5.

5.5.2 Advection

When the dispersion happens within a medium that also has a mean flow, velocity u, the net transport of the dispersing substance is referred to as *advection.* Advection can be accounted for by adding a uC term to equation 5.3 giving

$$q = uC - D\nabla C \tag{5.7}$$

The diffusion equation (5.4) now becomes

$$\frac{\delta C}{\delta t} + u.\Delta C = -D\nabla^2 C \tag{5.8}$$

5.5.3 Shear

For non-uniform velocity flows *u(x,t)*, there will be a velocity gradient, or shear, present in the motion. This differential in advection will cause the pollutant to spread faster and is called *dispersion.* Often this dispersion is far faster than the

molecular diffusion, to the extent that in the mixing process molecular diffusion can be effectively ignored and the spread of the pollutant is driven by variations in the fluid motion rather than random thermal interactions.

However, the form of $u(x,t)$ can often be very complex, and therefore equation 5.8 may not be soluble analytically. In these cases, an experimental or numerical approach must be taken to understand the resulting dispersion.

5.5.4 Turbulent Diffusion

The previous example of advection assumed an exactly known, if complicated, flow $u(x,t)$, but often this is not the case. Turbulent flow is responsible for even greater mixing than a steady mean flow. *Turbulent diffusion* is usually treated mathematically, assuming that the turbulence is both isotropic and homogeneous with no mean flow.

Tracking a fluid particle moving in such a turbulent flow, the mean square of its displacement from its starting position at time $t = 0$ is proportional to t^2 for small t and to t for large times, first calculated by Taylor [74]. Since a pollutant can be thought of as large number of individual particles all obeying this rule, the variance of the spreading increases as t, implying the standard deviation increases as $\sqrt{t}$.

Although this result is analogous to molecular diffusion at large t, governed

by a "random walk", the dispersion coefficient is significantly larger for turbulent diffusion than molecular diffusion. For small t, the result is analogous to advection.

However, at intermediate t, the spread is governed by Richardson diffusion [28, 62]. Richardon's law, obtained by considering the separation of particle pairs states that the size of the cloud, σ, determines the diffusion coefficient, D, such that:

$$D \propto \sigma^{\frac{4}{3}} \tag{5.9}$$

This means the diffusion coefficient is increasing as the cloud size increases; it expands with increasing rapidity.

5.5.5 Fractional Brownian Motion

Random Brownian motion predicts the size of a dispersion cloud in terms of the standard deviation, as shown in equation 5.6. However, when the motion is not entirely random the dispersion can be referred to as *fractional Brownian Motion* and the standard deviation generalised by introducing the *Hurst Exponent, H*:

$$\sigma = (2Dt)^H \tag{5.10}$$

where $H = \frac{1}{2}$ for normal Brownian motion. The variation between fractional and normal Brownian motion is a dependence of the current step in a random walk on the previous motion. Equation 5.6 assumes that each step is entirely without correlation with the previous, or any other, step. If the current motion is influenced by the previous direction, then the motion is no longer random but contains a pattern, albeit only visible on a statistical scale.

When the particle is more likely to oppose the motion of the previous step, the process is called *subdiffusive* or *antipersistent* and the cloud will grow at a slower rate than random motion with

$$0 < H < \frac{1}{2} \tag{5.11}$$

If the particle is more likely to continue in the same direction, the process is called *superdiffusive* or *persistent* and the cloud will grow at a faster rate than random motion with

$$\frac{1}{2} < H < 1 \tag{5.12}$$

Therefore, by measuring the hurst exponent, it is possible to examine whether the mixing is sub- or superdiffusive and how it may continue in long time scales.

5.5.6 Quantifying the Dispersion

All of the processes discussed in sections 5.5.1 to 5.5.5 may be present in any mixing. Although each have formulae to calculate their contribution to the dispersion, it is virtually impossible to separate the effect of each in experimental results. Therefore, it is sometimes more appropriate to treat the entire dispersion using fractional Brownian motion. Since any measurement will apply only to the section of the flow being investigated and may not be fractional Brownian motion, any calculated exponent may not be exactly the Hurst exponent, and should therefore simply be referred to as a dispersion exponent.

Equation 5.10 enables the evaluation of a dispersion coefficient, D, and a dispersion exponent H by taking the logarithm of each side

$$log\sigma = Hlogt + Hlog(2D) \tag{5.13}$$

Plotting $\log \sigma$ against $\log t$, H and D can be calculated from the gradient of the slope and intercept respectively. The variance of the concentration distribution can also be calculated as the ratio of the 2^{nd} order moment to the 0^{th} order moment, as defined in section 5.4.

Dispersion coefficients and exponents were also measured to quantify the area covered by the film and the depth reached in a similar manner to Schlicke [67].

This enables direct comparisons to previous experimental results, discussed in section 8.4.

5.6 Fractal Dimension

Once the film has settled on the surface of the water, it is approximately 10^{-7}m thick, six orders of magnitude thinner than the depth of the tank and therefore the film can be treated as essentially two-dimensional. The lightsheet produced by the SBB is two orders of magnitude thinner than the tank width, and can also be treated as a plane. The interception of the two planes produces a line, and therefore prior to breaking, there is a thin line of fluorescence on the water's surface.

Once the breaking wave has dispersed the film beneath the surface, the depth component of the film is no longer negligible compared to the width and length, and the dye becomes essentially three-dimensional. The intersection of a volume and a plane is also a plane, and it is in this intersection plane that the fluorescence is seen and recorded.

However, as seen in figure 5.1, it is clear the dispersion does not entirely occupy the plane. The outline of the film, which prior to breaking was one-dimensional on the surface alone, has now spread below the surface but has not fully developed into a two-dimensional plane. This transition, of both the film

itself and the outline, can be described using a *fractal dimension.*

Although the most commonly used definition of dimension is the topological dimension, there are many different definitions [54]. The topological dimension D_t, is an integral measure such that all arcs have a value of one; all areas, two; all volumes three, and so on. There is no room for fractionality in the topological dimension. Motivated by a need to find a way of quantifying the dimension of shapes which do not fall neatly into one of these categories, other dimensions were defined.

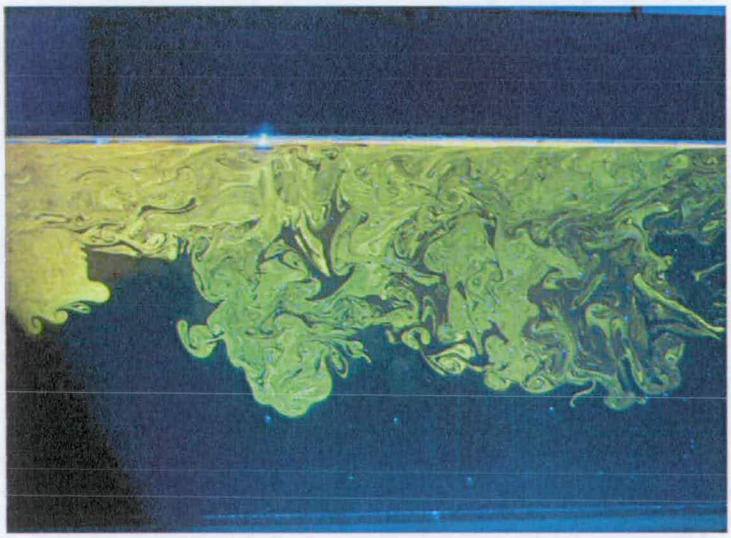

Figure 5.1: Photograph of PLIF

The notion of dimension that is best fitted to application in science is the *Box Counting Dimension*, which is an adaptation of Mandlebrot's original *Fractal Dimension*, itself a adaptation of the *Hausdorff* dimension derived by the Felix Hausdorff in 1919. A full description of the Hausdorff dimension can be found in

Peitgen [54] but a brief summary is provided here.

The definition of a fractal has altered since it was proposed by Mandlebrot [1]. Currently, it is accepted that a fractal is a shape whose parts are in some way similar to the whole. This definition can applies to fluorescent area of mixing in these experiments, as seen in figure 5.1.

A structure is said to be strictly self-similar if it can be split into smaller pieces each of which is a perfect replica of the original. If the smaller pieces look very much the same as the original but are not identical, then they are statistically self-similar rather than strictly self-similar. Such structures are common in nature; trees, cauliflower and broccoli for example.

Turbulence can be shown to be an example of statistical self-similarity [11, 56]. Fractal geometry has also been used with other naturally occurring processes such as cloud formation [40], cracking concrete [51], occurrence of breaking waves [37], coastlines [44] and even price fluctuations in the stock market [45].

A simple, but important, example of strict self-similarity is a line, as shown in figure 5.2. The number of sections the line is split into is entirely arbitrary, they are always perfect replicas.

A square can be split in a similar manner, but only if split into a square number of pieces, i.e. 4, 9, 16 etc. A cube can also have self-similarity if split into 8, 27, 64 etc. It should be noted that self-similarity does not imply the

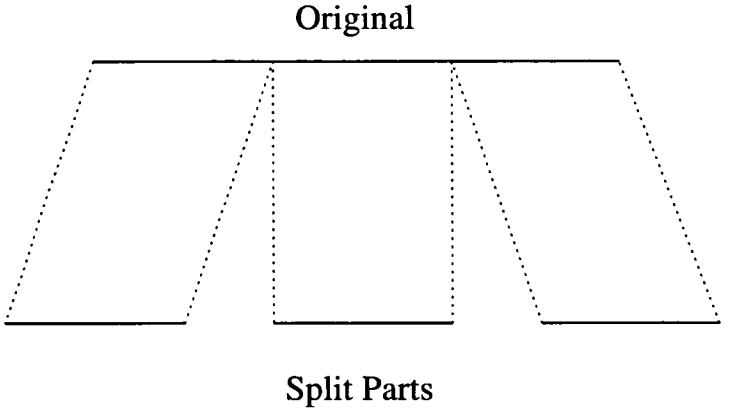

Figure 5.2: Simple self-similarity

shape requires a fractal description, as a line, square or cube do not. However, self-similarity is an important feature of fracture structures, such as the Koch curve, shown in figure 5.3.

With every iteration in a Koch curve, each straight section is replaced with the original 1st iteration Koch curve, so with each passing step the outline becomes more complex. This can be seen from figure /reffig:koch where the curve is always more complex than th one above. In purely mathematical terms, there is no limit on the number of iterations that can be performed.

In can be seen that the Koch curve exhibits the same strict self-similarity as the line or square. There are four smaller copies of the 1st iteration in the structure of the second iteration, each $\frac{1}{3}$ the size. For lines, squares and cubes, the reduction factor in the separated sections was equal to the number of sections produced. Hence, there could be nine self-similar squares obtained from one

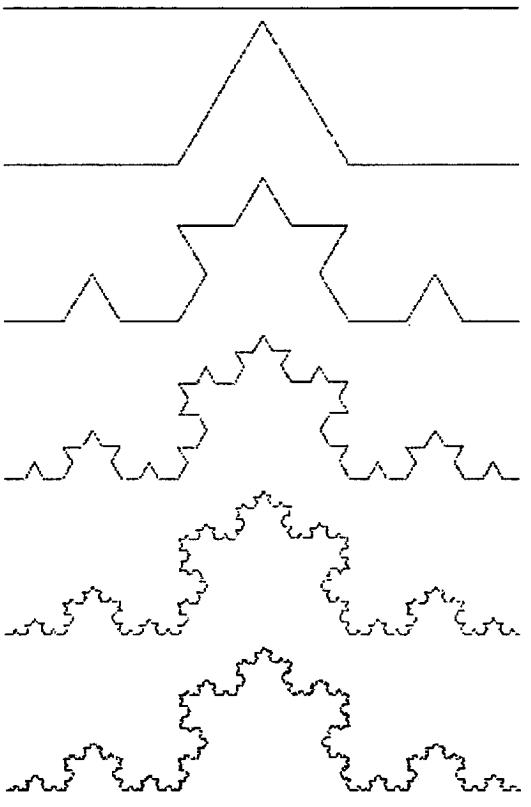

Figure 5.3: First five iterations of Koch curve (from top to bottom)

square, each a ninth the size of the original. However, this is not the case for the Koch curve; there are four self-similar Koch curves, each one third the size. It is this difference which separates fractal and non-fractal structures when measured in this way. For the line, square and cube there is a simple relationship between the number of pieces, n, and their reduction factor from the original, r:

$$n = \frac{1}{r^D} \tag{5.14}$$

where D is 1, 2 and 3 for the line, square and cube respectively. Therefore D corresponds exactly to the accepted topological dimension for those structures. However, for the Koch curve, $n = 4$ and $r = \frac{1}{3}$. Rearranging equation 5.14 and defining $R = \frac{1}{r}$ gives:

$$D = \frac{\log n}{\log R} \tag{5.15}$$

If the number of self-similar parts extracted from the Koch curve increases to sixteen, then each is a ninth of the size of the original, essentially squaring n and R, which due to the nature of logarithms cancels top and bottom and the equation remains the same. Therefore, solving for D in the simplest case gives the value of D for all cases, which is 1.2619 to 5 significant figures. This is referred to as the *self-similarity dimension* of the Koch curve.

Not all curves are as easy to define as the Koch curve, and most naturally occurring structures do not show strict self-similarity. For these shapes, the *box-counting dimension* is a more appropriate measure. The box-counting dimension proposes a systematic measurement which can be applied to any structure regardless of the topological dimension it exists within. The structure is placed with a regular mesh with side length s and the number of boxes of the mesh containing

a piece of the outline, $N(s)$, is counted. This is shown in figure 5.4 using the Koch curve, a 5 by 17 grid and an arbitrary s of 1.

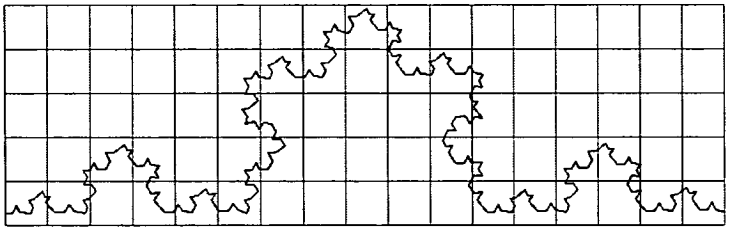

Figure 5.4: Box-counting grid with s = 1

There are 35 grid squares containing an outline, as shown in figure 5.5.

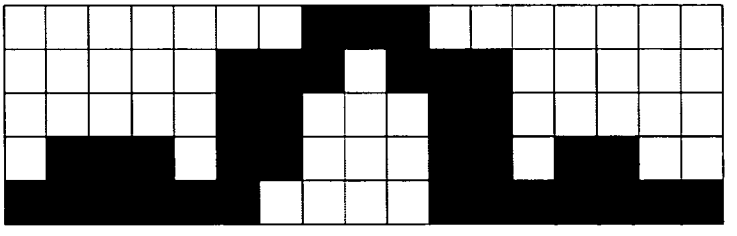

Figure 5.5: Box-counting grid with filled squared counted (s=1)

By decreasing the size of s, $N(s)$ will increase accordingly. Figure 5.6 shows the same Koch curve covered with a 10 by 34 grid with an s of $\frac{1}{2}$. There are ninety-six grid squares containing a section of outline, as shown in figure 5.7.

This process is easy to recreate computationally for a large range of s values. Plotting log N(s) against log $\frac{1}{s}$ gives an approximately straight line. The gradient of this line is the box-counting dimension. Using only two values for s, the example above calculated the box-counting dimension to be 1.45, compared to

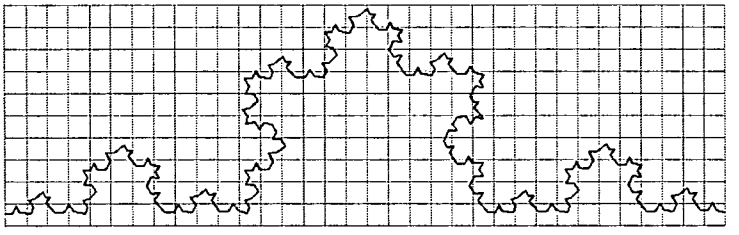

Figure 5.6: Box-counting grid with s = $\frac{1}{2}$

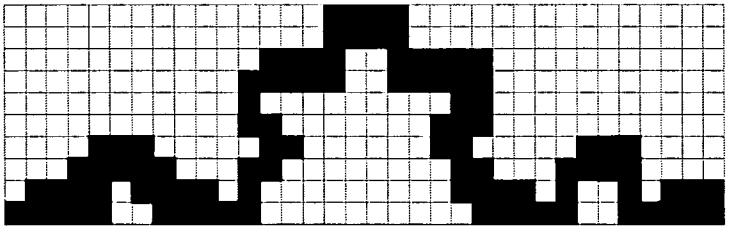

Figure 5.7: Box-counting grid with filled squared counted (s=$\frac{1}{2}$)

the self-similarity dimension of 1.26. This is not a bad estimate using only two grid sizes, and up to 46 grid sizes are used to calculate results in this Thesis.

Further reading can be found in Edgar [25] or Feder [27].

5.6.1 Measuring the Dimension

Practically, the relationship between $N(s)$ and s will not be an exact line. Therefore, when analysing the images, a least-squares algorithm was used to provide a best fit to the data. Also, there was a minimum length scale set by the size of an individual pixel, s cannot be shorter than this size. The upper limit on s was set by the size of the dispersion, if a single grid square contains the entire dispersion;

the dimension will be calculated to be one. Therefore, it was only meaningful to attempt to calculate the dimension over a range of s fitting to the experiment.

5.7 Conclusions

In this chapter the methods of obtaining results from PLIF images were discussed. Five parameters are measured: depth reached for each concentration value, area covered by each concentration value, centre of mass motion, dispersion and fractal dimension. An explanation of the process used to calculate each of these values was given.

Chapter 6

Single Breaker Results

6.1 Introduction

In this chapter the quantities discussed in chapter 5 are calculated and presented for single breakers with non-dimensional amplitudes from 0.314 to 0.352. Previous work has been carried on dispersion by single breakers [59, 67] but did not cover as wide a range of amplitudes or give as much emphasis on the relationship between amplitude and the measured parameters.

Sample images from an experiment which may be useful in the discussion of results can be found in Appendix A.

6.2 Qualitative Description of Breaking

Once the film had been applied and settled on the water's surface, it remained undisturbed until a breaking wave passed. Non-breaking waves caused the film to translate in the direction of the wave motion due to Stoke's drift, but there was very little downward mixing.

As the breaking wave approaches, the film still follows the water's surface. At the point of breaking, when the air is entrained into the water, the film is finally broken and begins to mix. The dye directly beneath the jet of the plunging breaker is pushed downward, entraining more dye, and the energy provided by the breaking fuels turbulent dispersion. In addition to this, the splash up from the plunging tip forms a second area of dispersion further upstream. The two areas then overlap to form one larger area. The process of mixing continues while the eddies and turbulence gradually transfer their energy to smaller scales until motion finally dies out and molecular diffusion, chemical and buoyancy effects take over the dispersion. For spilling breakers, the process is very similar but with a smaller secondary splash up effect and smaller and slower eddies.

In the experiments involving a second breaking wave, the second breaker occurred 32 seconds after the initial breaker, the time interval being limited by the input conditions to the wave paddle, while turbulent motion still dominated the mixing. The motion from the first breaking wave was still evident but was

quickly swamped by the turbulence created by the second breaker. Unlike the first breaking wave, the dye was no longer on the surface but had already been dispersed.

Seven ak values were attempted, ranging from 0.314 to 0.352, with amplitudes from 0.099m to 0.111m respectively and k_c equal to $3.17m^{-1}$, covering from very mild spilling breakers up to large plungers, as shown in table 6.1.

Amplitude(m)	ak value	Breaker Type
0.099	0.314	Spiller
0.101	0.320	Spiller
0.103	0.327	Spiller
0.105	0.333	Spiller/Plunger
0.107	0.339	Plunger/Spiller
0.109	0.347	Plunger
0.111	0.352	Plunger

Table 6.1: Breaking waves investigated

Of these values, 0.314, 0.333 and 0.352 were also used by Schlicke, and 0.352 by Rapp and Melville, allowing comparisons to be made, whilst the other amplitudes served to increase the body of knowledge.

6.3 Maximum Depth Results for Single Breaker

The maximum depth for each concentration was measured as a function of time. In the following sections, plots of non-dimensionalised depth against non-dimensionalised time are presented for different amplitudes. The time axis represents the time

since the breaking event, non-dimensionalised using the angular frequency of the central wave; $\log\omega_c t = 1$ therefore represents the time of breaking.

Table 6.2 shows the relationship between time following breaking and $log_{10}\omega_c t$.

Time after breaking (seconds)	$log_{10}\omega_c t$
5	1.44
10	1.74
15	1.92
20	2.04
25	2.14
30	2.22
35	2.29
40	2.34
45	2.40
50	2.44

Table 6.2: $log_{10}\omega_c t$ - Time relationship

The depth is measured relative to the mean water level, non-dimensionalised using the central wavenumber. Measurement from the mean water level results in exaggerated peaks and troughs in the graph around the breaking event but produces accurate results once the surface motion has been damped. This was approximately four seconds after breaking in the experiments described here.

Table 6.3 shows the actual depth in metres and wavelengths for a range of $log_{10}k_c d$ values.

For each breaking wave amplitude, a sample result is presented. It is important to note that the maximum depth, as defined in section 5.2, is recorded and not the average depth. Therefore these results are very sensitive to the turbulent

$log_{10}k_cd$	Depth(m)	Wavelengths(λ)
0	0.32	0.16
-0.1	0.25	0.13
-0.2	0.20	0.10
-0.3	0.16	0.08
-0.4	0.13	0.07
-0.5	0.10	0.05
-0.6	0.08	0.04
-0.7	0.06	0.03
-0.8	0.05	0.03
-0.9	0.04	0.02

Table 6.3: $log_{10}k_cd$ - Depth relationship

nature of the mixing. The area and centre of mass results present more precise indications of the film motion as a whole.

The $log_{10}k_cd$ values can be converted back into actual depths in metres with the following equation:

$$MaximumDepth = \frac{10^{log_{10}k_cd}}{3.17} \tag{6.1}$$

This can then be converted into fractions of a wavelengths or waveheights using table 6.1.

The percentages represent the concentration of the dye, with 100% corresponding to the concentration of the undiluted rhodamine B solution.

Gradients and intercepts are calculated by plotting the data using the software Tecplot 9. Linear approximations are calculated using a least square fit also using

Tecplot 9. Errors and uncertainties are not included, as the random nature of the experiments mean the variations between individual experiments are larger than the uncertainty in using the least square fit.

6.3.1 Maximum Depth Results for Single $ak = 0.314$ Breaker

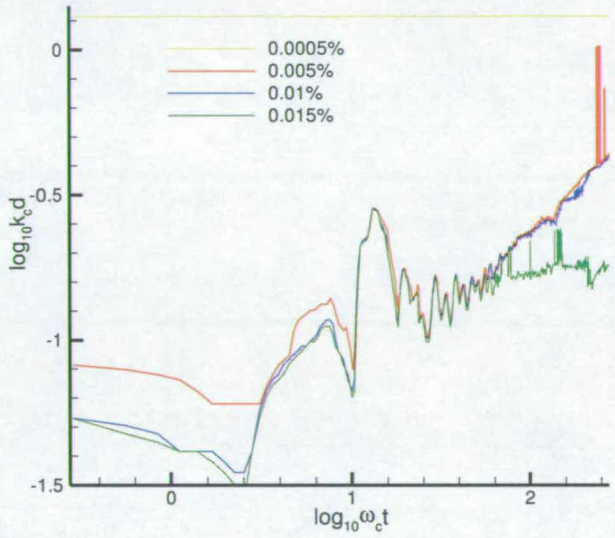

Figure 6.1: Depth against time for single ak = 0.314 breaker

Immediately following breaking, the maximum depth of all measurable concentrations increases. The smaller concentrations descend further than the larger, as should be expected. The line for 0.0005% represents background dye; since this background level is thoroughly mixed through the water column, the maximum depth indicated by this line corresponds to the bottom of the tank.

It should be noted that a higher value on the $\log_{10}k_cd$ scale means a greater depth in the tank and an increase in maximum depth means an increase in the depth reached by the dispersing film.

The largest concentration, 0.015% descends to a depth of $log_{10}k_cd$ = -0.8 (corresponding to approximately 5cm, $\frac{1}{40}$ wave length or half a waveheight) and then remains steady between $\log\omega t = 1.8$ and the end of the recording. This can be compared to the experimental images in Appendix A of an $ak = 0.346$ breaker.

The line of 0.005% shows a linear relationship between $\log\omega t = 1.6$ and the end of the experiment, with a gradient of 6.05×10^{-1} and intersection at -1.83. This corresponds to a dispersion coefficient, calculated using $\frac{10\frac{c}{H}}{2}$ from equation 5.13 where c is the intercept and H the dispersion exponent, of 4.72×10^{-4}.

The intercept c, is very sensitive to the time over which the linear region appears, and a small change in position can create a large difference in calculated dispersion coefficient. Therefore, the most important results measured from the maximum depth results are the gradient of the $log_{10}k_cd$ - $log_{10}\omega_ct$ relationship, which shows how the dye is ascending or descending, and the final maximum depth reached, which indicates how far the dye is penetrating beneath the surface.

Assuming no other disturbance, the depth reached by the film d, with respect to the time following breaking will be given by

$$k_c d_{0.005\%} = (9.45 \times 10^{-4} \omega_c t)^{0.605} \tag{6.2}$$

Although this steady increase continues to the end of the experiment, it would be limited simply by the mass of dye available. As can be seen from later experiments, the maximum depth reached and area of higher concentrations falls as the experiment progresses as it fuels dispersion into lower concentrations. Over a significantly long time, even the lowest levels measured here would exhibit the same behaviour.

The dispersion exponent is greater than 0.5, which implies the process is super-diffusive. This may be due to the additional turbulent eddy motion which causes the dye to spread faster than a standard random walk.

The line inbetween these two concentrations, 0.01%, is closer to the lower concentration than the higher. Between four seconds ($\log\omega_c t = 1.2$) and the end of the experiment the graph shows a linear growth with a gradient of 5.89 $\times 10^{-1}$ and intercept of -1.81.

The final depth values of the three concentrations are $log_{10} k_c d$ = -0.74, -0.37 and -0.36 for 0.015%, 0.01% and 0.005% respectively. A summary of these results, with results for larger breaking waves, is presented in section 6.3.8.

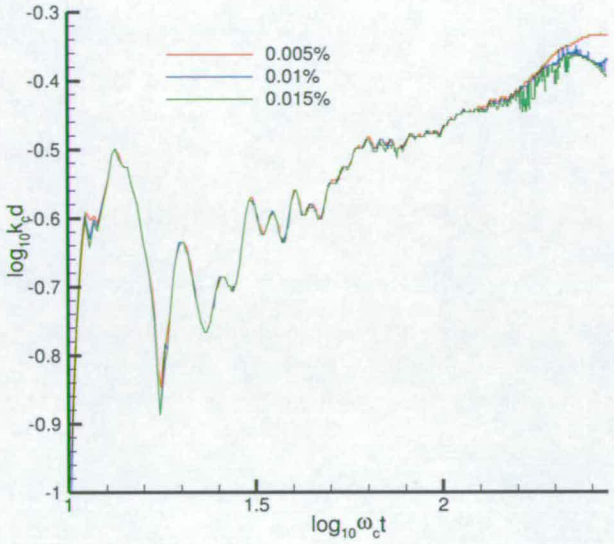

Figure 6.2: Depth against time for single ak = 0.320 breaker

6.3.2 Maximum Depth Results for Single $ak = 0.320$ Breaker

The maximum depth reached by the same three concentrations; 0.005%, 0.01% and 0.015% for a breaking wave with an ak value of 0.320 are plotted in figure 6.2. The depths reached by all three levels are very similar, reaching depths approximately the same as the lower concentration in the $ak = 0.314$ breaker. This suggests, in this result, the larger concentrations remained together with the smaller concentrations, pulled down by the turbulent motion. The smaller spilling breaker produces smaller eddies, and therefore the larger concentrations penetrate a similar depth to the lower ones.

Between $\log\omega_c t = 1.6$ and 2.1, all three selected values show a steady increase,

with gradients of 2.48 $\times 10^{-1}$ for 0.015%, 2.59 $\times 10^{-1}$ for 0.01% and 3.02 $\times 10^{-1}$ for 0.005% . All three of these results suggest anti-persistent dispersion, although the region logω_ct = 1.1 to 1.6 shows rapid depth increases for all three concentrations and this may affect the final results. If a small patch of dye containing a wide range of concentrations was carried downward near the start of the mixing; this would skew the maximum depth results.

After this linear region, the 0.015% and 0.01% concentration maximum depth begins to decrease; i.e. getting closer to the surface. The dye is dispersing and hence the dye at the greater depth is being diluted and fuels the continued descent of the lower concentrations, rather than the greater concentrations actually ascending.

The final depths reached by the three concentrations were $log_{10}\omega_c t$ = -0.40, -0.37 and -0.33 for 0.015%, 0.01% and 0.005% respectively.

6.3.3 Maximum Depth Results for Single $ak = 0.327$ Breaker

The next largest breaker had an ak value of 0.327 and the maximum depth results are shown in figure 6.3.

The upper red line, representing 0.005%, follows an approximately linear path from $log_{10}\omega_c t = 1.4$ (approximately four and a half seconds after breaking) until $log_{10}\omega_c t = 2.1$. The equation of this line is $log_{10}k_c d = 3.40 \times 10^{-1}\ log_{10}\omega_c t - 1.06$,

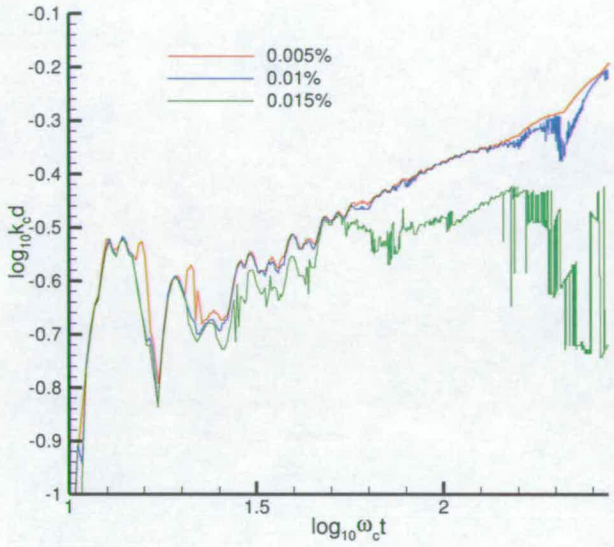

Figure 6.3: Depth against time for single ak = 0.327 breaker

giving a dispersion coefficient of 3.81 $\times 10^{-1}$.

The lower green line represents the 0.015% concentration. Between $log_{10}\omega_c t =$ 1.8 and 2.1 the graph is also linear, with a gradient of 2.20×10^{-1}. The dispersion co-efficient is calculated to be 3.26×10^{-5}.

After this linear section the maximum depth value fluctuates between $log_{10}k_c d =$-0.5 and -0.75. This is due to small patches of dye entering and leaving the light-sheet at the lower depth.

The line representing the maximum depth reached by the 0.01% concentration is much closer to the 0.005% line than the 0.015% line. Over the same range as

the lower concentration, it shows a roughly linear growth with a gradient of 3.27 $\times 10^{-1}$ with a similar intercept. Near the end of the experiment, the graph shows a very sharp decrease in maximum depth. This is caused by a patch of dye being pulled downward by an eddy.

The final maximum depths reached by the three concentrations are $log_{10}k_cd$ = -0.72, -0.22 and -0.19 in order of decreasing concentration.

6.3.4 Maximum Depth Results for Single $ak = 0.333$ Breaker

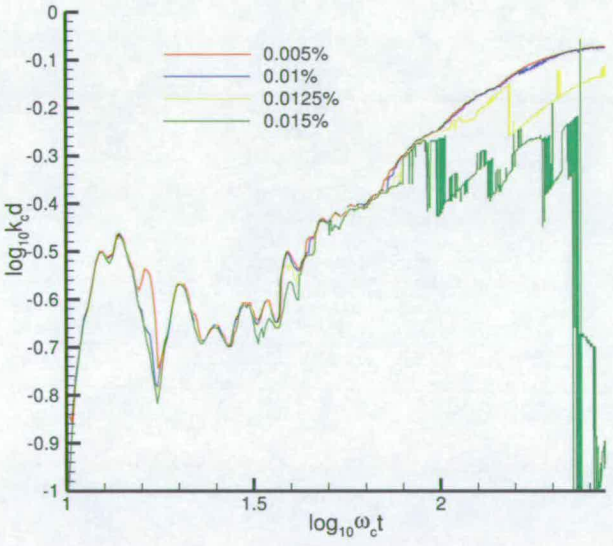

Figure 6.4: Depth against time for single ak = 0.333 breaker

Four maximum depth results are shown in figure 6.4 for concentrations of 0.005%, 0.01%, 0.0125% and 0.015%. The maximum depths reached by 0.005%

and 0.01% concentrations are very similar, showing periods of approximately linear growth between 6 and 40 seconds after breaking ($log_{10}\omega_c t$ = 1.6 to 2.35) with gradients of 5.83 $\times$ 10^{-1} and 5.84 $\times$ 10^{-1} respectively. Both lines would intercept the y-axis at -1.42. After 40 seconds the lines appear to begin to level off. This could be due to the gradual decrease in turbulent energy or the effect of the bottom of the tank. Further work in deep tanks would be required to investigate this.

Over the similar range as the lower concentrations linear growth, the maximum depth for the 0.0125% concentration also increases, with a gradient and intercept of 6.29 $\times$ 10^{-1} and 1.52 respectively. However, there is a sharp decrease in maximum depth just after $log_{10}\omega_c t$ = 2.1 followed by a gradual increase in depth again until the end of the experiment, with a gradient of 4.97 $\times$ 10^{-1}.

The maximum depth reached by the 0.015% concentration is erratic, varying between $log_{10}k_c d$ = -0.3 and -1.2.

The final maximum depths reached by the four concentrations, from largest to smallest, are $log_{10}k_c d$ = -0.94, -0.11, -0.07 and -0.07.

6.3.5 Maximum Depth Results for Single $ak = 0.339$ Breaker

The maximum depth results for two ak = 0.339 breakers are presented in figures 6.5 and 6.6 to show the difference in maximum depths reached by larger concen-

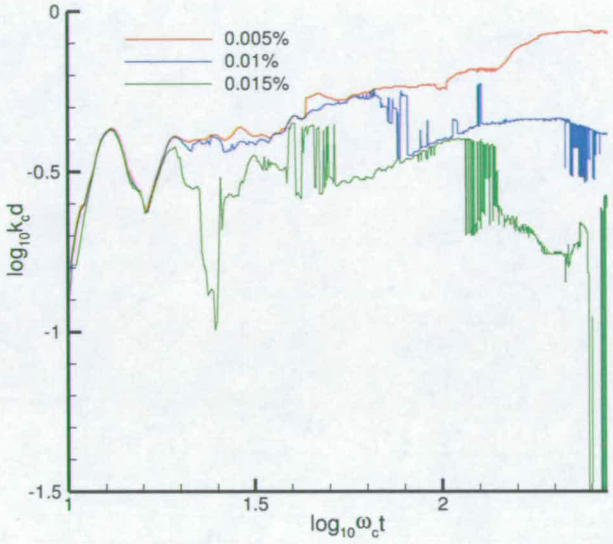

Figure 6.5: Depth against time for single ak = 0.339 breaker (first example)

trations. In both figures, the maximum depth reached for three concentrations, 0.005%, 0.01% and 0.015% is plotted.

The lines representing the smallest concentration, 0.005%, have similar final maximum depths but different shapes. In figure 6.5, the line is approximately linear between 5 and 45 seconds after breaking, with a gradient of 3.58×10^{-1} before levelling off at $log_{10}k_cd$ equals approximately -0.1. Figure 6.6 shows a shorter, sharper period of increasing maximum depth between 8 and 25 seconds, with a gradient of 6.55×10^{-1}. Following this is a short time of erratic fluctuation before reaching a final value of approximately -0.1.

The maximum depths of both 0.01% concentrations, in figures 6.5 and 6.6,

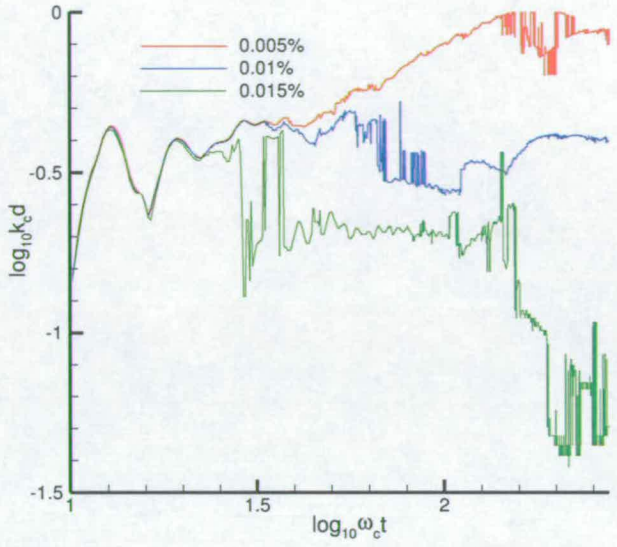

Figure 6.6: Depth against time for single ak = 0.339 breaker (second example)

again finish at similar values, but the graphs have different forms. In figure 6.5 the line follows that of the lower concentration until $log_{10}\omega_c t$ is approximately 1.6 and then the depth increases to a value similar to the 0.015% level. There is then a steady decrease in maximum depth, with a gradient of 2.18×10^{-1} before a levelling off and slight increase.

In figure 6.6, the 0.01% concentration line detaches itself from the lower concentration far earlier, and then shows a series of sharp increases and decreases in maximum depth before reaching a steady value at the end of the experiment.

In both graphs, the 0.015% concentrations shows a final decrease in maximum depth, ending very near the water's surface. In figure 6.5 there is a period of

steady decrease in maximum depth between 10 and 21 seconds after breaking with a gradient of 4.83×10^{-1} followed by periods of fluctuation and increase in maximum depth. In figure 6.6, the plot shows large areas where the maximum depth remains steady between sharp increases. These sharp increases could be caused either by dye leaving the lightsheet or small patches of high concentration dispersing into lower values.

The final maximum depths reached for the concentrations plotted in figure 6.5 are $log_{10}k_cd$ = -0.61, -0.38 and -0.07 for 0.015%, 0.01% and 0.005% respectively. The final maximum depths reached for the concentrations plotted in figure 6.6 are $log_{10}k_cd$ = -1.29, -0.40 and -0.05.

6.3.6 Maximum Depth Results for Single $ak = 0.346$ Breaker

The maximum depths reached by four concentrations, 0.003%, 0.005%, 0.01% and 0.015%, are plotted in figure 6.7 for a breaking wave with an ak value of 0.346.

The smallest concentration, 0.003% shows a linear relationship between 5 seconds and 30 seconds after breaking ($log_{10}\omega_c t$ = 1.4 to 2.2) with a gradient of 3.61×10^{-1} before levelling off at $log_{10}k_cd$ equals approximately 0.05. The plot for maximum depth of the 0.005% concentration follows a similar line to the 0.003% plot between 5 and 13 seconds, with a gradient of 5.24×10^{-1}. Following

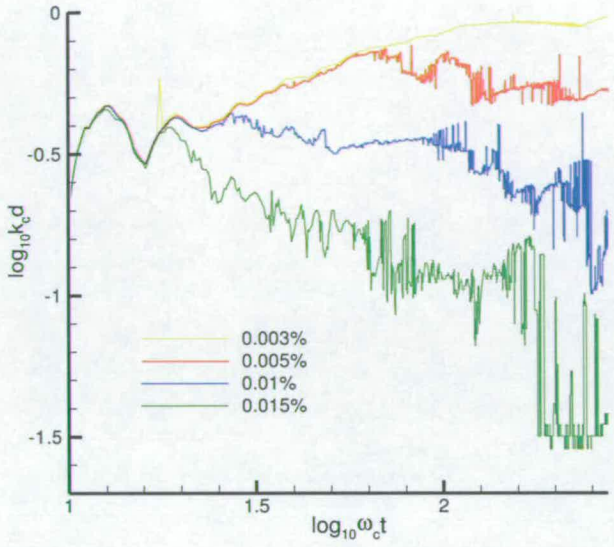

Figure 6.7: Depth against time for single ak = 0.346 breaker

this, it decreases for approximately twelve seconds before increasing again after 25 seconds, with a few steady areas.

The line representing 0.01% shows a small period of linear increase in maximum depth between 5 and 15 seconds, with a gradient of -1.37 $\times$ 10^{-1} before maintaining a steady value and then erratically decreasing in maximum depth until the end of the experiment.

It is possible to identify a trend in the decrease of maximum depth for 0.015%. Between 5 seconds and the end of the experiment this concentration shows a decrease of maximum depth with gradient of -9.17 $\times 10^{-1}$, although the graph is very unstable at points.

The final depths reached by the four concentrations, from largest to smallest, are $log_{10}k_cd$ = -1.42, -0.73, -0.28 and -0.02.

6.3.7 Maximum Depth Results for Single $ak = 0.352$ Breaker

An ak value of 0.352 was the largest used in these experiments, corresponding to a plunging breaker.

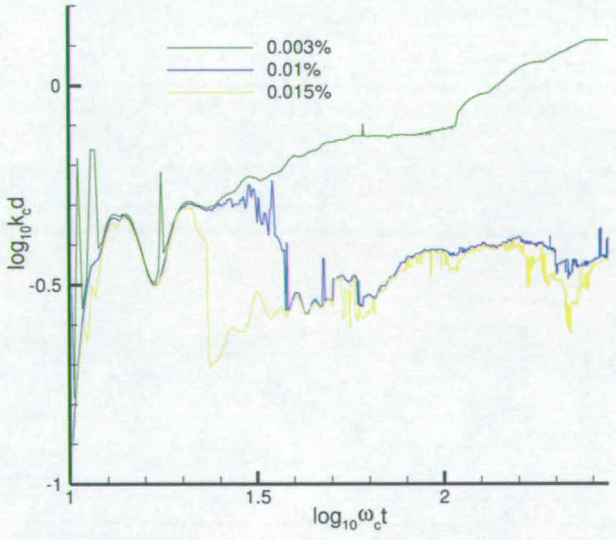

Figure 6.8: Depth against time for single ak = 0.352 breaker

The maximum depth reached by concentrations 0.003%, 0.01% and 0.015% following a breaking wave with an ak value of 0.352 are presented in figure 6.8. The 0.003% concentration shows a steady increase in maximum depth between 20 seconds after breaking and just before the end of the experiment with a gradient

of 4.35 $\times$ 10^{-1}, with a short period of steady maximum depth at the end of the experiment when fully mixed.

The plots of 0.01% and 0.015% both decrease sharply in maximum depth at $log_{10}\omega_c t$ = 1.5 and 1.3 respectively and remain approximately steady at this depth for the remainder of the experiment, with slight decreases in maximum depth between $log_{10}\omega_c t$ = 1.7 and 1.9 with gradients of 7.10 $\times$ 10^{-1} and 7.99 $\times$ 10^{-1}.

The final depths reached by the 0.015%, 0.01% and 0.003% concentrations are $log_{10}k_c d$ = -0.43, -0.38 and 0.11 respectively.

6.3.8 Maximum Depth Results Summary

As discussed previously, it is very difficult to compare the dispersion coefficients measured from the maximum depth results as they are very sensitive to slight alterations in time. Therefore, table 6.4 shows only the dispersion exponents for the measured sections on each concentration. These values are also very sensitive to the conditions under which they occur and are not necessarily comparing like with like.

It is important to look at the depths reached by the different concentrations at the end of each experiment. These are shown in table 6.5.

As the breaker size increases, the depth reached by the 0.005% concentration

increases, with the exception of the $ak = 0.346$ breaker. This suggests that larger breakers, with greater energies, will cause the lower concentrations to descend further than the smaller, less powerful breakers.

The maximum depth reached by the 0.01% concentration increases between ak values of 0.314 to 0.333 and then begins to decrease again for the large breakers. The transition from increasing to decreasing maximum depth with breaker size occurs at the point where the breakers progress from being spilling to plunging. This implies the breaker type has a significant effect, with the more energetic plunging breakers being powerful enough to disperse the 0.01% concentration into lower levels whereas the spillers are not, simply carrying it downward.

ak value	Concentration	Dispersion Exponent
0.314	0.005%	6.05×10^{-1}
0.314	0.01%	5.89×10^{-1}
0.314	0.015%	6.20×10^{-1}
0.320	0.005%	3.02×10^{-1}
0.320	0.01%	2.59×10^{-1}
0.320	0.015%	2.48×10^{-1}
0.327	0.005%	3.40×10^{-1}
0.327	0.005%	6.86×10^{-1}
0.327	0.01%	3.27×10^{-1}
0.327	0.01%	1.23
0.327	0.015%	2.20×10^{-1}
0.333	0.005%	5.83×10^{-1}
0.333	0.01%	5.84×10^{-1}
0.333	0.0125%	6.29×10^{-1}
0.333	0.0125%	4.97×10^{-1}
0.339	0.005%	3.58×10^{-1}
0.339	0.005%	6.55×10^{-1}
0.339	0.01%	2.18×10^{-1}
0.339	0.01%	8.55×10^{-1}
0.339	0.015%	4.83×10^{-1}
0.346	0.003%	3.61×10^{-1}
0.346	0.005%	5.24×10^{-1}
0.346	0.01%	-1.37×10^{-1}
0.346	0.015%	-9.17×10^{-1}
0.352	0.003%	4.35×10^{-1}
0.352	0.01%	7.10×10^{-1}
0.352	0.015%	7.99×10^{-1}

Table 6.4: Dispersion exponents from Single Breaker Depth Results

Concentration	ak value	$log_{10}k_cd$	Status
0.0005%	0.314	0.11	level
0.003%	0.346	-0.02	ascending
0.003%	0.346	0.11	steady
0.005%	0.314	-0.36	descending
0.005%	0.320	-0.33	steady/descending
0.005%	0.327	-0.19	descending
0.005%	0.333	-0.07	descending/steady
0.005%	0.339	-0.07	steady
0.005%	0.339	-0.05	steady
0.005%	0.346	-0.28	ascending
0.01%	0.314	-0.37	descending
0.01%	0.320	-0.37	ascending
0.01%	0.327	-0.22	descending
0.01%	0.333	-0.07	steady
0.01%	0.339	-0.38	ascending
0.01%	0.339	-0.40	steady
0.01%	0.346	-0.28	descending
0.01%	0.352	-0.38	steady
0.0125%	0.333	-0.11	descending
0.015%	0.314	-0.74	steady
0.015%	0.320	-0.40	ascending
0.015%	0.327	-0.72	-
0.015%	0.333	-0.94	-
0.015%	0.339	-0.61	-
0.015%	0.339	-1.29	-
0.015%	0.346	-1.42	-
0.015%	0.352	-0.43	-

Table 6.5: Maximum depth values for single breaker results

The trend of larger breakers actually causing a shallower maximum depth to be reached is continued by the 0.015% concentration, where larger breaking waves produce the smallest maximum depths; the majority of the large concentrations are mixed into lower concentrations, causing a significant reduction in the depth they reach.

This is significant as it implies that small spilling breakers will result in a greater penetration of higher concentrations than larger plunging breakers. Therefore the dispersion of a surface pollutant caused by isolated spilling breakers may pose a larger threat to organisms living near the water's surface than that caused by plunging breakers.

6.4 Area Results for Single Breaker

The area covered by the dispersing surface film is of obvious importance. As with the previous section, a sample plot is presented for each breaker amplitude used. As the concentration lines spread more evenly, it is possible to plot the full range of concentrations used for most experiments.

Time is non-dimensionalised in the same manner as the depth results, and area is non-dimensionalised by multiplying by the central wavenumber k_c, squared. As with the depth results, log-log graphs are used.

Gradients and dispersion coefficients are calculated for certain lines from each plot and a final table of area results is presented at the end of section. Primarily the concentrations of 0.004% and 0.015% are examined as these provided the clearest results; 0.004% was the lowest value that is always higher than the background level and 0.015% was the highest concentration measured.

6.4.1 Area Results for Single $ak = 0.314$ Breaker

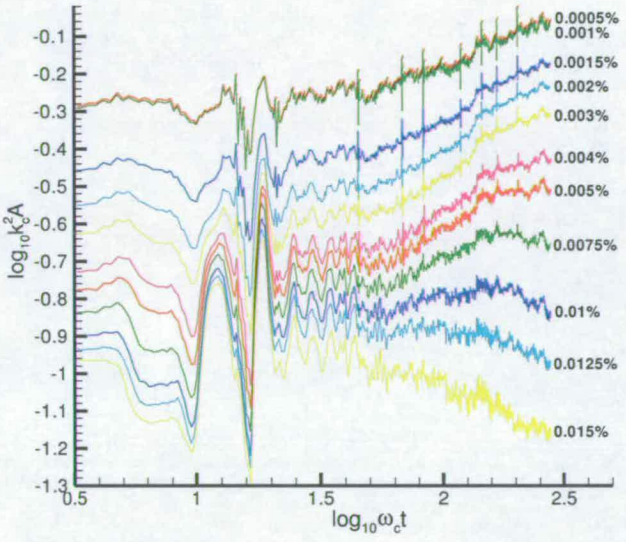

Figure 6.9: Area against time for single ak = 0.314 breaker

Figure 6.9 is a plot of non-dimensional area against non-dimensional time. Each line represents the number of pixels with a grey level corresponding to that concentration or higher, as measured from the calibration images. The large initial values of 0.0005% and 0.001% concentrations are due to the background dye.

Sharp peaks and troughs can be seen around $log_{10}\omega_c t = 1$, caused by the motion of the water's surface during breaking. The smaller concentrations, 0.0015% to 0.004%, continue to grow following breaking whereas the higher levels begin to decrease following an initial expansion as they feed the expansion of lower

concentrations.

The area of the 0.005% concentration remains almost constant in area, balanced between expanding and being fuelled by the higher concentrations. As this concentration appears to maintain a constant area it will be referred to as *Concentration of Constant Area, CCA*. The CCA for an $ak = 0.314$ breaker is therefore estimated to 0.005%. This value is significant because it represents the highest concentration that is not decreasing in area over the period of the experiment and therefore the highest concentration of pollutant to which the environment will be subjected to for a given time.

The larger concentrations show a steady decrease in area following breaking. This corresponds to the initial mixing following breaking dispersing the greater concentrations.

The area of concentrations 0.0005% to 0.004% show a steady increase between $\log\omega t = 1.6$ and the end of the experiment, with a gradient and intercept of 3.62×10^{-1} and -1.04 respectively, representing a dispersion coefficient of 6.64×10^{-4}. The relationship between patch size and time is therefore

$$k_c^2 A = (2 \times 6.64 \times 10^{-4} \times \omega_c t)^{0.362} \tag{6.3}$$

Between $log_{10}\omega_c t = 1.7$ and 2.25, the line for 0.0075% is very similar to the lines described in equation 6.3, with a gradient and intercept of 3.12×10^{-1} and

-1.32. However, after $log_{10}\omega_c t = 2.25$ (32 seconds after breaking), the area levels off, decreasing slightly.

From $log_{10}\omega_c t = 1.6$ onward the 0.015% concentration shows a steady decline in area, with a gradient of -2.66×10^{-1}.

The results for the final area covered for each concentration for each breaking wave amplitude can be found in Appendix B.

6.4.2 Area Results for Single $ak = 0.320$ Breaker

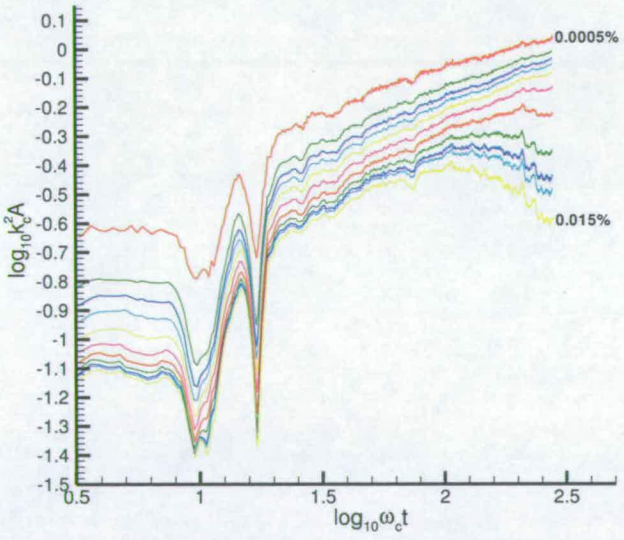

Figure 6.10: Area against time for single ak = 0.320 breaker

Figure 6.10 shows the evolution of dye area over time following an $ak = 0.320$

breaker. Unlike figure 6.9 where background dye from previous experiments gave an initial high value of the lowest concentrations, this graph clearly shows the sharp increase in all areas covered as the dye is mixed beneath the surface. The top right portion of the graph is shown expanded in figure 6.11. In this graph it is easier to make out the individual concentrations.

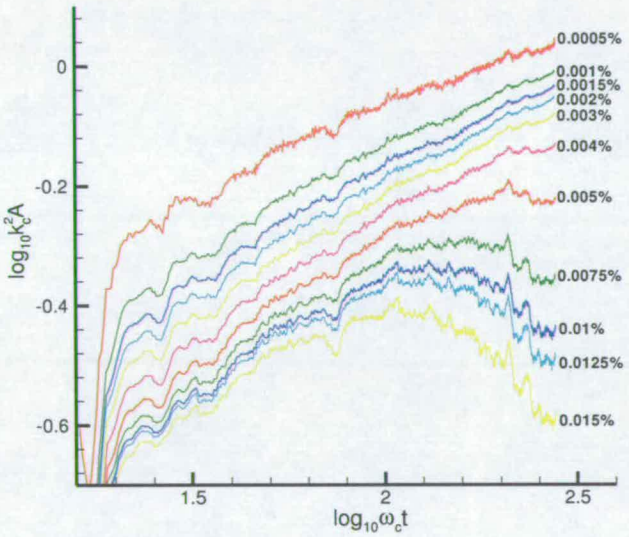

Figure 6.11: Area against time for single ak = 0.320 breaker (large)

From approximately 4 seconds after breaking ($log_{10}\omega_c t = 1.35$) until the end of the experiment, the plots of 0.0005% to 0.004% show steady growth. 0.003% has a gradient and intercept of 3.63×10^{-1} and -9.53×10^{-1}, giving a dispersion coefficient of 1.20×10^{-3}.

The 0.015% concentration shows similar growth between 4 seconds and ap-

proximately 20 seconds ($log_{10}\omega_c t = 2.05$) with a gradient of 3.41×10^{-1}. However, between this point and the end of the experiment, the area decreases with a gradient of -5.31×10^{-1}.

The CCA appears to be around 0.005% again.

6.4.3 Area Results for Single $ak = 0.327$ Breaker

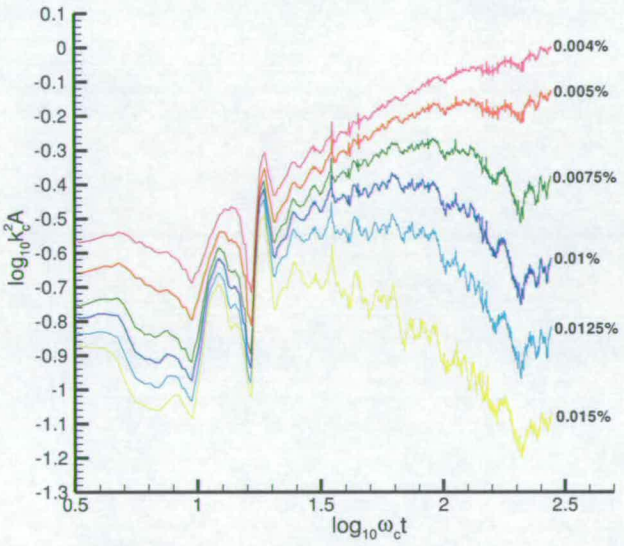

Figure 6.12: Area against time for single ak = 0.327 breaker

In the graph of area against time for an ak = 0.327 breaker, shown in figure 6.12, the lower concentrations have been removed as they were swamped by background. The plot for 0.004% has a gradient and intercept of 2.81×10^{-1} and -6.77×10^{-1}. The dispersion coefficient is then calculated to be 1.9×10^{-3}.

Although the concentrations follow the paths similar to other experiments, there is a sharp change at $log_{10}\omega_c t = 2.3$. This corresponds to a patch of dye entering the lightsheet, causing a rise in the areas of most concentrations.

Between $log_{10}\omega_c t = 1.45$ and this point, the line of 0.015% concentration shows a steady decrease with a gradient of -5.63×10^{-1}.

The CCA is now slightly less than 0.005%.

6.4.4 Area Results for Single $ak = 0.333$ Breaker

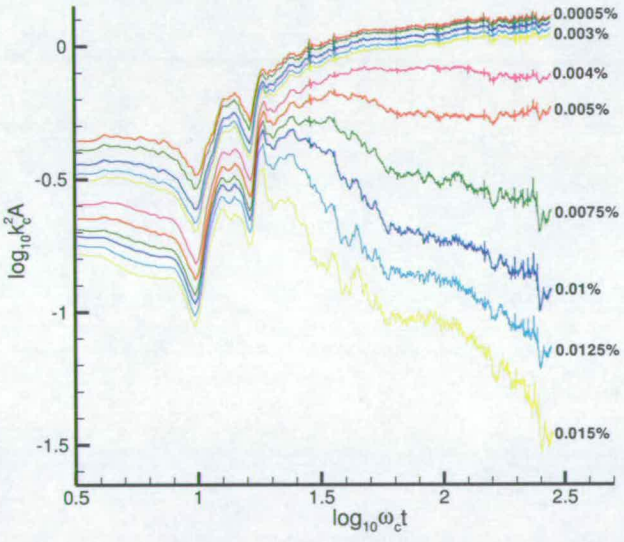

Figure 6.13: Area against time for single ak = 0.333 breaker

The lines representing the concentrations 0.0005% to 0.003% in figure 6.13

are very close together and show very slow growth in area. This can be explained by how quickly the concentrations reach large values. These concentrations have reached a value of $log_{10}k_c^2A = 0$ within a far shorter space of time than the similar concentrations in figure 6.12.

The lines for 0.004% and 0.005% are very nearly level, with gradients of -6.43×10^{-2} and -2.85×10^{-2} respectively. The *CCA* therefore lies somewhere between the two.

As with the previous experiments, the area covered by the 0.015% concentration falls rapidly after breaking. Between $log_{10}\omega_c t = 1.4$ and the end of the experiment the line has a gradient of -7.06×10^{-1}.

6.4.5 Area Results for Single $ak = 0.339$ Breaker

The concentration values between 0.0005% and 0.004% show a gradual increase in area for the $ak = 0.339$ breaker, shown in figure 6.14. The line representing 0.004% has a gradient of 2.88×10^{-1} and intercept of -5.92×10^{-1}, giving a dispersion coefficient of 4.4×10^{-3}.

The line for 0.005%, although rising in area between $log_{10}\omega_c t = 1.3$ and 2, begins to decline after $log_{10}\omega_c t$ reaches 2. This implies the line of *CCA* is somewhere between 0.004% and 0.005%, potentially nearer 0.004%.

The 0.015% value show a decrease between $log_{10}\omega_c t = 1.8$ and the end of the

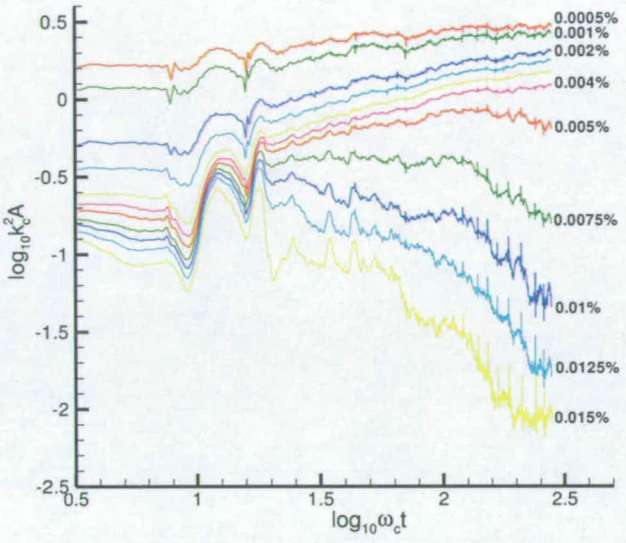

Figure 6.14: Area against time for single ak = 0.339 breaker

experiment with a gradient of -1.50.

6.4.6 Area Results for Single $ak = 0.346$ Breaker

The top two lines in figure 6.15, showing the dispersion areas under an $ak = 0.346$ breaking wave, can be disregarded as they correspond to a concentration level lower than the background. However, the concentration values 0.0015%, 0.002% (not labeled due to lack of space) and 0.003% show a steady increase in area, similar to those shown in figures 6.9 to 6.14. The gradient and intercept of the line representing the 0.003% concentration are 2.70×10^{-1} and -4.02×10^{-1} respectively. The dispersion coefficient is 1.6×10^{-2}.

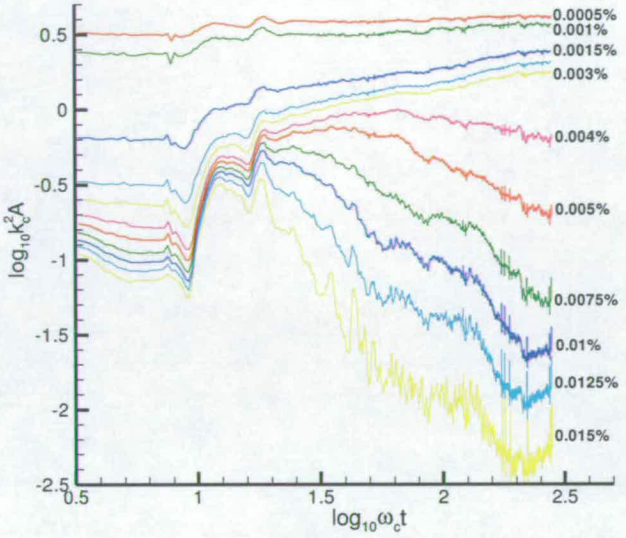

Figure 6.15: Area against time for single ak = 0.346 breaker

The *CCA* level appears to be between 0.003% and 0.004%, with the 0.004% line having a gradient of -1.68×10^{-2} between $log_{10}\omega_c t = 1.7$ and the end of the experiment.

As with figure 6.12, there is a slight increase in area at the end of the experiment, corresponding to a patch of dye entering the lightsheet. Prior to this point, the 0.015% line had a gradient of -1.36.

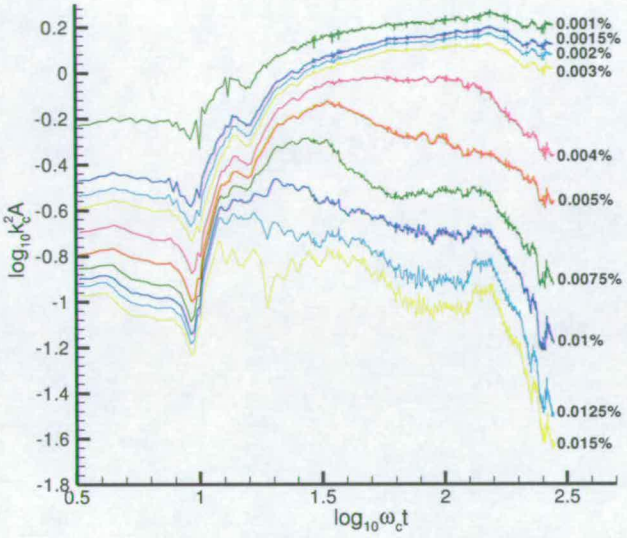

Figure 6.16: Area against time for single ak = 0.352 breaker

6.4.7 Area Results for Single $ak = 0.352$ Breaker

The final breaker is an $ak = 0.352$ plunging breaker. This is the largest breaker it was possible to use without significant amounts of dye leaving the upstream view of the cameras.

As can be seen in figure 6.16, the lines for concentrations below 0.004% show a rapid increase and then a general levelling off, covering an area of approximately $log_{10}k_c^2A = 0$ to 0.2. The areas of 0.004% and greater are steady until a sudden drop around a time of $log_{10}\omega_c t = 2.1$. This corresponds to dye leaving the far end of the vision of the cameras, and therefore is not a genuine drop in area covered by the film.

The *CCA* value in this plot lies between 0.003% and 0.004%.

6.4.8 Area Results Summary

The previous sections have discussed the gradients of the concentrations in the plot of area against time. A summary of these results are presented in table 6.6 below.

Concentration	ak value	Dispersion Exponent(Gradient)
0.003%	0.320	3.63×10^{-1}
0.003%	0.346	2.70×10^{-1}
0.004%	0.314	3.62×10^{-1}
0.004%	0.327	2.81×10^{-1}
0.004%	0.333	-6.43×10^{-2}
0.004%	0.339	2.88×10^{-1}
0.004%	0.346	-1.68×10^{-2}
0.005%	0.333	-2.85×10^{-2}
0.015%	0.314	-2.66×10^{-1}
0.015%	0.320	3.41×10^{-1}
0.015%	0.320	-5.31×10^{-1}
0.015%	0.327	-5.63×10^{-1}
0.015%	0.333	-7.06×10^{-1}
0.015%	0.339	-1.50×10^{-1}
0.015%	0.346	-1.36

Table 6.6: Dispersion exponents for single breaker area results

There doesn't appear to be a direct link between breaker size and dispersion exponent, although since exponents are calculated at different times during the experiment they provide only a limited snapshot.

However, there is a clear overall increase in spread between the concentra-

tion area lines as the size of the wave increases. Tables of $log_{10}k_c^2A$ for each concentration and breaking wave amplitude can be seen in appendix B.

The CCA value shows a steady decrease with increasing wave amplitude. This implies that larger waves will result in smaller concentrations of dye remaining constant in area and will therefore be more beneficial to the dispersion of a surface pollutant.

The graphs shown in figure 6.17 show the areas covered by the concentrations 0.0005%, 0.001%, 0.0015% and 0.002% as breaker size increases. Experiments where the background dye may have affected these results were discarded.

For the smallest measured concentration, 0.0005%, there is a clear linear relationship between area and ak value of the breaking wave between 0.320 and 0.352. This is given by:

$$log_{10}k_c^2A = 4.91ak - 1.53 \tag{6.4}$$

The final point on this line represents an area equal to the full image (1528 x 484), and is therefore impossible to go beyond in this experiment.

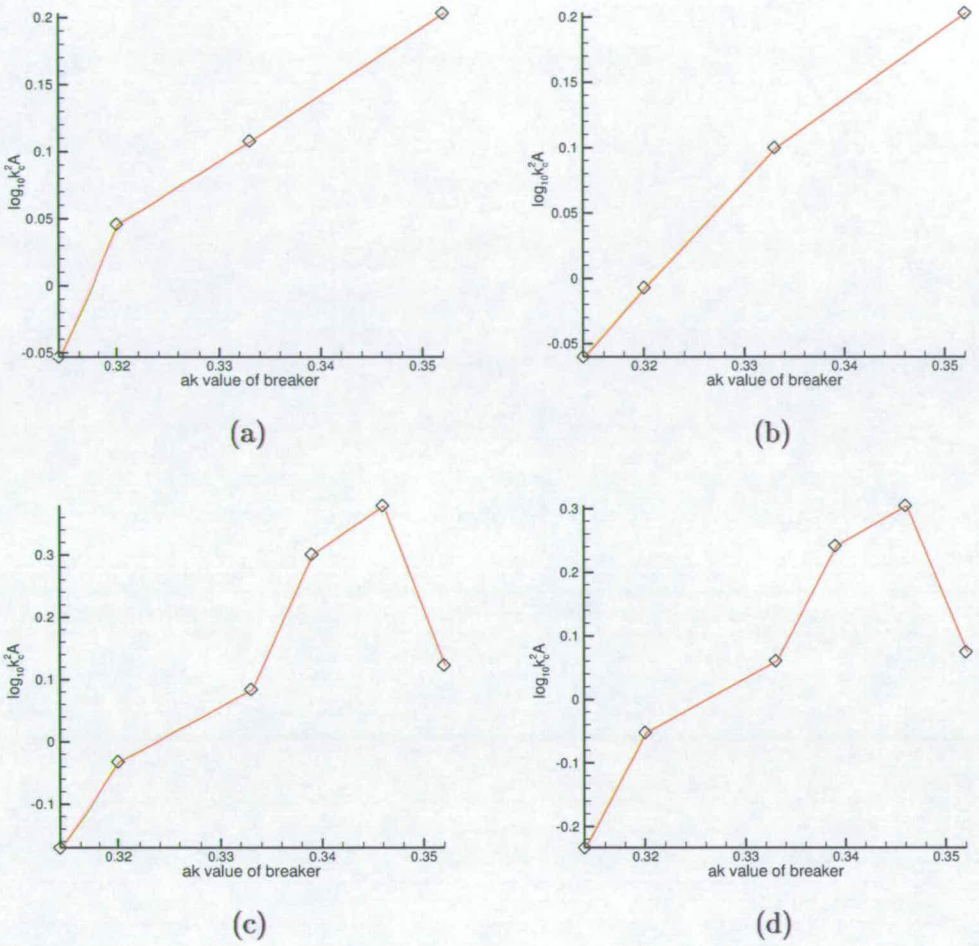

Figure 6.17: Area against breaker size for (a)0.0005%, (b)0.001%, (c)0.0015% and (d)0.002%

The next graph, (b), has the equation:

$$log_{10}k_c^2A = 8.39ak - 2.69 \tag{6.5}$$

Graph (c) in figure 6.17 shows the area covered by the 0.0015% concentration

for increasing breaking wave size. There is a linear region between 0.314 and 0.346, with a slight dip at 0.333. This linear region is described by:

$$log_{10}k_c^2A = 1.69 \times 10^1 ak - 5.47 \tag{6.6}$$

The area value for the largest breaker is lower than the previous wave results. This could be due to the random nature of the experiment, but results for higher concentrations suggest this is the beginning of a different trend exhibited with the larger breakers. This will be discussed further when examining the higher concentrations.

The final graph in figure 6.17 is very similar to the previous result. This graph presents the area of the 0.002% concentration for increasing breaker size. Over the same region as described for the previous graph, the relationship is given by:

$$log_{10}k_c^2A = 1.62 \times 10^1 ak - 5.29 \tag{6.7}$$

This similarity is continued onto the results for 0.003% concentration, shown in the top left of figure 6.18 where the gradient of the line is 1.77×10^1 with an intercept of -4.14.

The graphs become qualitatively different for concentrations greater than 0.003%. The graph of area against breaker size for 0.004% concentration, shown

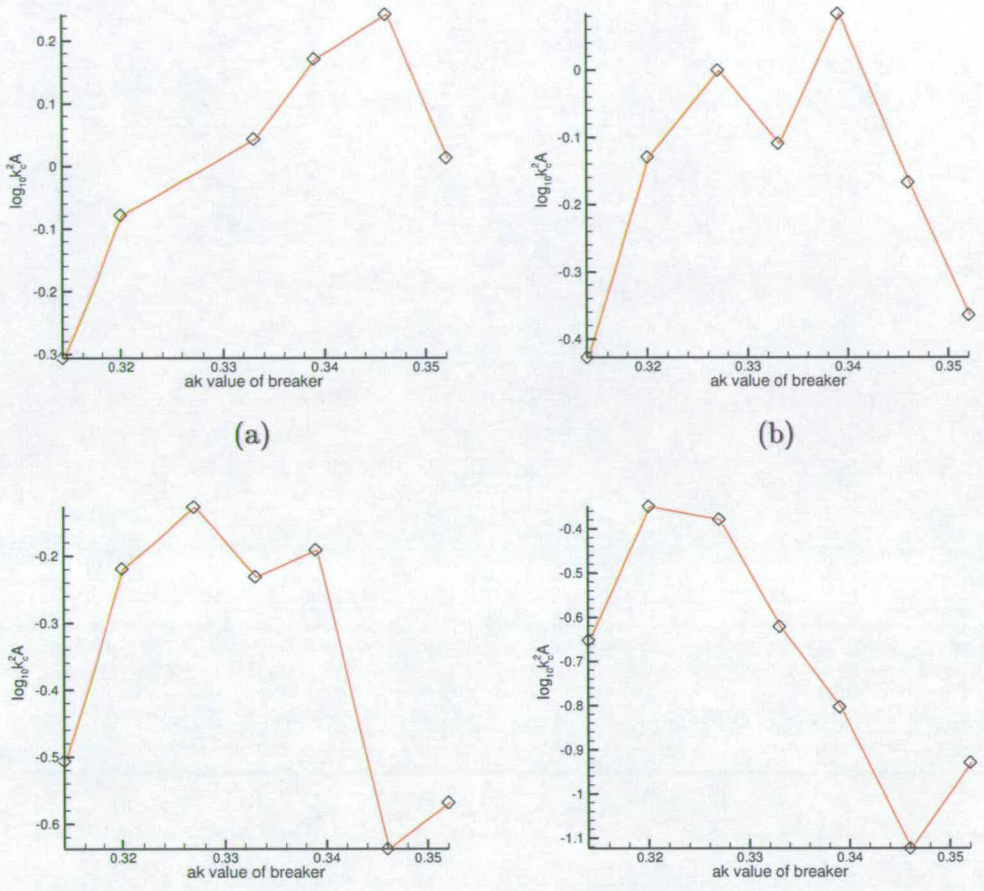

Figure 6.18: Area against breaker size for (a)0.003%, (b)0.004%, (c)0.005% and (d)0.0075%

in the top right of figure 6.18, has a definite peak for a breaker with an ak value of 0.339. The slight dip for the previous wave size, also exhibited by the lower concentrations and the 0.005% results appears to be an exception to the expected result caused by the random nature of the experiment.

This maximum at 0.339, corresponding to the transition from spilling to plunging breaking, is followed by a rapid decrease in area. As with the depth results

discussed in section 6.3.8, there is a notable change in the character of the mixing when the breaking process changes from spilling to plunging.

The relationship between area and breaking wave size following the peak is given by:

$$log_{10}k_c^2A = -3.45 \times 10^1 ak + 1.18 \times 10^1 \tag{6.8}$$

Graph 6.18(c), representing 0.005%, is qualitatively very similar to the previous result, again with the slight dip for the $ak = 0.333$ breaker. Comparing all four graphs in figure 6.18 it appears there is a similar structure, with the peak of area moving gradually to the left with increasing concentration. This suggests that certain breaking wave sizes will result in maximum areas for certain concentrations, allowing predictions of which concentrations may cause the greatest problems given a sea condition containing known breaker sizes.

Between ak values of 0.327 and 0.346, the relationship between area and breaker size for the 0.0075% concentration is:

$$log_{10}k_c^2A = -3.85 \times 10^1 ak + 1.22 \times 10^1 \tag{6.9}$$

Both the graphs for 0.005% and 0.0075% show an increase in area again for the largest breaker. This could be due to the specific experiment and not the

increase in amplitude, but the effect is exhibited for both 0.346 and 0.352 for the largest measured concentration. This suggests another change in behaviour, with further translation of the graphs as the concentration increases.

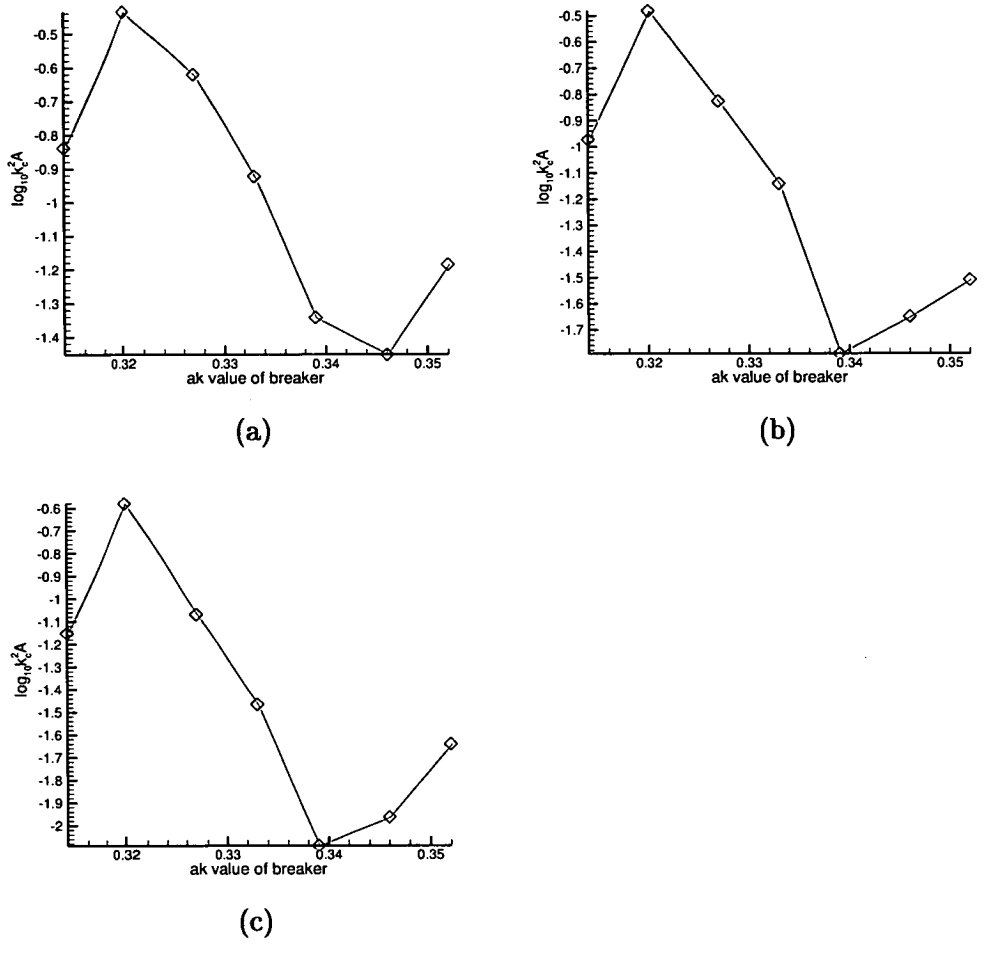

Figure 6.19: Area against breaker size for (a)0.01%, (b)0.0125% and (c)0.015%

Figure 6.19 is the final set of graphs showing area against breaker amplitude. The top left graph shows the 0.01% concentration. The structure of the graph is very similar to 0.0075% graph, with the peak of area moved slightly to the left.

Between ak values of 0.320 and 0.339, the plot has a gradient of -4.77 $\times$ 10^1 with an intercept of -1.49 $\times$ 10^1.

The next largest concentration, 0.0125%, is also very similar to 0.01%. However, there is a clear increase in area after 0.339. For these concentrations the transition from spilling to plunging is creating greater areas again. The larger spilling breakers serve to disperse the higher concentrations more, reducing their area. However, the plunging breakers create larger areas of the higher concentrations again, relative to their sizes for the largest spillers.

The reduction in area before the transition to plunging breaking is given by:

$$log_{10}k_c^2A = -6.70 \times 10^1 + 2.10 \times 10^1 \tag{6.10}$$

and following the transition, the relationship is:

$$log_{10}k_c^2A = 2.17 \times 10^1 - 9.16 \tag{6.11}$$

The final graph shows the area covered by the 0.015% concentration. The two regions of the graph before and after the transition to plunging breakers are given by equations 6.12 and 6.13:

$$log_{10}k_c^2A = -7.79 \times 10^1 + 2.44 \times 10^1 \quad (6.12)$$

$$log_{10}k_c^2A = 3.40 \times 10^1 - 1.37 \times 10^1 \quad (6.13)$$

The graphs presented in figures 6.17 to 6.19 represent only the final areas covered by the dispersing dye.

6.4.9 2D Mass

Before looking at the centre of mass motion, it is important to consider the effect of dye entering and leaving the lightsheet. During the analysis process the 0^{th} moment of the dye, as defined in section 5.4, was calculated. This 0^{th} moment is effectively the 2D mass of the film, the sum of the concentration value of each pixel, and therefore gives an indication of the amount of dye entering and leaving the lightsheet.

A plot of this 2D mass against time for an $ak = 0.327$ breaker is shown in figure 6.20 below.

The initial peaks and troughs are caused by the moving surface but the mass settles down to an almost constant value between $log_{10}\omega_c t = 1.5$ and the end of the experiment. There are slight variations as any dye with a concentration

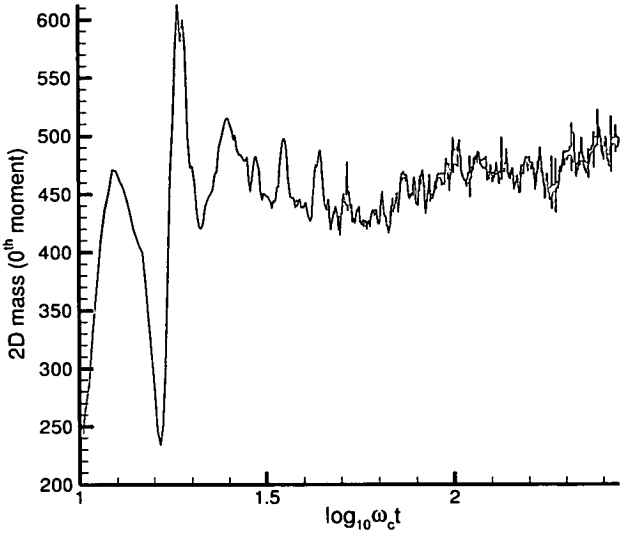

Figure 6.20: 2D mass against time for single ak = 0.327 breaker

greater than 0.02% is just counted as 0.02% concentration, and any dye with a concentration of less than 0.0005% is not counted at all. Also, the motion of dye in and out of the lightsheet causes variations in the 2D mass. This can be seen more clearly on the plot for an $ak = 0.346$ breaker shown in figure 6.21, where there is a steady rise in the mass due to extra dye entering the lightsheet.

As previously mentioned, the $ak = 0.352$ breaker caused dye to leave the upstream end of the vision of the cameras. This can be seen in the mass plot for this breaker in figure 6.22.

The mass remains largely constant until approximately $log_{10}\omega_c t = 2.2$ and then as the dye leaves the mass falls until the end of the experiment. This is one

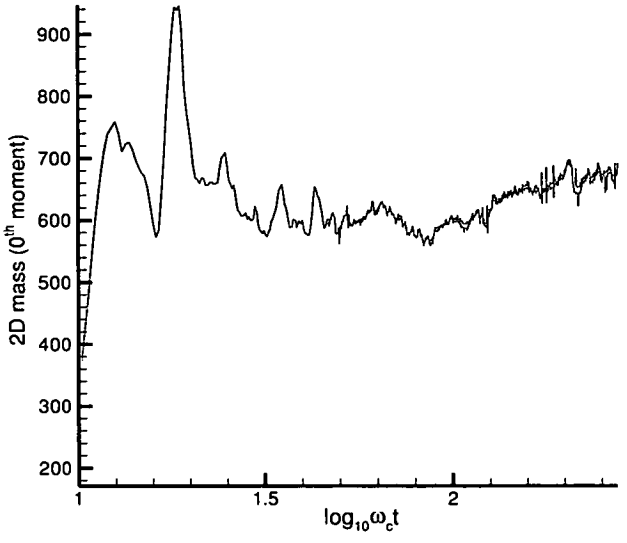

Figure 6.21: 2D mass against time for single ak = 0.346 breaker

of the limiting factors in the size of wave that could be used for these experiments. Also, for the second breaker experiments, when the time scale from initial breaker was much larger and a further breaking wave caused more dispersion, the size of wave was limited further, as will be discussed in chapter 7.

This effect could be removed by scaling the area results with respect to the 2D mass of the film. However, this system would be very sensitive to dye entering and leaving the lightsheet and would not reflect the true area covered by the dispersing film.

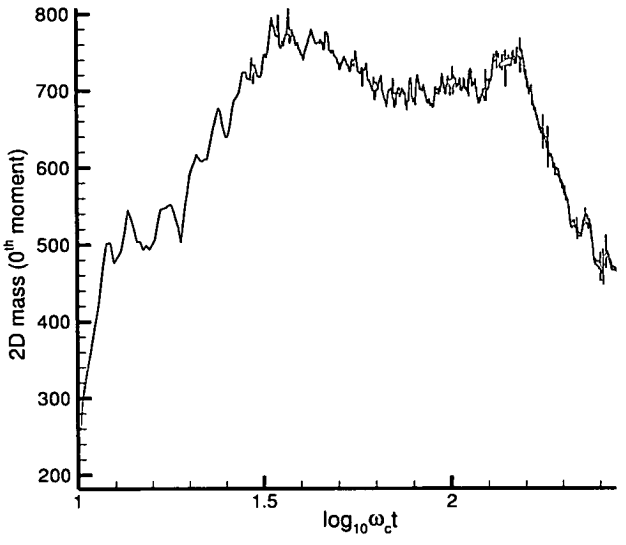

Figure 6.22: 2D mass against time for single ak = 0.352 breaker

6.5 Centre of Mass Results for Single Breaker

The centre of mass, c.o.m., was also measured during these experiments. By tracking the position of the c.o.m. it was possible to calculate the position of the dye as a whole as it was dispersed by the breaking wave. Combining this result with the values for depth and area gives a clear picture of how and where the dye dispersed.

The centre of mass was measured as separate x and y coordinates, corresponding to the directions perpendicular and parallel to the wave direction respectively, as shown in figure 6.23. The results are plotted, non-dimensionalised by multi-

plication with k_c, against non-dimensional time. The lines are plotted relative to the MWL at the centre of the image. The y coordinate is represented by a red line, with positive values corresponding to motion in the wave direction and negative values motion opposite to the wave direction. The x, or depth, coordinate is represented by a green line, with negative values corresponding to increasing distance from the MWL.

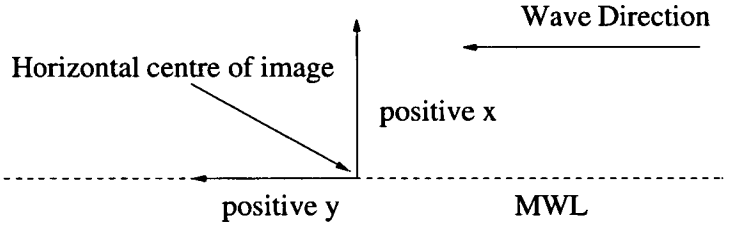

Figure 6.23: Coordinate system for recorded images

The depth is non-dimensionalised with respect to k_c rather than wave amplitude to allow easy comparison with the depth results presented in section 6.3.8. Logarithms are not used for the c.o.m. position in order to keep the distinction between x and y components as clear as possible. However, time is plotted logarithmically to allow comparison with depth and area results and to show the decrease in centre of mass motion with increasing time following breaking. The relationship between $k_c d$ and $log_{10}\omega_c t$ is often presented as a straight line with a gradient calculated using Tecplot 9 once again. Although this would predict the infinite motion downstream after infinite time, it shows that in time scales of the order of seconds and minutes there is a logarithmic relationship.

6.5.1 Centre of Mass Results for Single $ak = 0.314$ Breaker

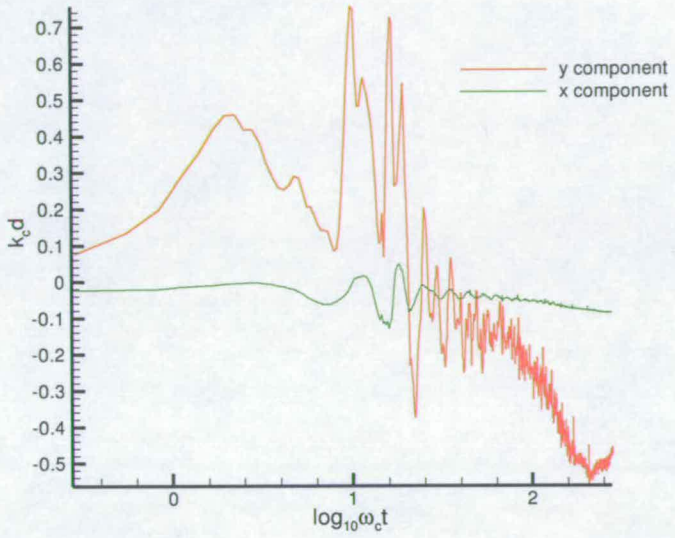

Figure 6.24: Centre of mass against time for single ak = 0.314 breaker

The first graph, figure 6.24, shows the motion of the centre of mass after the film has been dispersed by a breaking wave with a non-dimensional amplitude of 0.314. Both lines start near a $k_c d$ value around zero. This is because each value has been plotted as its variation from the perfect centre of mass position before breaking, corresponding to a film spread exactly evenly on the MWL. Slight variations cause the initial c.o.m. value to vary marginally from this however.

The process of breaking itself at $log_{10}\omega_c t = 1$ causes sharp peaks and troughs in the c.o.m. values before the surface motion dies down. The c.o.m. then appears to move upstream, against the wave motion, for approximately 25 seconds, reaching

a distance of approximately a tenth of a wavelength. Following this, the c.o.m. of the dye patch travels downstream a short distance.

The motion of the c.o.m. against the wave direction is due to the position of the breaking wave in the recordings. Before the film is disturbed the centre of mass is exactly in the middle of the image. However, the actual breaking point of the wave is slightly to the upstream direction of the centre of the image, and when the dispersion occurs following a breaking wave it is on the righthand side of the recording only. Therefore, the c.o.m. appears to move upstream, against the wave direction.

The depth of the c.o.m. steadily decreases between $log_{10}\omega_c t = 1.5$ and the end of the experiment with a relationship of

$$k_c d = -6.82 \times 10^{-2} log_{10}\omega_c t + 7.82 \times 10^{-2} \tag{6.14}$$

with a final depth of $k_c d$ = -0.086.

6.5.2 Centre of Mass Results for Single $ak = 0.320$ Breaker

The most obvious feature of the graph of c.o.m. position for an ak = 0.320 breaker, seen in figure 6.25 is the low initial value of the y component, approximately one wavelength upstream of the centre of the images.

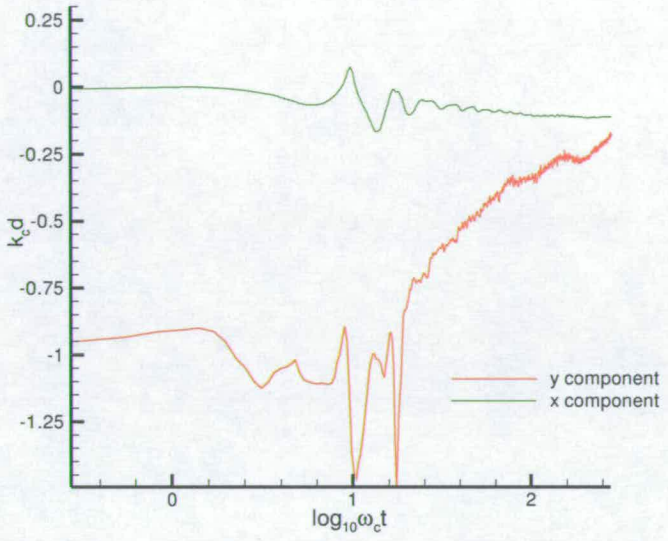

Figure 6.25: Centre of mass against time for single ak = 0.320 breaker

This could be caused by small areas of high concentration below the surface moving the c.o.m. position. However, this has the largest effect on the intercept of the graph and not the gradient connecting the c.o.m. to the time following breaking. Also, as this small area of high concentration is dispersed following breaking, its effect is minimised, and in effect reduces the final c.o.m. position by much less than 1 $k_c d$.

Between 4 and 14 seconds after breaking, ($log_{10}\omega_c t$ = 1.2 to 1.8) the c.o.m. moves almost 0.1 of a wavelength downstream, with a gradient of 6.88×10^{-1}. Similar short areas of motion can be seen around $log_{10}\omega_c t$ = 2 and 2.1, with gradients of 4.61×10^{-1} and 5.92×10^{-1} respectively.

Between 5 seconds and the end of the experiment the depth coordinate shows a steady decrease with the relationship

$$k_c d = -4.37 \times 10^{-2} log\omega_c t - 1.23 \times 10^{-2} \tag{6.15}$$

although the decrease has largely levelled off by the end of experiment at a depth of $k_c d = -0.11$, approximately $\frac{1}{50}$ of a wavelength.

6.5.3 Centre of Mass Results for Single $ak = 0.327$ Breaker

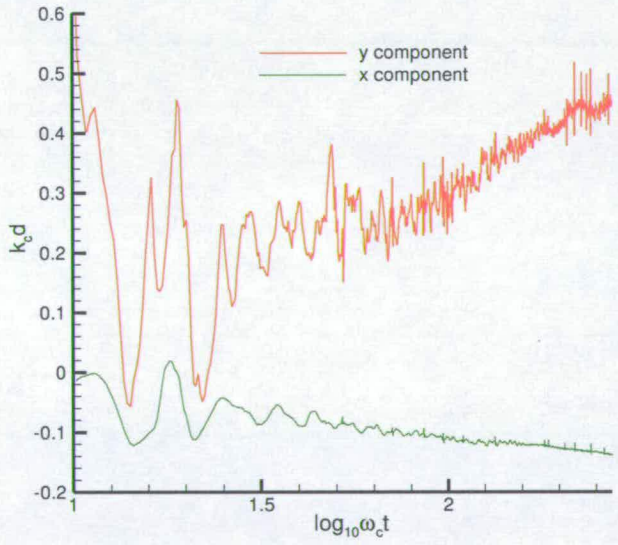

Figure 6.26: Centre of mass against time for single ak = 0.327 breaker

The time axis of the graph in figure 6.26 has been shortened to start at $log_{10}\omega_c t$

= 1 to enable a clearer inspection of the motion following breaking.

The y component shows an increase in the downstream direction between 12 and 40 seconds after breaking, with a gradient of 3.93×10^{-1} before levelling off at the end of the experiment with a final value of approximately $k_c d = 0.45$, corresponding to 0.07 wavelengths downstream.

As with the graphs in figures 6.24 and 6.25, the depth of the c.o.m. decreases as time increases. The gradient between $log_{10}\omega_c t = 1.6$ and the end of the experiment is -6.53×10^{-2} with a final $k_c d$ value of -0.138.

6.5.4 Centre of Mass Results for Single $ak = 0.333$ Breaker

Figure 6.27 shows the centre of mass motion for a breaking wave with an ak value of 0.333. The red line, representing downstream direction, shows two linear areas; between $log_{10}\omega_c t = 1.6$ and 2, and 2.1 and the end of the experiment, with a slightly flatter region between. The gradients of these two sections are 6.29×10^{-1} and 8.45×10^{-1} respectively. The final displacement of the c.o.m. is approximately $k_c d = 0.772$, 0.12 wavelengths downstream.

The depth component decreases between $log_{10}\omega_c t = 1.6$ and the end of the experiment with a gradient of 6.90×10^{-1}, reaching a final depth of $k_c d$ = -0.197.

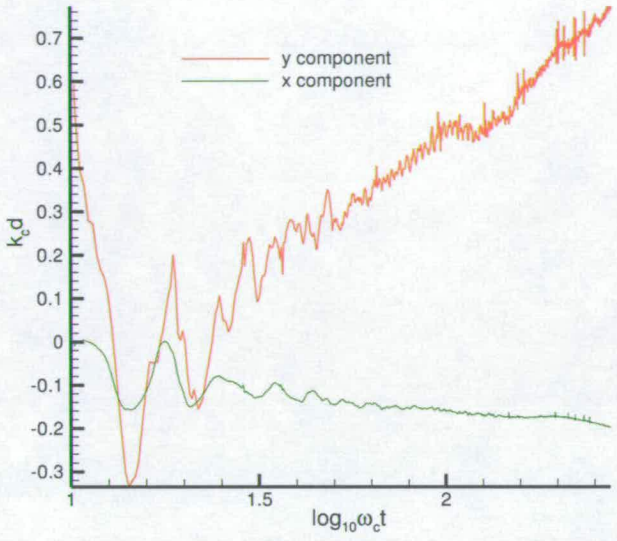

Figure 6.27: Centre of mass against time for single ak = 0.333 breaker

6.5.5 Centre of Mass Results for Single $ak = 0.339$ Breaker

The graph of c.o.m. motion for an $ak = 0.339$ breaker, shown in figure 6.28, shows an example of a qualitatively different downstream motion. A very sharp rise in the $k_c d$ value between $log_{10}\omega_c t = 1.3$ and 1.8 is followed be a far slower increase afterwards, with a gradient of 3.02×10^{-1}. However, the final value of $k_c d = 0.865$ is consistent with the general trend of increasing downstream motion with increasing amplitude, shown in figure 6.31 in section 6.5.8.

The depth of the centre of mass decreases in a similar manner to the smaller amplitudes with a gradient of -1.72×10^{-1}, reaching a final value of $k_c d$ = -0.259.

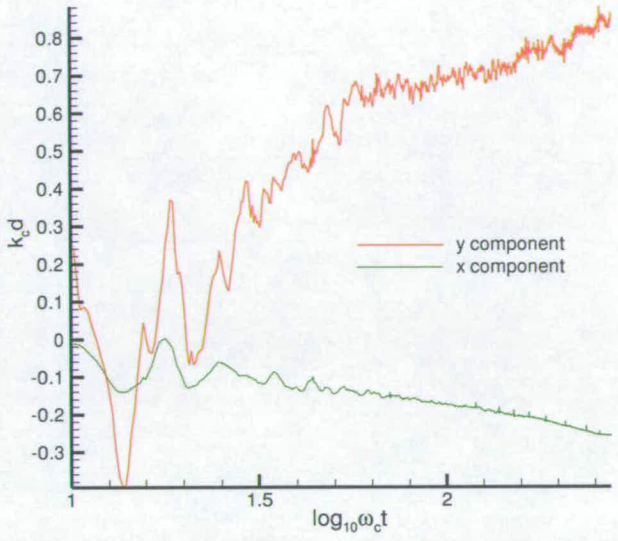

Figure 6.28: Centre of mass against time for single ak = 0.339 breaker

6.5.6 Centre of Mass Results for Single $ak = 0.346$ Breaker

In the case of the $ak = 0.346$ breaker, the c.o.m. increases in depth and moves downstream steadily from approximately 14 seconds after breaking until the end of the experiment, as shown in figure 6.29. The downstream motion gradient is 7.09×10^{-1} with the depth increasing with a gradient of -1.41×10^{-1}. The final $k_c d$ values of downstream motion and depth are 1.069 and -0.246 respectively.

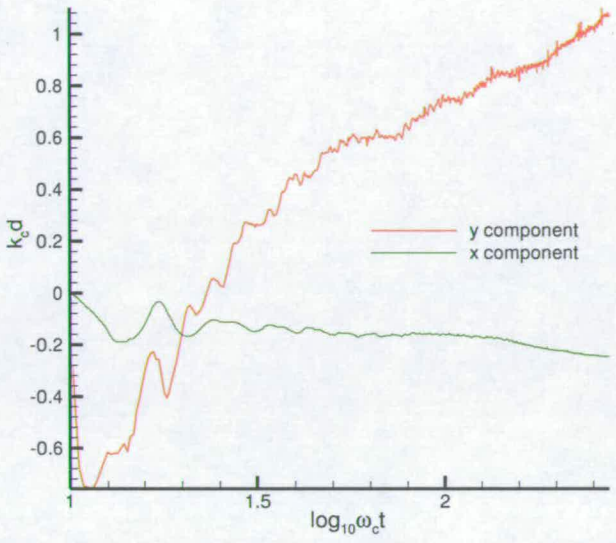

Figure 6.29: Centre of mass against time for single ak = 0.346 breaker

6.5.7 Centre of Mass Results for Single $ak = 0.352$ Breaker

The results for the centre of mass motion for the final and largest breaking wave are presented in figure 6.30.

Two regions can be seen in downstream motion, the first a steady increase between $log_{10}\omega_c t = 1.6$ and 2.1, the second between 2.1 and the end of the experiment. The first section has a gradient of 1.42, the second 3.19×10^{-1}. Combined with the result for an ak = 0.339 breaker shown in figure 6.28, this suggests that once a certain value downstream has been reached there is a resistance to continued motion at this speed and the velocity is reduced. The final c.o.m. position is at a $k_c d$ value of 1.212, approximately $\frac{1}{5}$ of a wavelength downstream.

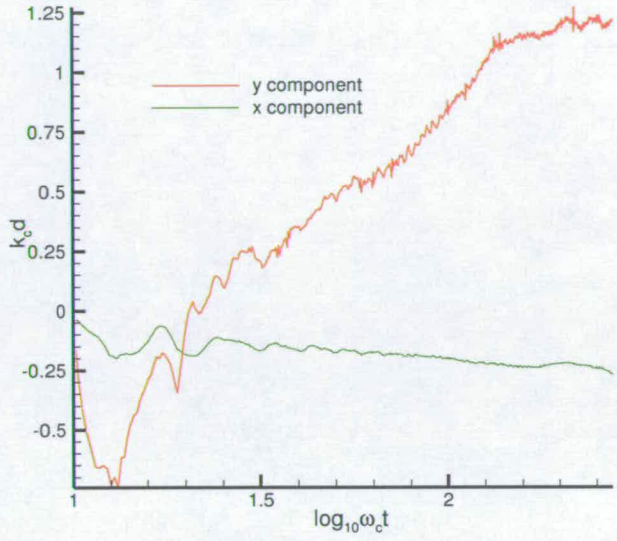

Figure 6.30: Centre of mass against time for single ak = 0.352 breaker

The centre of mass depth increases steadily between $log_{10}\omega_c t = 1.6$ and the end of the experiment with a gradient of -1.07×10^{-1} and final $k_c d$ value of -0.270.

6.5.8 Centre of Mass Results Summary

A clear relationship between breaker amplitude and centre of mass motion can be seen from the results in sections 6.5.1 to 6.5.7. This is plotted in figure 6.31 where the y components for the two smaller breakers are excluded.

The graph shows a general trend with:

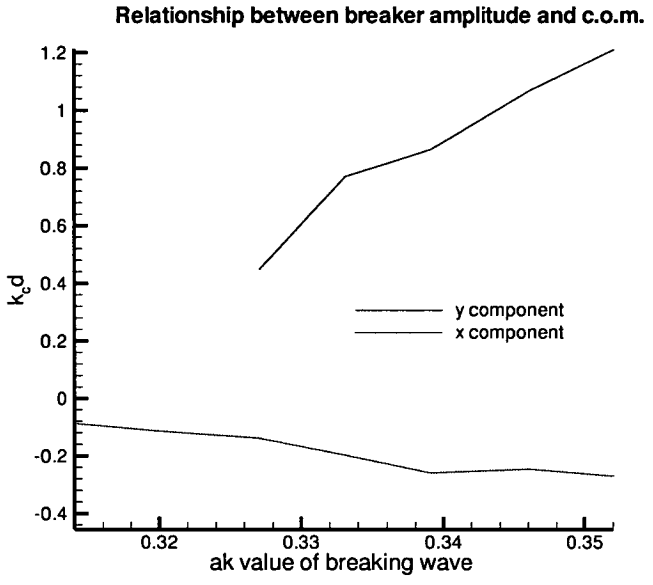

Figure 6.31: Relationship between breaker amplitude and centre of mass motion

$$com_y = 2.88 \times 10^1 ak - 8.92 \tag{6.16}$$

$$com_x = -5.26ak + 1.56 \tag{6.17}$$

These relationships only apply to the c.o.m. positions 50 seconds after breaking.

To obtain more accurate and a longer term relationship, the experiments would have to be repeated to add more points to this graph and cover more amplitudes between 0.314 and 0.352.

6.6 Dispersion Results for Single Breaker

The horizontal and vertical components of the dispersion were examined separately, with individual standard deviations being calculated for each. These were obtained taking the square root of the 2^{nd} order moment, the variance. The results are plotted as $log_{10}\sigma_{xory}k_c$ against $log_{10}\omega_c t$. Figure 6.32 shows the horizontal and vertical dispersion for an $ak = 0.346$ breaker.

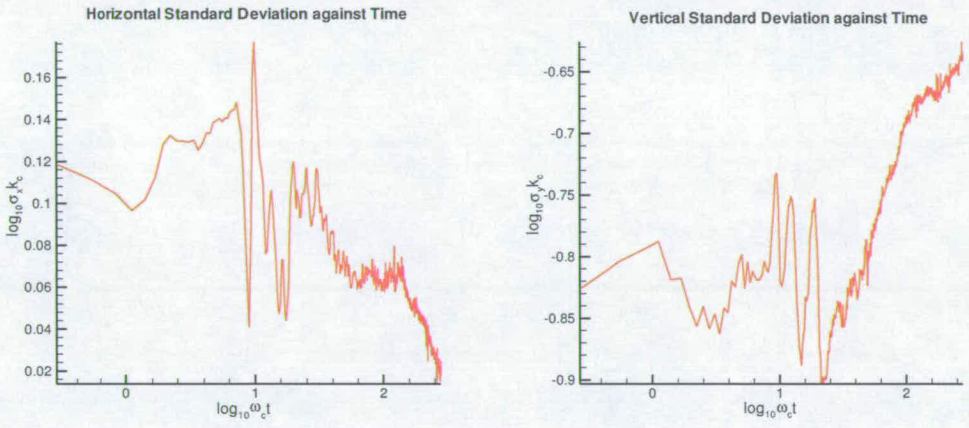

(a) (b)

Figure 6.32: (a)X and (b)Y diffusion for an $ak = 0.346$ breaker

Initially the horizontal standard deviation is large, because the film is spread over the whole water's surface, and the vertical standard deviation is small, because the film is very thin. Immediately following breaking, the standard deviation in the horizontal direction begins to decrease as the dye is mixing in a defined patch. This continues for the remainder of the experiment. The decrease is interesting as it appears to imply the patch decreases in size, which the area

results show is not the case. However, the nature of the standard deviation means that the decrease corresponds to a decreasing size of the higher concentrations, not necessarily the entire dye patch.

The vertical standard deviation started very small, and grew continually as the experiment progressed and the dye mixed further below the surface. Here the standard deviation grows as the experiment continues. This shows that although the higher concentrations may cover a smaller horizontal area as the experiment continues, they cover a larger vertical area.

The standard deviation of the horizontal or vertical components showed no direct amplitude dependence. This can be seen from the results for the other breaking wave amplitudes presented in Appendix C.

6.7 Fractal Dimension Results for Single Breaker

The final measured quantity was the box-counting fractal dimension. During the analysis program, each image was thresholded to remove any background; pixels above the threshold were set to black, below the threshold white.

The thresholded image was then edge detected, once again as part of the analysis program, and the box counting dimension was calculated using a range of ruler sizes from 1 to the vertical variance. A sample graph of log N(s) against log 1/s can be seen in figure 6.33.

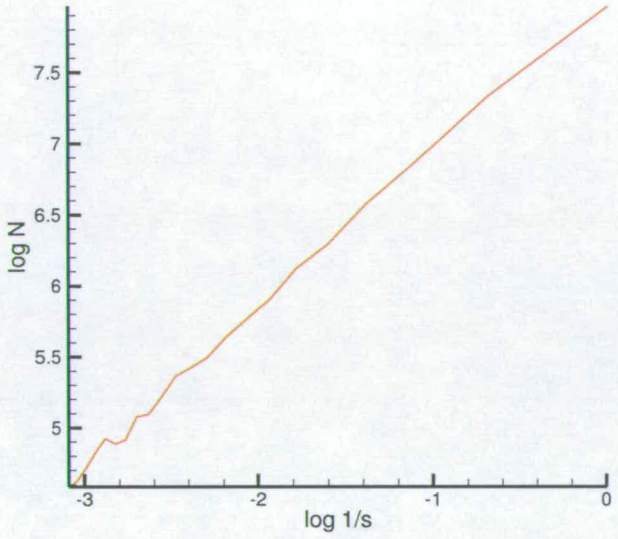

Figure 6.33: Graph of Log N against Log 1/s

As noted by Schlicke [67] using the same analysis software, the value of the threshold had a very large effect of the measured fractal dimension. Four sample graphs are plotted in figure 6.34 using four different threshold values to examine the same breaking wave with an ak amplitude of 0.327.

Essentially, each different threshold value is measuring the box counting dimension of the outline of a given concentration. The most reasonable outline to apply has to be that of the lowest concentration band larger than background measurements. Therefore, for the following box counting results, the threshold level was decided in this manner.

Figure 6.35 shows the box counting dimensions of the dispersion caused by

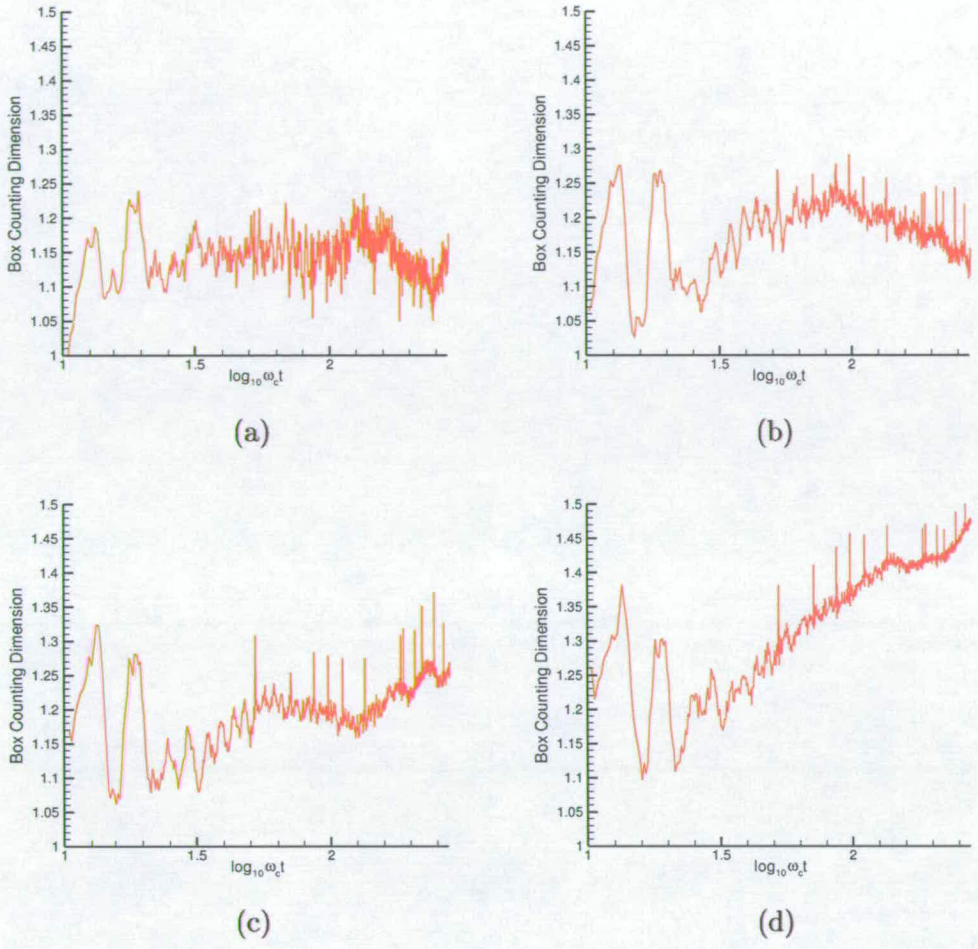

Figure 6.34: Fractal dimension with thresholds of (a)0.015%, (b)0.0075%, (c)0.005% and (d)0.003%

the first four breaking wave amplitudes.

The measured box-counting dimension for the dispersion caused by the breaking wave with a non-dimensional ak amplitude of 0.314 remains level at approximately 1.15 until $log_{10}\omega_c t = 2$, then it rises steadily to approximately 1.25. This small value suggests that there is less active mixing and the dye patch has simply been disturbed from the surface.

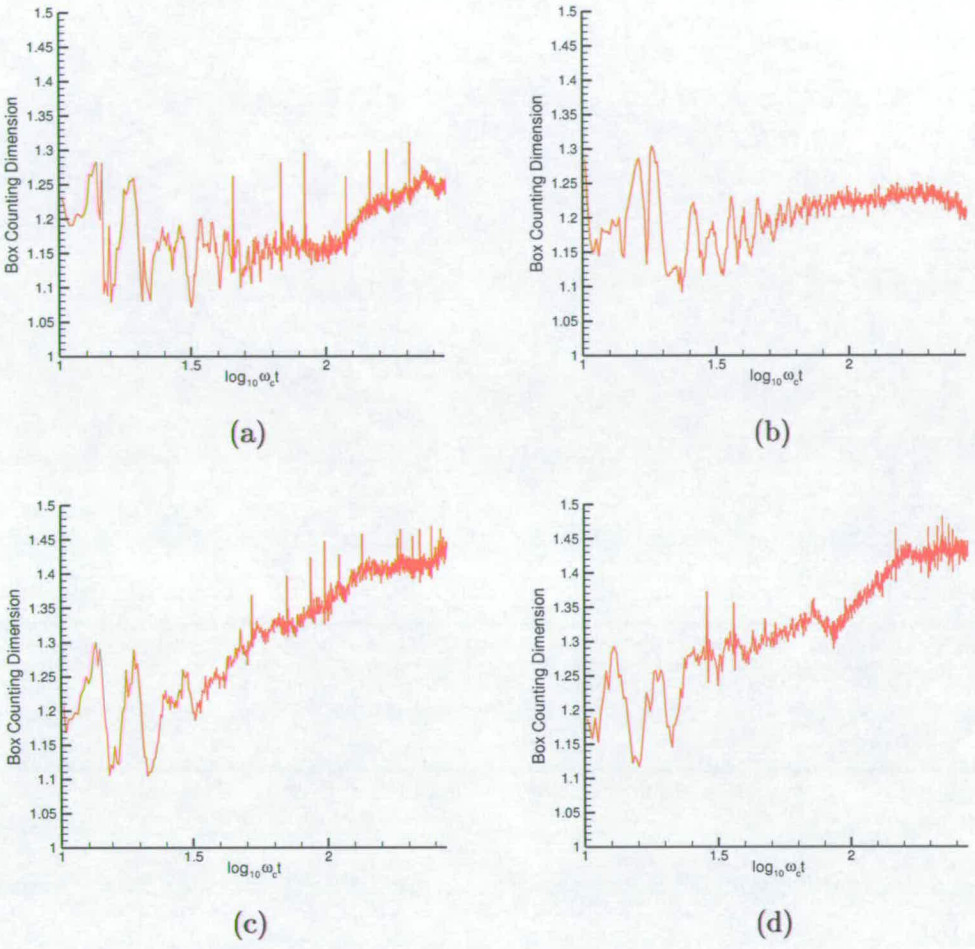

Figure 6.35: Box counting dimension of outline of dispersion caused by breaking waves with ak amplitudes (a)0.314, (b)0.320, (c)0.327 and (d)0.333.

The box-counting dimension for the $ak = 0.320$ breaker remains at a steady value between 1.2 and 1.25 for the entire experiment following the settling of the surface water. This value is lower than both the expected and previous results; this could be due to an underestimate of the necessary threshold value when calculating the fractal dimension.

The next larger size of breaker, $ak = 0.327$ (figure 6.35(c)), shows a much

larger box-counting dimension than the previous two results. The value increases steadily between $log_{10}\omega_c t = 1.5$ and 2.2, reaching a value of approximately 1.4. From $log_{10}\omega_c t = 2.2$ onward the value remains steady. Comparing this result, and higher fractal dimensions calculated for the larger waves, to the lower values for the smaller two breakers suggests that the more energetic plunging processes will create more complex dispersion outlines.

The box-counting dimension calculated for the outline of the mixing caused by a breaking wave with non-dimensional amplitude of $ak = 0.333$ is shown in plot (d) of figure 6.35. There are a number of identifiable regions on this graph. Between $log_{10}\omega_c t = 1.5$ and 1.8 and between 1.9 and 2.2, the fractal dimension is increasing, implying stages of active mixing by turbulence. From $log_{10}\omega_c t = 2.2$ until the end of the experiment the box-counting dimension is constant at approximately 1.45.

The graphs of the calculated box-counting dimension of the outline of the dispersion for the three largest breaking wave amplitudes investigated are shown in figure 6.36.

The graph for the $ak = 0.339$ breaker has a similar final dimension to the 0.333 result but shows a far sharper rise to reach this value between $log_{10}\omega_c t = 2$ and 2.3. Prior to the increase, the box-counting dimension had been approximately 1.3.

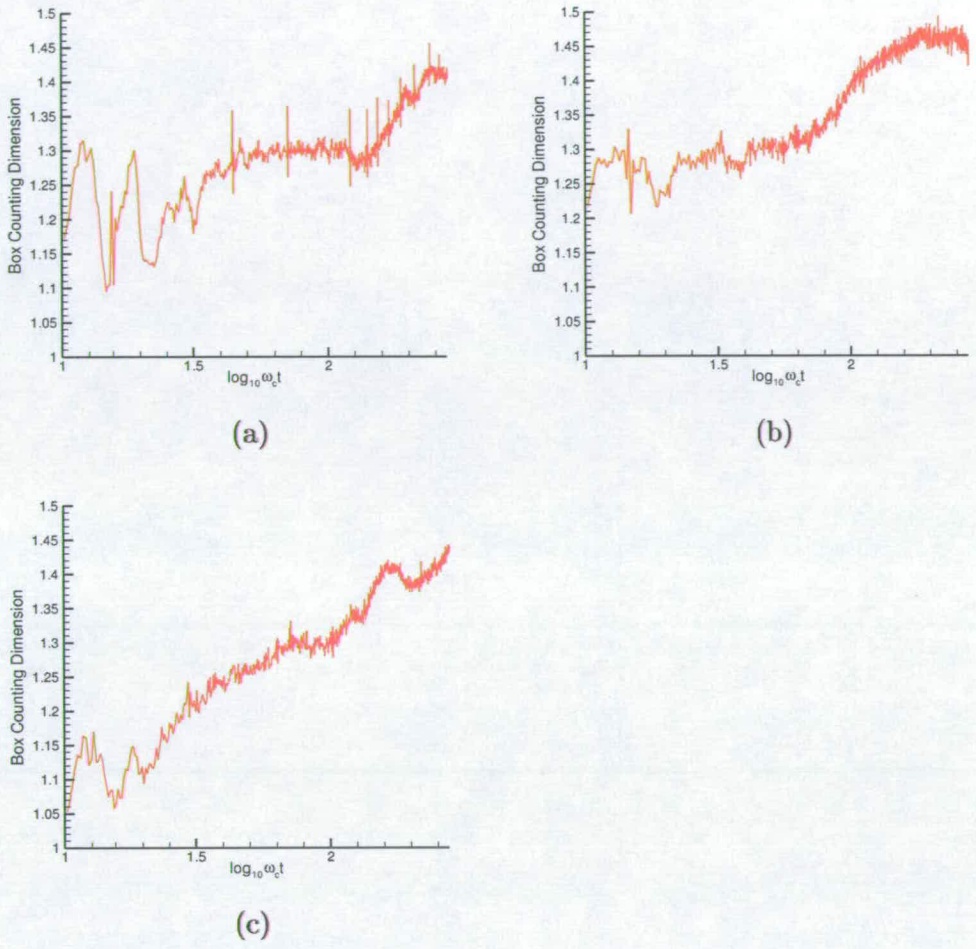

Figure 6.36: Box counting dimension of outline of dispersion caused by breaking waves with ak amplitudes (a)0.339, (b)0.346 and (c)0.352.

Plot (b) in figure 6.36 shows the box-counting dimension of the outline of the dispersion caused by the $ak = 0.346$ plunging breaker. The graph is very similar to the plots shown for the smaller two breaking waves. There is a period with a steady value at approximately 1.3 before a time of increasing fractal dimension, levelling off at 1.45 at the end of the recording. As with the previous results, this could be due to an increasing dominance of smaller length scales producing more

complex outline as turbulence develops.

The final graph, figure 6.36(c), shows the box-counting results for the largest breaking wave, with a non-dimensional ak amplitude of 0.352. This plot shows a more consistent constant increase in fractal dimension over the course of the whole experiment, but once again the final value is approximately 1.45.

Although the actual numerical value of the box-counting dimension is highly dependant on the threshold value used, the qualitative nature of the evolution of the dimension as the experiment continues is still very important. For the two smaller spilling breakers, the measured box-counting dimension was around 1.2. For the plunging breakers the value was greater than 1.4. This suggests that the extra energy provided by the larger breakers during plunging provides a greater complexity to the turbulent mixing. However, the similarity between all the results between ak values of 0.327 and 0.352 suggests that although there is a large increase in energy with larger plungers, there is a limit on the complexity the outline of the mixing can show. This links with the trends shown around the transition point between spilling and breaking shown by the maximum depth and area results

complex outline as turbulence develops.

The final graph, figure 6.36(c), shows the box-counting results for the largest breaking wave, with a non-dimensional ak amplitude of 0.352. This plot shows a more consistent constant increase in fractal dimension over the course of the whole experiment, but once again the final value is approximately 1.45.

Although the actual numerical value of the box-counting dimension is highly dependant on the threshold value used, the qualitative nature of the evolution of the dimension as the experiment continues is still very important. For the two smaller spilling breakers, the measured box-counting dimension was around 1.2. For the plunging breakers the value was greater than 1.4. This suggests that the extra energy provided by the larger breakers during plunging provides a greater complexity to the turbulent mixing. However, the similarity between all the results between ak values of 0.327 and 0.352 suggests that although there is a large increase in energy with larger plungers, there is a limit on the complexity the outline of the mixing can show. This links with the trends shown around the transition point between spilling and breaking shown by the maximum depth and area results

6.8 Single Breaker Conclusions

Five different factors were measured for seven different breaking wave amplitudes. Examining the effect of increasing breaker size on maximum depth reached by a range on concentrations showed some interesting relationships. The lower concentrations penetrated to greater depths with increasing wave size; the larger the ak value, the greater the maximum depth they obtained. The larger concentration values however, reached maximum depths at the cusp between spilling and breaking. The largest spilling breakers caused the greatest maximum depth to be reached by the highest concentrations with the largest plunging breakers producing the shallowest dispersion.

The results in section 6.4 showed that there is a clear connection between breaker size and area covered by the dispersing dye. The larger breakers caused larger overall dispersion patterns. However, as with the maximum depth results, the small spilling breakers actually result in larger areas of higher concentration. Plunging breakers create more expansive mixing with a lower concentration whereas spilling breakers create small, higher concentration dispersion.

By tracking the centre of mass of the film it was possible to examine how the film moved as a whole. The relationship between the x and y components of the centre of mass and the ak value of the wave was found to be approximately linear in the region examined with the form:

$$com_y = 2.88 \times 10^1 ak - 8.92$$

$$com_x = -5.26ak + 1.56$$

implying that larger breaking waves cause greater movement downward and in the wave direction.

The dispersion coefficients were independent of breaker size and demonstrated that the patch showed a greater spreading in the vertical than horizontal direction.

Finally, the fractal-dimension was measured using the box-counting method. Although the actual numerical value was highly dependent on the threshold used, the general trend in the results showed that the plunging breakers produced a more complex outline in the mixing, suggesting greater turbulence and more energetic mixing than the smaller spilling breakers.

The results presented in this chapter show that whilst plunging breakers will cause greater depths and areas to be covered by the dispersing dye, they also lower the concentrations more significantly and move the dispersion further away from its initial starting point than spilling breakers. Therefore, in terms of potential environmental damage, spilling breakers pose a greater threat to species living just below the surface who may be sensitive to higher concentrations of pollutant and plunging breakers will cause the fastest and most widespread dispersion.

Chapter 7

Double Breaker Results

7.1 Introduction

In the previous chapter, the dispersion of a surface film caused by a single breaker was examined. However, in ocean conditions rough enough to produce breaking waves, there are likely to be more than one breaker in a given patch of water. In this chapter the results from experiments on the dispersion caused by a second breaker are examined.

After the surface film has been disturbed by a single breaker, a second breaking wave of identical amplitude is created. This second wave breaks 32 seconds after the first breaker, the fastest the equipment was able to produce. The second breaker was of the same type as the first as it was assumed that in ocean conditions

the following breakers are more likely to be similar to the original than differing in any substantial way.

Initially the maximum depths are presented, then the results for area, centre of mass, dispersion and fractal dimension. Comparisons and conclusions between the dispersion caused by single and double breakers are presented at the end of each section.

7.2 Maximum Depth Results for Second Breaker

The measurements in this chapter are taken after two breaking waves have dispersed the surface film. The initial wave breaks up the surface layer, and the second breaker, of identical amplitude, causes further dispersion. The plots are presented in the same manner as single breaker results; non-dimensional depth against non-dimensional time. The time-axis represents time since the second breaking event, which occurred 32 seconds after the first breaker. This corresponds to a $log_{10}\omega_c t_1$ value of 2.25 where t_1 is the time of the first breaker.

The longer time since the original breaker and the process of a second breaking wave meant that the dye was more likely to leave the lightsheet than in the single breaker experiments. Therefore it was only possible to carry out experiments on three non-dimensional ak amplitudes: 0.314, 0.320 and 0.327, before significant amounts of dye left the lightsheet downstream. Since only three amplitudes were

used, more than one sample result may be presented.

Gradients and intercepts are calculated using a least square fit on Tecplot 9.

7.2.1 Maximum Depth Results for Second $ak = 0.314$ Breaker

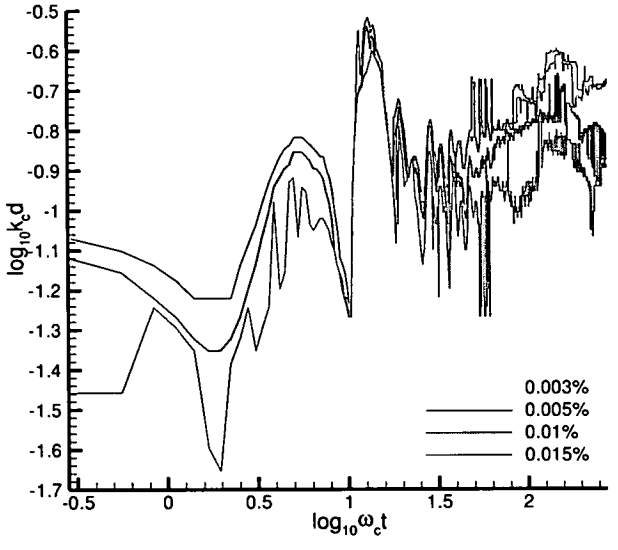

Figure 7.1: Depth against time for second ak = 0.314 breaker

Figure 7.1 shows the maximum depth reached by four concentrations for 50 seconds following a second spilling breaker with an ak value of 0.314. Initially, the maximum depths are spread by the first breaking wave. The values are slightly lower (corresponding to a higher maximum depth) than the $log_{10}\omega_c t_1 = 2.25$ point in figure 6.1. The random nature of the experiment meant it was almost

impossible to recreate the same conditions from the single recorded breaker for the first of the two breakers in these experiments. However, there is a clear distinction between the concentration levels prior to the second breaker.

Following breaking the maximum depth increases for all concentrations. Between $log_{10}\omega_c t = 1.6$ and the end of the experiment (approximately 8 to 50 seconds), the plot for 0.003% shows a general increase of depth with the relationship

$$log_{10}k_c d = 1.49 \times 10^{-1} log_{10}\omega_c t - 9.30 \times 10^{-1} \tag{7.1}$$

There is also a period of steadily increasing maximum depth for the plot of 0.01% concentration between $log_{10}\omega_c t = 1.6$ and 2.1 with a gradient of 3.44×10^{-1} and an intercept of -1.48.

Both dispersion exponents are less than 0.5, implying a subdiffusive descent of the maximum depth. This is unsurprising as the maximum depth is very sensitive to individual eddies and motion within the fluid and therefore is unlikely to descend consistently.

The final depths reached by the measured concentrations, 0.003%, 0.005%, 0.01%, 0.015% were $log_{10}k_c d$ = -0.55, -0.67, -0.82 and -0.90 respectively.

7.2.2 Maximum Depth Results for Second $ak = 0.320$ Breaker

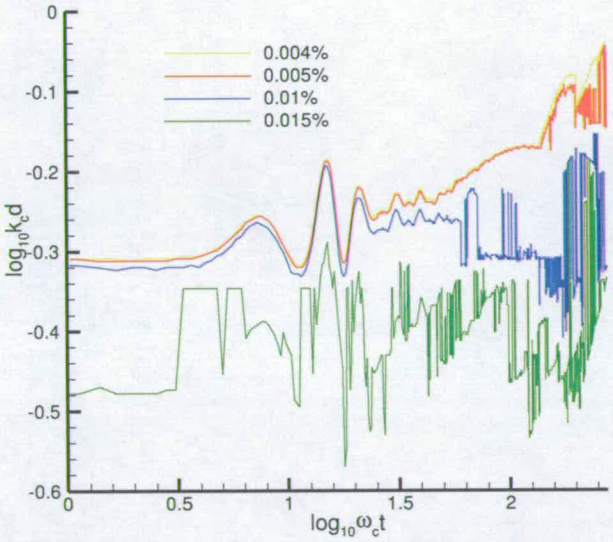

Figure 7.2: Depth against time for second ak = 0.320 breaker (first example)

The next set of breakers examined had ak values of 0.320. The first graph of maximum depths reached for this amplitude of breaker is presented in figure 7.2. Four concentrations are plotted, 0.004%, 0.005%, 0.01% and 0.015%. The initial values compare well with the concentration maximum depth levels for the single breaker after $log_{10}\omega_c t_1 = 2.25$, shown in figure 6.2.

The lower two concentrations show very similar behaviour with three definite regions between $log_{10}\omega_c t = 1.65$ and 2.15, 2.15 and 2.3, and 2.3 and the end of the experiment. In the first region, from $log_{10}\omega_c t = 1.65$ to 2.15, (8 to 25 seconds after

breaking), both lines show a steady increase in maximum depth with gradients and intercepts of 1.39×10^{-1} and 1.40×10^{-1}, and -4.57×10^{-1} and -4.60×10^{-1} for 0.004% and 0.005% respectively.

This is followed by a period of far quicker increasing maximum depth, probably caused by a specific eddy pulling the dye further from the surface. The relationships for the two lower concentrations in this region are:

$$log_{10}k_cd = 6.28 \times 10^{-1} log_{10}\omega_c t - 1.50 \tag{7.2}$$

$$log_{10}k_cd = 5.75 \times 10^{-1} log_{10}\omega_c t - 1.39 \tag{7.3}$$

At $log_{10}\omega_c t = 2.15$, there is a sharp decrease in the maximum depth value followed by another steady period of growth. This final region, for the 0.004% concentration, has a gradient of 5.73×10^{-1} and intercept of 1.44.

The larger concentrations show different behaviour. The maximum depth plot for the 0.01% concentration, despite a series of sharp individual peaks, shows very little change over the course of the whole experiment. Between $log_{10}\omega_c t = 1.9$ and 2.1 the line is almost level, showing a very slight increase with a gradient of 2.23×10^{-3}. This period with no change in maximum depth suggests that the dye which is producing this reading reached this depth after the first breaking wave and was not being affected by the turbulent motion created by the second

breaker.

The largest concentration measured, 0.015%, shows a series of regions where the maximum depth increases before falling again. Each of these regions have a large number of sharp peaks, possibly corresponding to small areas of dye entering or leaving the lightsheet. The final part of the graph, from $log_{10}\omega_c t = 2.25$ to the end of the experiment shows a period of increasing maximum depth, discounting the sharp peaks. The gradient of this region is 7.34×10^{-1}.

The final depths reached by the 0.004%, 0.005%, 0.01% and 0.015% concentrations were $log_10 k_c d$ = -0.04, -0.05, -0.32 and -0.34 respectively.

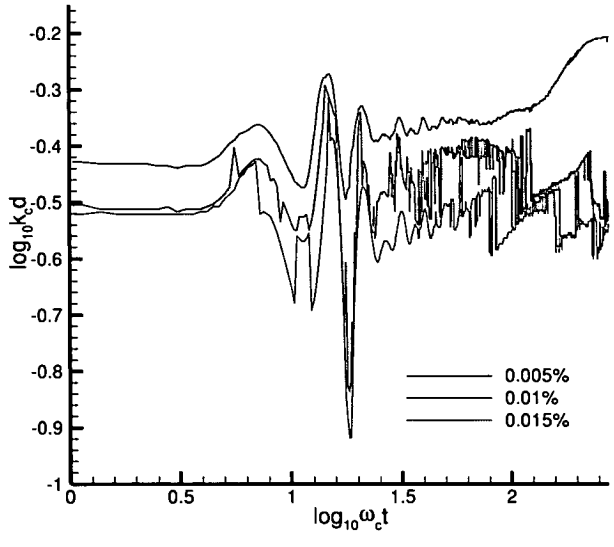

Figure 7.3: Depth against time for second ak = 0.320 breaker (second example)

Figure 7.3 shows another set of results for a second $ak = 0.320$ breaker experi-

ment. Again, the initial concentration values match the single breaker experiment favourably. The smallest concentration on the graph, 0.005%, remains steady at $log_{10}k_cd$ = -0.35 until $log_{10}\omega_ct$ = 2.1. Between this point and $log_{10}\omega_ct$ = 2.4 the maximum depth increases with the relationship

$$log_{10}k_cd = 4.93 \times 10^{-1} log_{10}\omega_ct - 1.37 \tag{7.4}$$

The 0.01% concentration shows a steady increase between 22 and 38 seconds ($log_{10}\omega_ct$ = 2.1 and 2.3) with a gradient and intercept of 2.47×10^{-1} and -1.01 respectively. The final value of the maximum depth for 0.01% concentration, $log_{10}k_cd$ = -0.52, is very similar to the initial value, suggesting the second breaker has little effect on increasing the maximum depth for this concentration.

The largest concentration, 0.015%, shows a period of steady increasing depth between $log_{10}\omega_ct$ = 1.95 and 2.2 with a gradient and intercept of 3.57×10^{-1} and -1.26. Following this, the maximum depth falls to $log_{10}k_cd$ = -0.6 and remains around this level until the end of the experiment. This final value is less than the initial value, suggesting the second breaker disperses the higher concentrations more than a single breaker.

The final depths reached by the three concentrations are $log_{10}k_cd$ = -0.21, -0.52 and -0.54 for 0.005%, 0.01% and 0.015% respectively.

The third graph in this section, figure 7.4, also contains plots of maximum

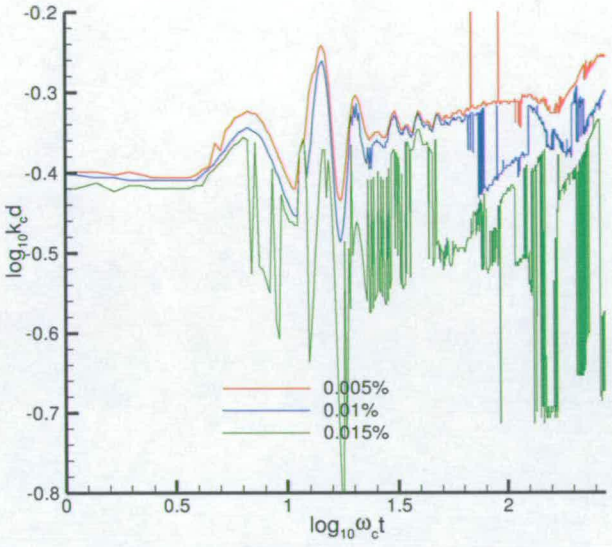

Figure 7.4: Depth against time for second ak = 0.320 breaker (third example)

depth for 0.005%, 0.01% and 0.015% concentrations after a second $ak = 0.320$ breaker. In this figure, the initial maximum depth values match very closely to the values at $log_{10}\omega_c t_1 = 2.25$ in figure 6.2.

Following breaking, the concentrations remain approximately steady before increasing in maximum depth in the final stages of the experiment. Between $log_{10}\omega_c t = 2.22$ and the end of the experiment the plot for 0.005% shows linear growth with the relationship

$$log_{10}k_c d = 3.19 \times 10^{-1} log_{10}\omega_c t - 1.03 \tag{7.5}$$

reaching a final value of $log_{10}k_cd$ = -0.26.

Between $log_{10}\omega_c t = 1.9$ and the end the experiment three regions can be seen in the line representing the maximum depth of the 0.01% concentration. In the first region, $log_{10}\omega_c t = 1.9$ to 2.1, the plot shows a steady increase with a gradient of 2.06×10^{-1}. Following this there is a sharp increase in maximum depth then a steady decrease with a gradient of -3.24×10^{-1}. This could be due to a patch of diffusing or ascending dye entering the lightsheet at $log_{10}\omega_c t = 2.1$. The final region of the graph shows an approximately linear increase in maximum depth again, this time with the relationship

$$log_{10}k_cd = 4.71 \times 10^{-1} log_{10}\omega_c t - 1.45 \tag{7.6}$$

The largest concentration shows a series of sharp positive and negative peaks throughout the experiment. Near the end of the experiment, between 43 and 47 seconds, there is a smooth region of linear increasing maximum depth with a gradient and intercept of 6.12×10^{-1} and -1.81 respectively.

The final depths reached by the three concentrations, smallest to largest respectively, were $log_{10}k_cd$ = -0.26, -0.30 and -0.56.

Figure 7.5 shows the final graph of maximum depth against time for a second $ak = 0.320$ breaker. The initial maximum depth values exhibit a larger spread than the previous figure.

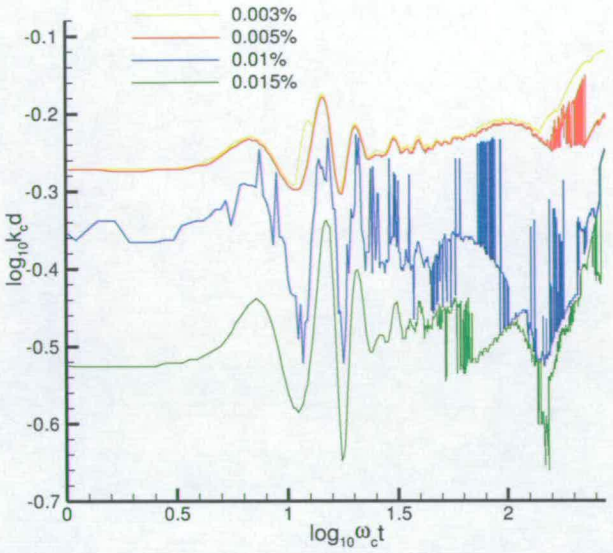

Figure 7.5: Depth against time for second ak = 0.320 breaker (fourth example)

The maximum depths for 0.003% and 0.005% concentrations remain close together until $log_{10}\omega_c t = 2.15$, when the lower concentration begins to descend until the end of the experiment, described by

$$log_{10}k_c d = 3.73 \times 10^{-1} - 1.02 \tag{7.7}$$

The plot for 0.005% follows this descent with a series of sharp peaks until $log_{10}\omega_c t = 2.35$ when it settles on a lower value before increasing again with a gradient of 3.87×10^{-1}.

The line representing 0.015% shows a short period of increasing maximum

depth between $log_{10}\omega_c t = 1.84$ and 2.04 with a gradient of 2.63×10^{-1} and similarly between $log_{10}\omega_c t = 2.2$ and 2.35 with a gradient of 8.06×10^{-1}.

The final maximum depths reached by the three concentrations are $log_{10}k_c d$ = -0.20, -0.25 and -0.25 for 0.005% , 0.01% and 0.015% respectively.

7.2.3 Maximum Depth Results for Second $ak = 0.327$ Breaker

The final size of breaking wave examined was $ak = 0.327$. Breakers with ak amplitudes of 0.333, 0.339, 0.346 and 0.352 were too large to take meaningful second breaker measurements on as they caused too much dye to leave the lightsheet.

Four graphs of maximum depth reaches as a function of concentration caused by a second $ak = 0.327$ breaker are presented in this section.

The first graph is shown in figure 7.6. This graph shows the maximum depths reached by 0.004%, 0.005% and 0.01% concentrations beneath a second $ak = 0.327$ breaker. The depths at $log_{10}\omega_c t = 0$ match well with the values at $log_{10}\omega_c t_1$ in figure 6.3. The lowest concentration, 0.004%, remains approximately steady until $log_{10}\omega_c t = 1.75$ and then grows linearly between this point and $log_{10}\omega_c t = 2.32$ (10 to 38 seconds after breaking) as

$$log_{10}k_c d = 2.50 \times 10^{-1} log_{10}\omega_c t - 7.56 \times 10^{-1} \tag{7.8}$$

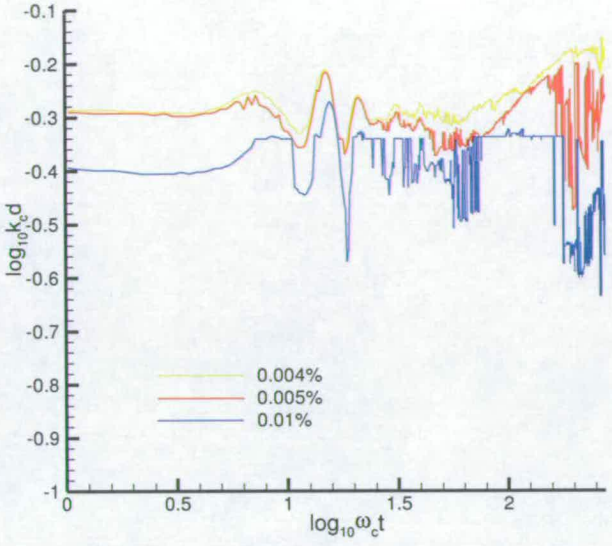

Figure 7.6: Depth against time for second ak = 0.327 breaker (first example)

before levelling off.

The slightly larger concentration, 0.005%, shows a similar period of increasing maximum depth between $log_{10}\omega_c t = 1.88$ and 2.17 with a gradient of 3.86×10^{-1} - 1.06 before becoming erratic towards the end of the experiment.

The most interesting features of the 0.01% line are the flat regions in the plot. Between $log_{10}\omega_c t = 1.88$ and 2.17 the maximum depth for 0.01% is described by the equation

$$log_{10}k_c d = -4.09 \times 10^{-3} log_{10}\omega_c t - 3.28 \times 10^{-1} \tag{7.9}$$

The maximum depths reached at the end of the experiment by concentration levels 0.004%, 0.005% and 0.01% were $log_{10}k_cd$ = -0.17, -0.26 and -0.46.

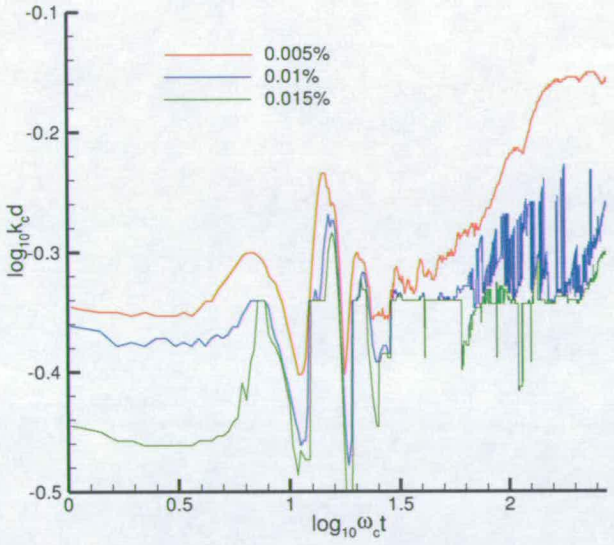

Figure 7.7: Depth against time for second ak = 0.327 breaker (second example)

The second graph in this section, figure 7.7, shows the maximum depths reached by 0.005%, 0.01% and 0.015% concentrations after two $ak = 0.327$ breakers. The maximum depth values at $log_{10}\omega_c t = 0$ compare favourably with the values for a single breaker.

The smallest concentration on this graph, 0.005%, shows two periods of steady increasing maximum depth from $log_{10}\omega_c t = 1.87$ to 2.02, and 2.06 and 2.18, with a brief decrease inbetween. The relationships between maximum depth and time for these two regions are given by

$$log_{10}k_cd = 4.41 \times 10^{-1} log_{10}\omega_c t - 1.10 \tag{7.10}$$

$$log_{10}k_cd = 4.50 \times 10^{-1} log_{10}\omega_c t - 1.14 \tag{7.11}$$

The maximum depth value measured for the 0.01% concentration fluctuates between $log_{10}k_cd$ = -0.34 and -0.26 until showing a steady increase at the end of the experiment, starting at $log_{10}\omega_c t = 2.4$. In this region, the plot has a gradient of 7.26×10^{-1}.

Similar behaviour is shown by the 0.015% graph at the end of the experiment, starting at $log_{10}\omega_c t = 2.35$, with a gradient of 3.83×10^{-1}. Prior to this, the maximum depth value remains approximately constant, implying the motion of the second breaker is not greatly affecting this maximum depth reading in this region.

The final maximum depths reached by 0.005%, 0.01% and 0.015% concentration in this experiment were $log_{10}k_cd$ = -0.15, -0.26 and -0.30 respectively.

Figure 7.8 shows the same concentrations as figure 7.7. However, the largest concentrations reach slightly greater maximum depths. The maximum depth for 0.005% remains approximately constant until 35 seconds after breaking ($log_{10}\omega_c t$ = 2.29) and then increases with the relationship

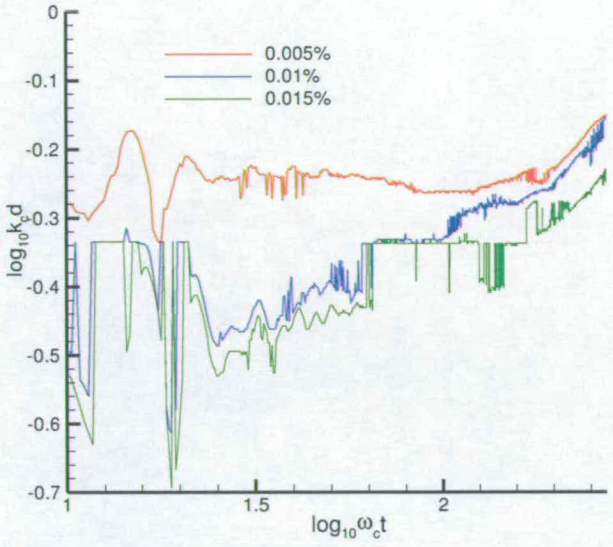

Figure 7.8: Depth against time for second ak = 0.327 breaker(third example)

$$log_{10}k_cd = 5.76 \times 10^{-1} log_{10}\omega_c t - 1.55 \tag{7.12}$$

until the end of the experiment.

A similar increase in maximum depth for the 0.01% concentration begins earlier in the experiment, $log_{10}\omega_c t = 2.18$ and continues until the end with a gradient of 4.57×10^{-1}. Prior to this, the maximum depth value is approximately constant, as is the value for the 0.015% concentration. The largest concentration grows from $log_{10}\omega_c t = 2.34$ until the end of the experiment with a gradient of 5.62×10^{-1}.

At the end of the experiment the concentrations 0.005%, 0.01%, 0.015% had maximum depth values of $log_{10}k_cd$ of 0.15, -0.15, and -0.25 respectively.

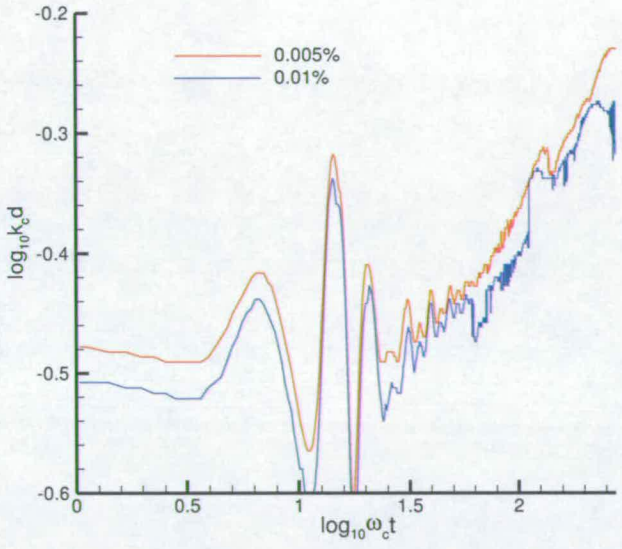

Figure 7.9: Depth against time for second ak = 0.327 breaker (fourth example)

The final maximum depth results are shown in figure 7.9. This graph shows only two concentration values, 0.005% and 0.01%. The initial maximum depths are much lower than the $log_{10}\omega_c t_1 = 2.25$ value for the single breaker. However, the maximum depths increase rapidly after the second breaker, in two clear regions for each concentration.

The 0.005% concentration increases in maximum depth between $log_{10}\omega_c t =$ 1.79 and 2.09 and again between 2.14 and 2.42. In these two regions the plot of $log_{10}k_cd$ against $log_{10}\omega_c t$ can be described by the two equations

$$log_{10}k_cd = 3.65 \times 10^{-1} - 1.09 \tag{7.13}$$

$$log_{10}k_cd = 3.83 \times 10^{-1} - 1.15 \tag{7.14}$$

Two regions of increasing depth for the 0.01% concentration can be seen between $log_{10}\omega_c t = 1.86$ and 2.04, and 2.18 and 2.36. The relationships for these two sections are given by

$$log_{10}k_cd = 2.38 \times 10^{-1} - 1.15 \tag{7.15}$$

$$log_{10}k_cd = 3.87 \times 10^{-1} - 1.18 \tag{7.16}$$

The final maximum depths reached by 0.005% and 0.01% concentrations are $log_{10}k_cd$ = -0.23 and -0.32.

7.2.4 Maximum Depth Results Summary

Graphs of maximum depth reached for given concentrations are presented for breaking waves of non-dimensional amplitudes 0.314, 0.320 and 0.327. Whilst the graphs are all slightly different, the same trends appear a number of times. For the larger concentrations of the $ak = 0.327$ breaking wave there are regions where

the maximum depth remains almost constant. This implies the second breaking wave is not having a large effect on the motion of the deepest areas of dye in this region. This can also be seen to a lesser effect on the larger concentration in the $ak = 0.320$ experiments.

The difference between the initial and final maximum depths for the measured concentrations is obviously very important. A summary of these values is presented in table 7.1, where the number in parenthesis denotes the number of the figure where the appropriate results are displayed.

Concentration	ak value	Initial $log_{10}k_cd$	Final $log_{10}k_cd$	Difference
0.003%	0.314	-0.63	-0.55	0.08
0.005%	0.314	-0.83	-0.67	0.16
0.01%	0.314	-0.99	-0.82	0.17
0.015%	0.314	-1.07	-0.90	0.17
0.004%	0.320(7.2)	-0.29	-0.04	0.25
0.005%	0.320(7.2)	-0.39	-0.05	0.34
0.01%	0.320(7.2)	-0.72	-0.32	0.40
0.015%	0.320(7.2)	-0.95	-0.34	0.61
0.005%	0.320(7.3)	-0.44	-0.21	0.23
0.01%	0.320(7.3)	-0.83	-0.52	0.31
0.015%	0.320(7.3)	-0.99	-0.54	0.45
0.005%	0.320(7.4)	-0.46	-0.26	0.20
0.01%	0.320(7.4)	-0.80	-0.30	0.50
0.015%	0.320(7.4)	-1.03	-0.57	0.46
0.003%	0.320(7.5)	-0.15	-0.12	0.03
0.005%	0.320(7.5)	-0.34	-0.20	0.14
0.01%	0.320(7.5)	-0.79	-0.25	0.54
0.015%	0.320(7.5)	-0.98	-0.25	0.73
0.004%	0.327(7.6)	-0.29	-0.17	0.12
0.005%	0.327(7.6)	-0.49	-0.26	0.23
0.01%	0.327(7.6)	-0.84	-0.46	0.38
0.005%	0.327(7.7)	-0.21	-0.15	0.06
0.01%	0.327(7.7)	-0.60	-0.26	0.34
0.015%	0.327(7.7)	-0.81	-0.30	0.51
0.005%	0.327(7.8)	-0.34	-0.15	0.19
0.01%	0.327(7.8)	-0.60	-0.15	0.45
0.015%	0.327(7.8)	-0.86	-0.25	0.61
0.005%	0.327(7.9)	-0.45	-0.23	0.22
0.01%	0.327(7.9)	-0.86	-0.32	0.54

Table 7.1: Depth values for second breaking wave results (brackets denotes figure)

It can be seen for all experiments (except 0.320(7.4)) that the large concentrations show a greater increase in maximum depth due to the second breaker than the lower values. This greater increase in not necessarily due to larger breaking wave amplitude.

The initial results imply that a second breaker dramatically increases the depth to which the greater concentrations penetrate. This will be looked at in more detail in the following chapter.

Further research must be carried out to draw more conclusive results and this is discussed in section 8.5

7.2.5 Comparison Between Single and Double Breaking Wave Maximum Depth Results

For single breaking waves the results suggest that there is a direct link between wave amplitude and depth reached for the lower concentrations, around 0.005%. However, the results for a second breaker show that there is little difference between the depth reached by this concentration for breaking waves with amplitudes of 0.320 or 0.327.

One of the most interesting results from the single breaking wave experiments was the discovery that the depth reached for the highest concentration band was at its greatest for the largest spilling breakers. As it was impossible to measure

second breaking wave experiments with plunging breakers, this result could not be examined for further breaking waves.

In every case, a second breaking wave resulted in greater maximum depths, although further research must be carried out to confirm whether this is due to a second breaking wave or simply a longer time scale following the first breaker.

7.3 Area Results for Second Breaker

The next quantity calculated from the experiments to be presented is the area covered by the film as it disperses. Section 6.4 looked at the area results for a single breaking wave, this section examines the area results after a second breaking wave has added further energy to the mixing.

As with graphs in section 6.4, the results are plotted as non-dimensional time against non-dimensional area in a log-log format.

Gradients and dispersion coefficients are calculated and summarised at the end of the section. Primarily, the concentrations 0.004%, 0.005% and 0.015% are examined.

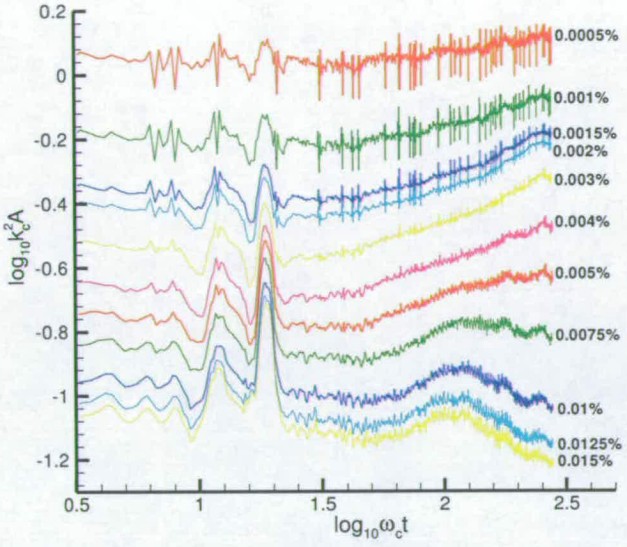

Figure 7.10: Area against time for second ak = 0.314 breaker (first example)

7.3.1 Area Results for Second $ak = 0.314$ Breaker

The first graph, figure 7.10, shows the changing area of a range concentrations beneath a second $ak = 0.314$ breaking wave. The initial spread of concentrations is caused by the first breaking wave and the peaks and troughs between $log_{10}\omega_c t = 1$ and 1.3 correspond to the second breaking wave.

The three plots of 0.003%, 0.004% and 0.005% are very similar between $log_{10}\omega_c t = 1.74$ and 2.42. The equations of these concentrations in this region are

$$log_{10}k_c^2 A_{0.003\%} = 3.16 \times 10^{-1} log_{10}\omega_c t - 1.09 \tag{7.17}$$

$$log_{10}k_c^2 A_{0.004\%} = 2.64 \times 10^{-1} log_{10}\omega_c t - 1.11 \tag{7.18}$$

$$log_{10}k_c^2 A_{0.005\%} = 1.87 \times 10^{-1} log_{10}\omega_c t - 1.06 \tag{7.19}$$

The three dispersion coefficients calculated from these equations are 1.78×10^{-4}, 3.12×10^{-5} and 1.07×10^{-6} for 0.003%, 0.004% and 0.005% respectively. The relationships between area and time for these three concentrations is therefore given by

$$A_{0.003\%} = \frac{(2 \times 1.78 \times 10^{-4} \times \omega_c t)^{0.316}}{k_c^2} \tag{7.20}$$

$$A_{0.004\%} = \frac{(2 \times 3.12 \times 10^{-5} \times \omega_c t)^{0.264}}{k_c^2} \tag{7.21}$$

$$A_{0.005\%} = \frac{(2 \times 1.07 \times 10^{-6} \times \omega_c t)^{0.187}}{k_c^2} \tag{7.22}$$

The larger concentrations show a similar increase in area between 10 and 20 seconds after breaking ($log_{10}\omega_c t = 1.74$ to 2.04). During this time, the lines representing 0.01%, 0.0125% and 0.015% have the linear approximations

$$log_{10}k_c^2 A_{0.01\%} = 3.57 \times 10^{-1} log_{10}\omega_c t - 1.64 \tag{7.23}$$

$$log_{10}k_c^2 A_{0.0125\%} = 3.01 \times 10^{-1} log_{10}\omega_c t - 1.62 \tag{7.24}$$

$$log_{10}k_c^2 A_{0.015\%} = 2.82 \times 10^{-1} log_{10}\omega_c t - 1.63 \tag{7.25}$$

which, in turn, gives

$$A_{0.01\%} = \frac{(2 \times 1.27 \times 10^{-5} \times \omega_c t)^{0.357}}{k_c^2} \tag{7.26}$$

$$A_{0.0125\%} = \frac{(2 \times 2.07 \times 10^{-6} \times \omega_c t)^{0.301}}{k_c^2} \tag{7.27}$$

$$A_{0.015\%} = \frac{(2 \times 8.30 \times 10^{-7} \times \omega_c t)^{0.282}}{k_c^2} \tag{7.28}$$

Following the increase there is a steady decrease until the end of the experiment. The three concentrations have gradients -3.37 $\times$ 10^{-1}, -3.92 $\times$ 10^{-1} and -4.15 $\times$ 10^{-1} for 0.01%, 0.0125% and 0.015%.

The initial and final areas covered by the concentrations are shown in table 7.2 and graph 7.11. Results are presented as $k_c^2 A$ to make interpretation clearer than using logarithmic values.

This implies a CCA value of approximately 0.0075%.

Concentration	Initial $k_c^2 A$	Final $k_c^2 A$	Difference
0.0005%	1.03	1.25	0.22
0.001%	0.595	0.816	0.221
0.0015%	0.423	0.646	0.223
0.002%	0.375	0.598	0.223
0.003%	0.287	0.468	0.181
0.004%	0.213	0.333	0.120
0.005%	0.172	0.231	0.059
0.0075%	0.140	0.149	0.009
0.01%	0.111	0.092	-0.019
0.0125%	0.097	0.072	-0.025
0.015%	0.089	0.062	-0.027

Table 7.2: Concentration areas for a second $ak = 0.314$ breaker

The second breaker in this section, shown in figure 7.12, is also for a second $ak = 0.314$ breaker. As in figure 7.10, gradients, intercepts and dispersion coefficients can be calculated for the concentrations 0.003%, 0.004% and 0.005%. Between $log_{10}\omega_c t = 1.62$ and 2.18 the areas are given by

$$log_{10} k_c^2 A_{0.003\%} = 2.50 \times^{-1} -1.00 \tag{7.29}$$

$$log_{10} k_c^2 A_{0.004\%} = 2.11 \times^{-1} -1.05 \tag{7.30}$$

$$log_{10} k_c^2 A_{0.005\%} = 1.59 \times^{-1} -1.03 \tag{7.31}$$

Calculating the dispersion coefficients gives;

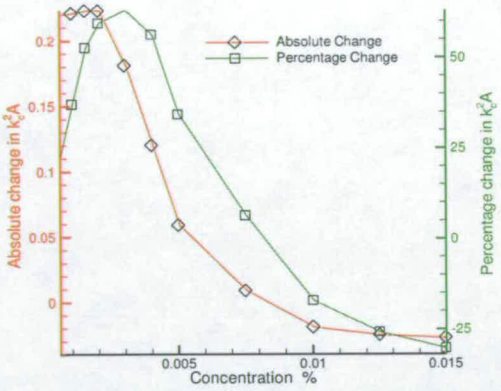

Figure 7.11: Change in $k_c^2 A$ against concentration for a second $ak = 0.314$ breaker (first example)

$$A_{0.003\%} = \frac{(2 \times 5 \times 10^{-5} \omega_c t)^{0.250}}{k_c^2} \tag{7.32}$$

$$A_{0.004\%} = \frac{(2 \times 5.28 \times 10^{-6} \omega_c t)^{0.211}}{k_c^2} \tag{7.33}$$

$$A_{0.005\%} = \frac{(2 \times 1.66 \times 10^{-7} \omega_c t)^{0.159}}{k_c^2} \tag{7.34}$$

A graph of the difference between initial and final areas is presented in figure 7.13. The red left hand axis shows the absolute change in $k_c^2 A$ over the recording time of the experiment and the green right hand axis shows the percentage change. A discussion of this result and similar results for large breakers will be given in the summary.

This implies a CCA value of 0.0075%.

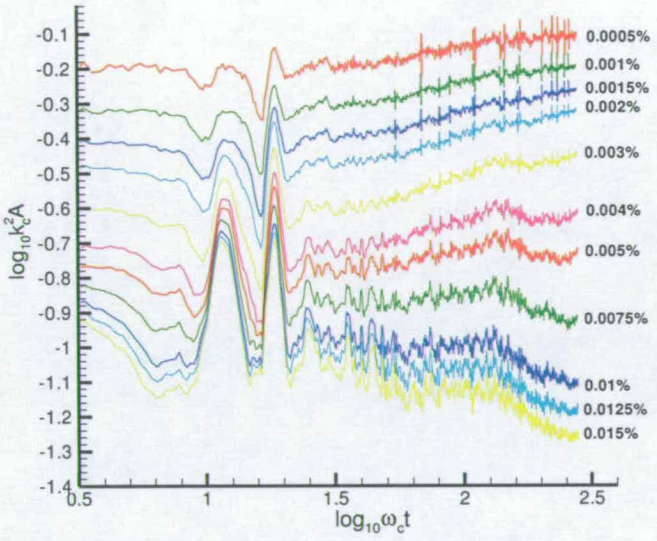

Figure 7.12: Area against time for second ak = 0.314 breaker (second example)

7.3.2 Area Results for Second $ak = 0.320$ Breaker

Five graphs of area results for second $ak = 0.320$ breakers are presented in this section. The first graph is presented in figure 7.14.

The lines representing the smallest concentrations, 0.0005% to 0.001% are very close together and show only a gentle increase in area throughout the experiment, mirrored at a slightly lower area by the 0.002% and 0.003% readings. This implies the background level for this experiment was around 0.002%.

Between $log_{10}\omega_c t = 1.62$ and the end of the experiment, the areas of 0.004%, 0.005% and 0.0075% have the following relationships to time

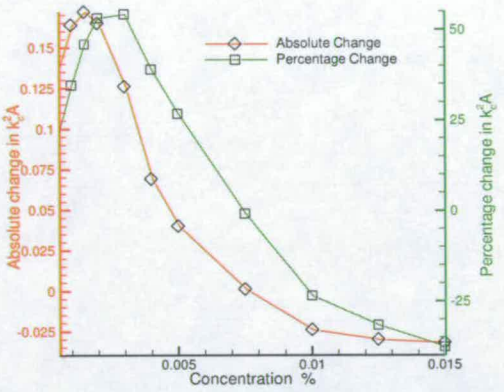

Figure 7.13: Change in $k_c^2 A$ against concentration for a second $ak = 0.314$ breaker (second example)

$$log_{10} k_c^2 A_{0.004\%} = 1.50 \times 10^{-1} log_{10} \omega_c t - 5.37 \times 10^{-1} \tag{7.35}$$

$$log_{10} k_c^2 A_{0.005\%} = 5.15 \times 10^{-2} log_{10} \omega_c t - 5.06 \times 10^{-1} \tag{7.36}$$

$$log_{10} k_c^2 A_{0.0075\%} = -1.83 \times 10^{-1} log_{10} \omega_c t - 3.42 \times 10^{-1} \tag{7.37}$$

Using the formula $D = \frac{10^{\frac{c}{H}}}{2}$, where D is the dispersion coefficient, c is the intercept and H the dispersion exponent, the area for 0.004% can be described by

$$A_{0.004\%} = \frac{(2 \times 1.32 \times 10^{-4} \omega_c t)^{0.150}}{k_c^2} \tag{7.38}$$

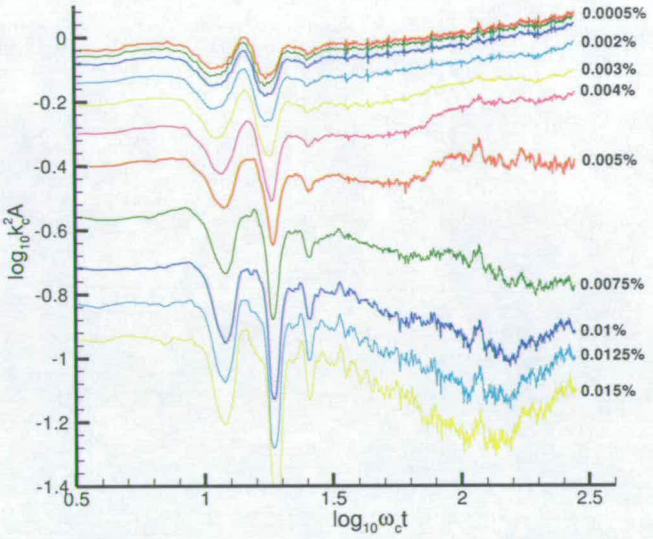

Figure 7.14: Area against time for second ak = 0.320 breaker (first example)

The plots for the largest three concentrations measured, 0.01%, 0.0125% and 0.015%, all show similar decreasing area between $log_{10}\omega_c t = 1.62$ and 2.18 (seven and a half to twenty seven and a half seconds after breaking). Following this, there is a period of increasing area again. In the first region, the equations describing the decreasing areas are

$$log_{10}k_c^2 A_{0.01\%} = -2.82 \times 10^{-1} log_{10}\omega_c t - 3.42 \times 10^{-1} \tag{7.39}$$

$$log_{10}k_c^2 A_{0.0125\%} = -3.15 \times 10^{-1} log_{10}\omega_c t - 4.45 \times 10^{-1} \tag{7.40}$$

$$log_{10}k_c^2 A_{0.015\%} = -3.66 \times 10^{-1} log_{10}\omega_c t - 4.86 \times 10^{-1} \tag{7.41}$$

The differences between initial and final areas are presented in figure 7.15. This figure implies a CCA value of 0.005%.

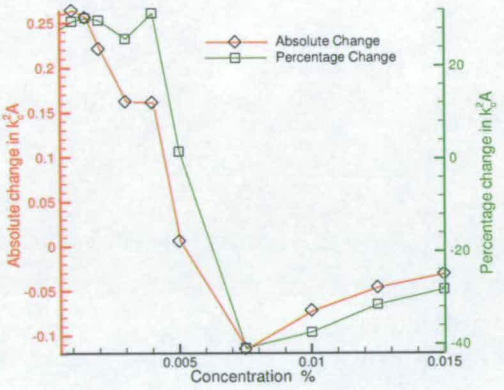

Figure 7.15: Change in k_c^2A against concentration for an $ak = 0.320$ breaker (first example)

The second graph of areas covered for a second $ak = 0.320$ breaker is shown in figure 7.16.

The smaller concentrations show a greater spread in this experiment due to lower background dye levels. However, the lines themselves are almost level, the 0.0015% concentration shows a gradient of 5.04 $\times 10^{-2}$ between $log_{10}\omega_c t = 1.64$ and the end of the experiment.

This characteristic is shared by most of the concentration values in this experiment, the relationship between log area and log time for the 0.005% concentration in the same period is given by

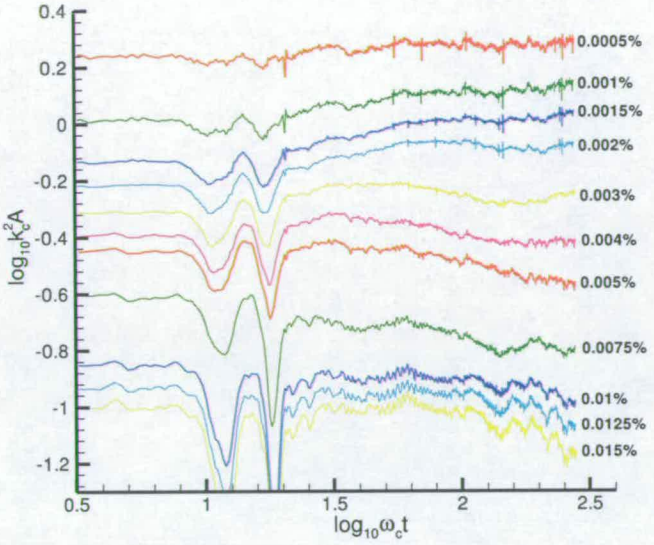

Figure 7.16: Area against time for second ak = 0.320 breaker (second example)

$$log_{10}k_c^2 A_{0.005\%} = -1.86 \times 10^{-1} log_{10}\omega_c t - 1.18 \times 10^{-1} \tag{7.42}$$

The difference between initial and final areas for this experiment is graphed in figure 7.17. The CCA appear to be around 0.005%

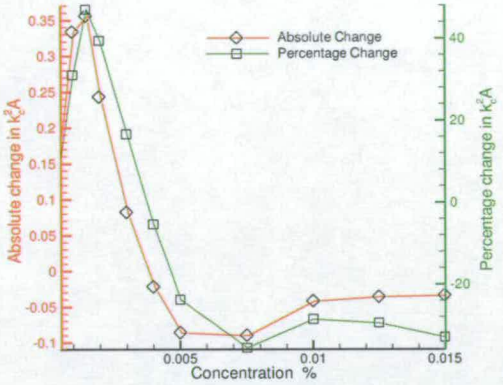

Figure 7.17: Change in $k_c^2 A$ against concentration for a second $ak = 0.320$ breaker (second example)

The next graph of results can be seen in figure 7.18

The lines show a larger spread in this graph that in the previous two, with most showing far less increase or decrease. The 0.004% plot has a gradient of only -2.86 $\times$ 10^{-2} between 4 seconds after breaking and the end of the experiment. Comparing this with the larger concentrations, between $log_{10}\omega_c t = 1.92$ and 2.29, the 0.0075% plot has a gradient of -1.88 $\times$ 10^{-1} before increasing in area after this period. The results for 0.01%, 0.0125% and 0.015% show similar trends over the same regions.

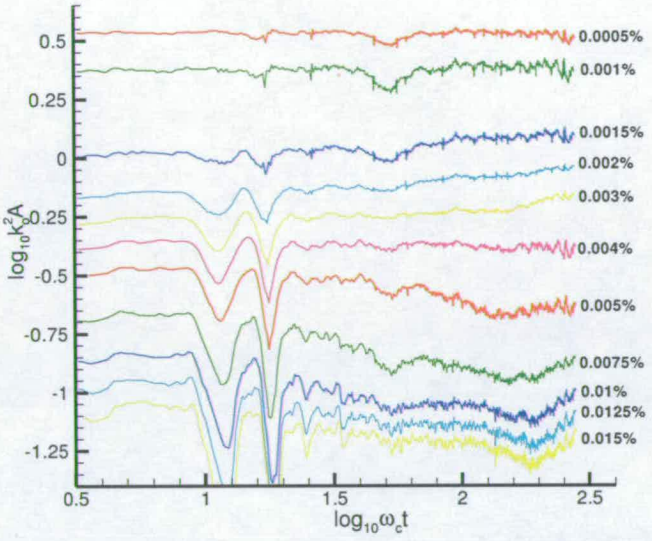

Figure 7.18: Area against time for second ak = 0.320 breaker (third example)

The lines start with a large spread and show, relative to the previous graph, smaller gradients, the resulting change in area over the experiment is plotted in figure 7.19.

The result for 0.0005% and 0.001% are not included as the high initial value suggestion they are already affected largely by the background dye levels. The CCA value appear to be around 0.004%.

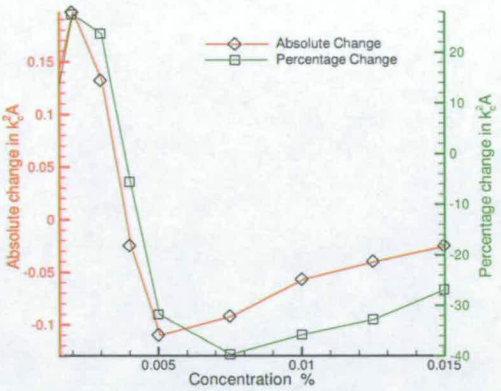

Figure 7.19: Change in k_c^2A against concentration for a second $ak = 0.320$ breaker (third example)

The fourth graph showing $log_{10}k_c^2A$ against $log_{10}\omega_c t$ for the given range of concentrations after a second $ak = 0.320$ breaker is presented in figure 7.20.

Again, the 0.0005% and 0.001% concentration areas appear to be largely affected by the background dye levels, as does the line for 0.0015%. As with the previous experimental result, there are large areas where the area appears to remain approximately constant. There is short period of increasing growth in the line for 0.003% concentration between $log_{10}\omega_c t = 1.74$ and 2.25 with the relationship

$$log_{10}k_c^2A_{0.003\%} = 1.60 \times 10^{-1} log_{10}\omega_c t - 4.90 \times 10^{-1} \tag{7.43}$$

Calculating the dispersion coefficient for the increasing area gives a relation-

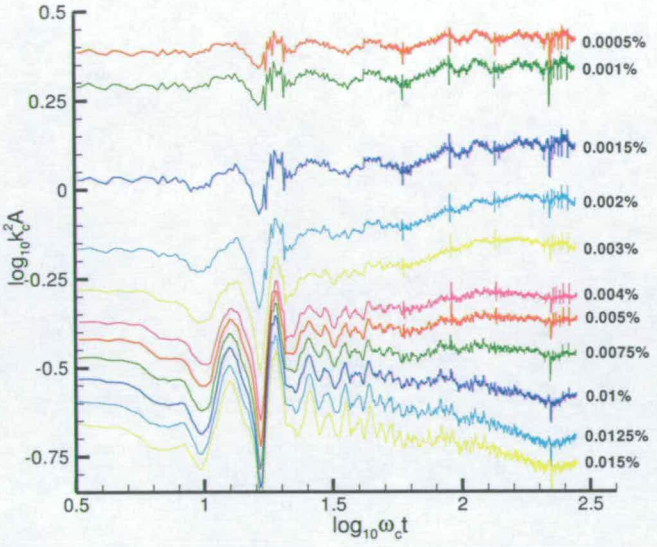

Figure 7.20: Area against time for second ak = 0.320 breaker (fourth example)

ship between area and time of;

$$A_{0.003\%} = \frac{(2 \times 4.33 \times 10^{-4} \omega_c t)^{0.160}}{k_c^2} \tag{7.44}$$

The measured area for the 0.004% concentration remains approximately constant, with a gradient of only -4.90 $\times$ 10^{-2} in the region $log_{10}\omega_c t = 2.04$ to the end of the experiment. Similar behaviour is shown by the 0.005% and 0.0075% concentrations. The large values show steadily decreasing area until $log_{10}\omega_c t = 2.35$ before increasing or remaining level. The gradient for the 0.015% concentration between $log_{10}\omega_c t$ and the end of the experiment is -1.53 $\times$ 10^{-1}.

A graph of the change in area over the course of the experiment is shown in figure 7.21. The CCA is much larger for this experiment, around 0.01%.

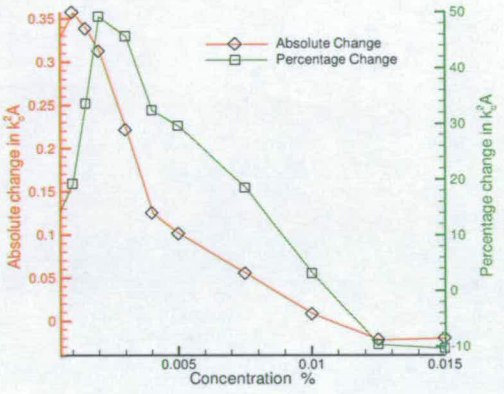

Figure 7.21: Change in k_c^2A against concentration for a second $ak = 0.320$ breaker (fourth example)

The final graph of results in this section is shown in figure 7.22. The concentrations 0.0005% to 0.002% are closely bunched together again and roughly level. Between $log_{10}\omega_c t = 1.44$ and the end of the experiment the line representing 0.002% has the relationship

$$log_{10}k_c^2A_{0.002\%} = 2.64 \times 10^{-2} log_{10}\omega_c t - 7.64 \times 10^{-2} \tag{7.45}$$

The concentration values 0.003% and 0.004% show decreases in area between $log_{10}\omega_c t = 1.52$ and 2.20 (6 to 29 seconds after breaking) before gradually increasing in area. Between $log_{10}\omega_c t = 1.52$ and 2.20, the gradient of the 0.004%

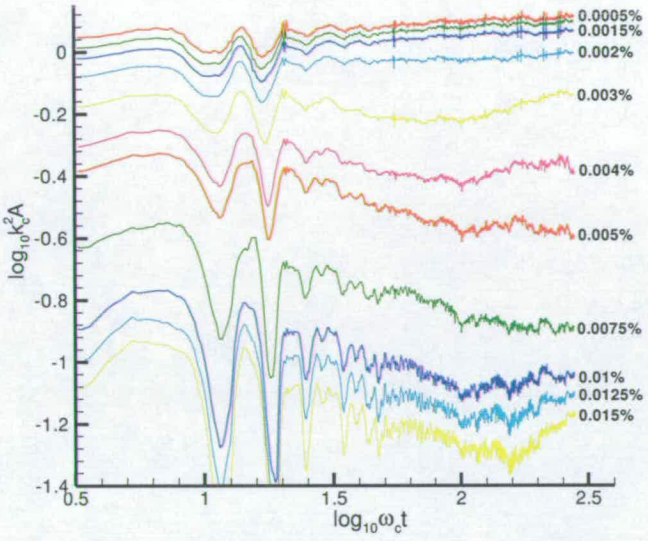

Figure 7.22: Area against time for second ak = 0.320 breaker (fifth example)

line is -1.28 × 10 $^{-1}$. The 0.005% area shows a similar decrease in this period, but remains approximately constant afterwards instead of increasing in area. The largest three concentrations, 0.01%, 0.0125% and 0.015% show decreasing area between $log_{10}\omega_c t$ = 1.6 and 2.2 before increasing again at the end of the experiment, by larger amounts for the larger concentrations.

The final plot of changing in area against concentration for a breaking wave with non-dimensional amplitude of 0.320 is shown in figure 7.23. The CCA value is approximately 0.003%.

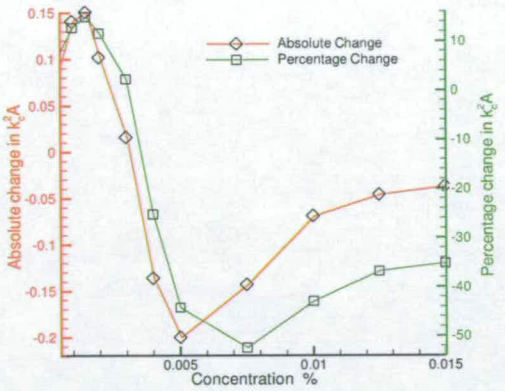

Figure 7.23: Change in $k_c^2 A$ against concentration for a second $ak = 0.320$ breaker (fifth example)

7.3.3 Area Results for Second $ak = 0.327$ Breaker

Figure 7.24 shows the area covered by the dispersing dye after a second $ak = 0.327$ breaking wave. Once again the lines representing the lowest four concentrations: 0.0005%, 0.001%, 0.0015% and 0.002%, appear level and are very similar. Between $log_{10}\omega_c t = 1.62$ and the end of the experiment, the 0.002% line had the following linear fit:

$$log_{10}k_c^2 A_{0.002\%} = 4.83 \times 10^{-2} log_{10}\omega_c t - 1.07 \times 10^{-1} \tag{7.46}$$

The 0.004%, 0.005% and 0.0075% concentrations also follow very similar patterns. Between approximately 18 and 40 seconds after breaking ($log_{10}\omega_c t = 1.99$ and 2.34) they all decrease in area with the following relationships:

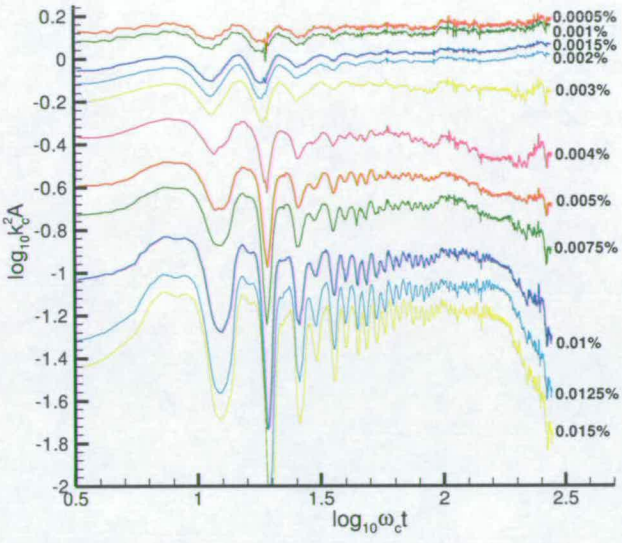

Figure 7.24: Area against time for second ak = 0.327 breaker (first example)

$$log_{10}k_c^2 A_{0.004\%} = -3.78 \times 10^{-1} log_{10}\omega_c t + 3.78 \times 10^{-1} \tag{7.47}$$

$$log_{10}k_c^2 A_{0.005\%} = -3.83 \times 10^{-1} log_{10}\omega_c t + 2.23 \times 10^{-1} \tag{7.48}$$

$$log_{10}k_c^2 A_{0.0075\%} = -4.98 \times 10^{-1} log_{10}\omega_c t + 3.56 \times 10^{-1} \tag{7.49}$$

At the end of the experiment the 0.004% concentration shows a slight increase in area whereas the 0.005% and 0.0075% concentrations both continue to decrease. The three largest concentrations, 0.01%, 0.0125% and 0.015%, maintain a constant area between $log_{10}\omega_c t = 1.92$ and 2.25 before decreasing rapidily

following this region. This rapid decrease could be due to dye leaving the lightsheet and will be discussed in section 7.3.4. The majority of the dye that leaves the lightsheet belongs to the larger concentrations, as can be seen in Appendix A, although this shows a single breaker with only a small amount of loss.

A graph of change between initial and final area is presented in figure 7.25.

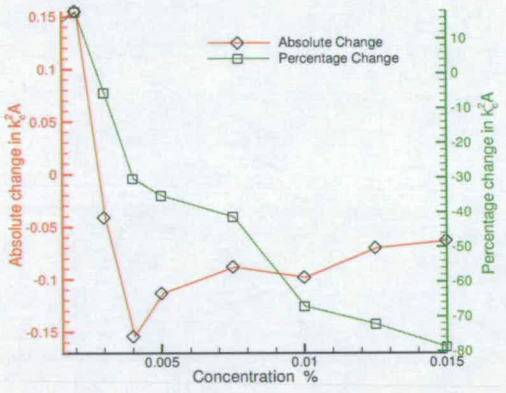

Figure 7.25: Change in k_c^2A against concentration for a second $ak = 0.327$ breaker (first example)

The next graph in this section is shown in figure 7.26. This graph is similar in many respects to the figure 7.24; the lower concentrations are close together on the graph, increasing gradually over the time of the experiment. The 0.005% area remains approximately constant throughout the experiment, but all values larger than this decrease in area.

Between 7 and 22 seconds after breaking many of the areas remain almost constant. The linear fits for the 0.003%, 0.004% and 0.0075% in this region and

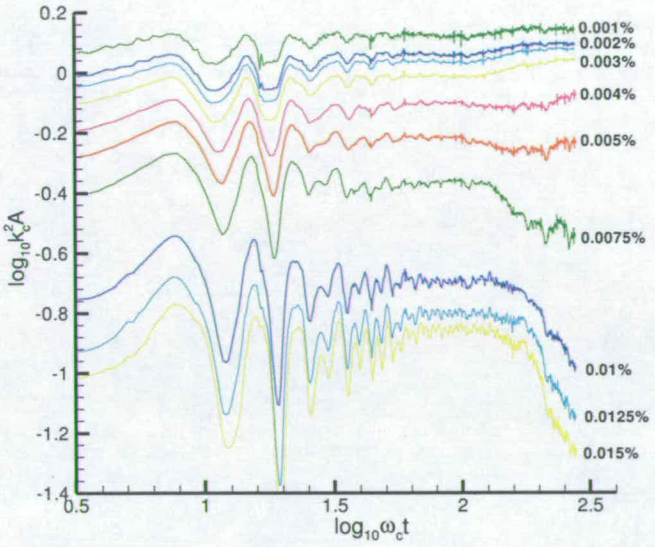

Figure 7.26: Area against time for second ak = 0.327 breaker(second example)

0.015% (between 10 and 22 seconds), are:

$$log_{10}k_c^2 A_{0.003\%} = 1.26 \times 10^{-2} log_{10}\omega_c t - 3.93 \times 10^{-2} \tag{7.50}$$

$$log_{10}k_c^2 A_{0.004\%} = 1.65 \times 10^{-2} log_{10}\omega_c t - 1.39 \times 10^{-1} \tag{7.51}$$

$$log_{10}k_c^2 A_{0.0075\%} = 3.36 \times 10^{-2} log_{10}\omega_c t - 4.35 \times 10^{-1} \tag{7.52}$$

$$log_{10}k_c^2 A_{0.015\%} = 6.41 \times 10^{-2} log_{10}\omega_c t - 9.88 \times 10^{-1} \tag{7.53}$$

This could well imply that during this region the dispersion effects of the second breaking wave are not having a large effect on total areas covered by these

concentrations and the gradually, far slower, processes of molecular diffusion are actually more important.

The relationships between area and time for the 0.003%, 0.004% and 0.015% concentrations between 22 seconds after breaking and the end of the experiment, and the 0.0075% concentrations between 22 and 37 seconds after breaking are shown below:

$$log_{10}k_c^2 A_{0.003\%} = 1.46 \times 10^{-1} log_{10}\omega_c t - 3.11 \times 10^{-1} \tag{7.54}$$

$$log_{10}k_c^2 A_{0.004\%} = 1.16 \times 10^{-1} log_{10}\omega_c t - 3.70 \times 10^{-1} \tag{7.55}$$

$$log_{10}k_c^2 A_{0.0075\%} = -7.19 \times 10^{-1} log_{10}\omega_c t - 1.13 \tag{7.56}$$

$$log_{10}k_c^2 A_{0.015\%} = -1.40 log_{10}\omega_c t + 2.17 \tag{7.57}$$

By examining the images taken during the experiment it is possible to see that the sudden decrease in area for the larger concentrations is caused by dye which was higher than the 0.02% limit dispersing into lower concentrations.

The difference between initial and final areas for each of the concentrations is plotted in figure 7.27.

The 0.005% line appears closest to the CCA value.

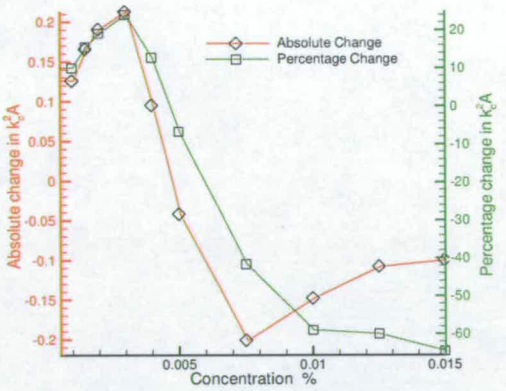

Figure 7.27: Change in k_c^2A against concentration for a second $ak = 0.327$ breaker (second example)

Figure 7.28 is the third graph of area, for each concentration, as a function of time beneath a second $ak = 0.327$ breaking wave. The lowest three concentrations have very similar lines with the plot for 0.002%, although at a higher area. Between $log_{10}\omega_c t = 1.62$ and the end of the experiment this concentration has the linear fit:

$$log_{10}k_c^2A_{0.002\%} = 7.21 \times 10^{-2} log_{10}\omega_c t - 1.41 \times 10^{-2} \tag{7.58}$$

The 0.004% concentration shows a region of almost contant area between 7 and 32 seconds after breaking (with a gradient of 7.37×10^{-3}) followed by a steady decrease in area with a gradient of -2.95×10^{-1}. Over the same two regions, the lines representing 0.005% and 0.01% concentrations show the follow-

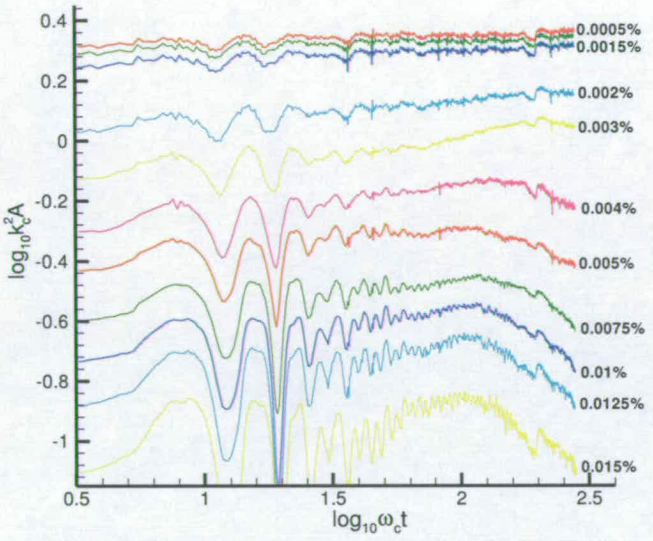

Figure 7.28: Area against time for second ak = 0.327 breaker (third example)

ing relationships, starting with 7 to 32 seconds (7 to 22 seconds for 0.01%) after breaking:

$$log_{10}k_c^2 A_{0.005\%} = -2.70 \times 10^{-2} log_{10}\omega_c t - 2.54 \times 10^{-1} \tag{7.59}$$

$$log_{10}k_c^2 A_{0.01\%} = 1.16 \times 10^{-1} log_{10}\omega_c t - 7.90 \times 10^{-1} \tag{7.60}$$

Following this period,

$$log_{10}k_c^2A_{0.005\%} = -3.39 \times 10^{-1} log_{10}\omega_c t + 4.17 \times 10^{-1} \tag{7.61}$$

$$log_{10}k_c^2A_{0.01\%} = -5.40 \times 10^{-1} log_{10}\omega_c t + 5.82 \times 10^{-1} \tag{7.62}$$

Figure 7.29 shows the change in area over the experiment.

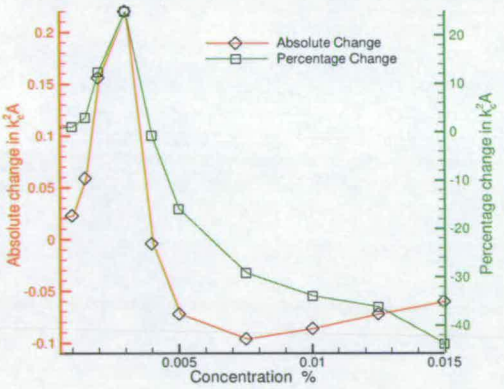

Figure 7.29: Change in k_c^2A against concentration for a second $ak = 0.327$ breaker (third example)

The 0.003% concentration appears closest to the CCA value.

The last area graph is presented as figure 7.30. As with previous area graphs, the lower concentrations are bunched together at the larger areas and have very small gradients throughout the experiment. The 0.002% line has a linear fit of:

$$log_{10}k_c^2A_{0.002\%} = 4.47 \times 10^{-2} log_{10}\omega_c t - 2.61 \times 10^{-1} \tag{7.63}$$

in the region from $log_{10}\omega_c t = 1.64$ to the end of the experiment.

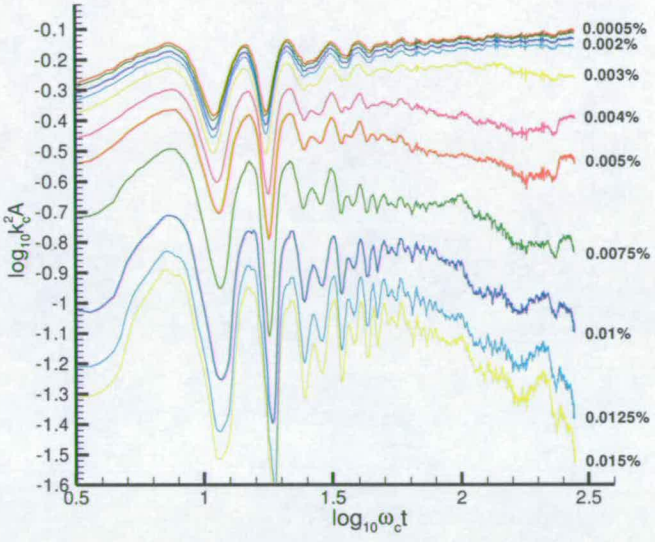

Figure 7.30: Area against time for second ak = 0.327 breaker (fourth example)

The plot for 0.004% has two clear periods of changing area, between $log_{10}\omega_c t = 1.64$ and 2.29, and 2.29 and the end of the experiment. The relationships in these regions are

$$log_{10}k_c^2 A_{0.004\%} = -1.72 \times 10^{-1} log_{10}\omega_c t_{1.64-2.29} - 4.77 \times 10^{-2} \tag{7.64}$$

$$log_{10}k_c^2 A_{0.004\%} = 3.47 \times 10^{-1} log_{10}\omega_c t_{2.29-2.44} - 1.23 \tag{7.65}$$

The largest concentrations show continual decreases in area following the sec-

ond breaker. The final graph of change in area over the course of the experiment for each of the concentrations is shown in figure 7.31.

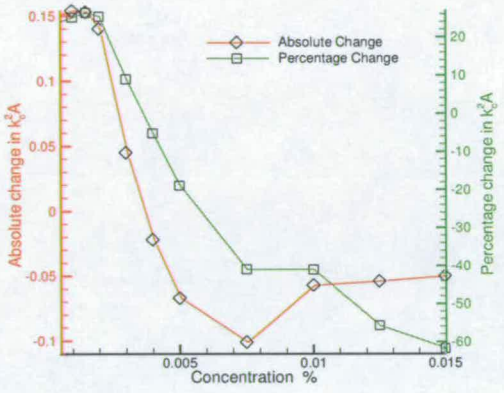

Figure 7.31: Change in k_c^2A against concentration for a second $ak = 0.327$ breaker (fourth example)

The area of concentration level 0.003% remains approximately constant.

7.3.4 2D Mass After Second Breaker

As with the single breaker area results it is important to look at the dye entering or leaving the lightsheet during the experiment.

A sample result from an $ak = 0.314$ breaker is presented in figure 7.32. The 0^{th} moment is calculated using equation 5.2. The initial sharp peaks are caused by the water's surface dropping below the MWL and producing a large number of false high concentration readings. Following this, the value remains approximately

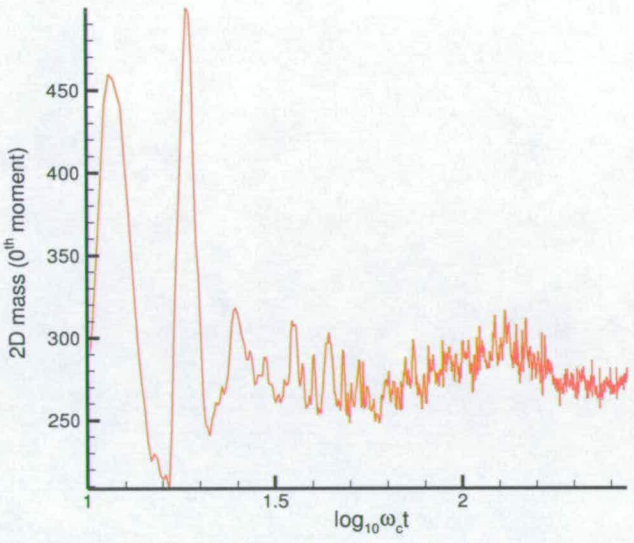

Figure 7.32: 2D mass against time for second ak = 0.314 breaker

level, implying that there is very small net out of plane motion.

The result for the next size of breaking wave, $ak = 0.320$, shown in figure 7.33, is qualatatively similar to figure 7.32 although the actual values for the mass are higher.

There is a slight decrease in mass over the course of the experiment. This could be due to three factors. Any dye leaving the lightsheet will lower the 0^{th} moment, and dye entering the lightsheet will cause it to rise. As the net out-of-plane motion should be very small, this should have no effect on larger timescales. Two other possible reasons for underestimation or reduction are the lowest concentrations passing below measureable levels, or else being excluded as

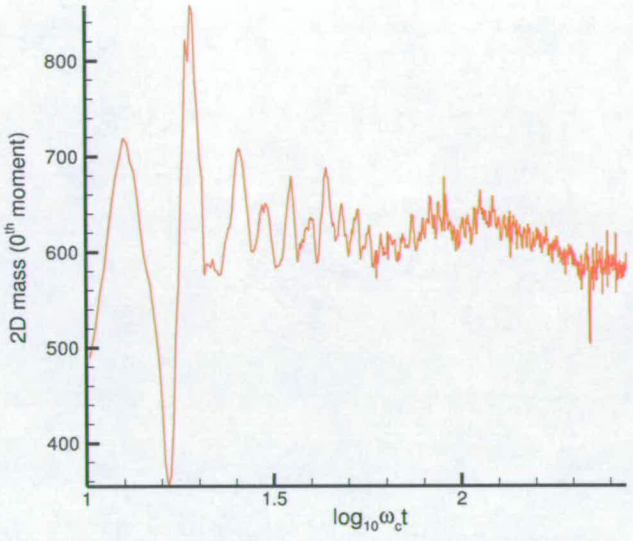

Figure 7.33: 2D mass against time for second ak = 0.320 breaker

background, and concentration higher than 0.02% being measured as 0.02%, and therefore underestimated.

The final 2D mass graph, figure 7.34 shows a sample result for a second $ak = 0.327$ breaker.

In this graph the surface fluctations take slightly longer to die out before a gradual decrease in mass is seen. Examination of the images from the experiment suggests that the second of the three possible causes, concentration dropping below measureable level, is responsible for this decrease.

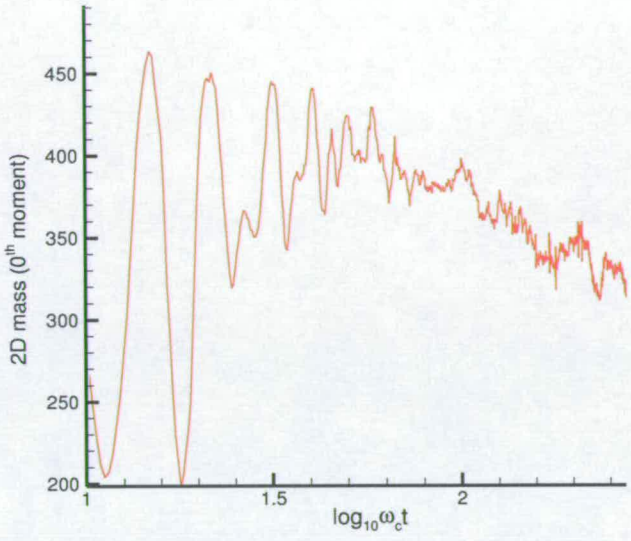

Figure 7.34: 2D mass against time for second ak = 0.327 breaker

Also of interest is the change in mass between the end of the first breaker and the end of the second breaker. Table 7.3 shows the initial and final 2D mass values and difference between the two.

This provides a test of how consistent the tracking of concentration is for that experiment and provides evidence of areas of experimental practice that may need to be improved in future work.

In can be seen that larger breaking waves tend to result in lowering of the mass during the experiment, in a similar manner to the single breakers. This means that future experiments should include greater ranges of concentrations and larger areas of measurement to counteract this effect.

ak value	Initial 2D Mass	Final 2D Mass	Difference
0.314	282.4	328.1	45.7 (+16.2%)
0.314	259.8	275.1	15.3 (+5.9%)
0.320	501.4	529.1	27.7 (+5.5%)
0.320	478.9	476.6	-2.3 (-0.5%)
0.320	428.5	418.8	-9.7 (-2.3%)
0.320	541.4	598.4	-57 (-10.5%)
0.320	546.8	475.5	-71.3 (-15%)
0.327	476.4	388.4	-88 (-18.5%)
0.327	682.8	600.2	-82.6 (-12.1%)
0.327	598.9	560.4	-38.5 (-6.4%)
0.327	374.0	313.3	-60.7 (-16.2%)

Table 7.3: Effect of second breaker on 2D mass

7.3.5 Area Results for Second Breaker Summary

The effect of a second breaking wave on the area of the dispersing dye is obviously very important. The results show that a second breaking wave increases the area covered by the lower concentrations but decreases the area covered by the larger concentrations. For the smallest breaking wave, with an ak value of 0.314, this boundary was around 0.0075%; any concentration below this value increased in size. This value was inversely related to the wave amplitude, and the largest breakers reduced the area of concentrations greater than 0.004%.

The greatest percentage increases in lower concentration area were actually produced by the smallest breaking waves, implying that whilst larger breaks cause the lower concentrations to reach greater depths, they produce smaller areas, relatively.

7.3.6 Comparison Between Single and Double Breaking Wave Area Results

The single breaking wave results showed that larger breaking waves reduced the area covered by the higher concentrations, with the transition from spilling to breaking again being a very important point. This general trend is continued by the second breaking wave experiments, where results show that a second breaking wave also decreases the area covered by higher concentrations. As it was not possible to obtain results for plunging breaking waves, the effect of the transition point between spilling and plunging could not be examined.

7.4 Centre of Mass Results for Second Breaker

The centre of mass was also measured for the second breaking wave experiments in the same manner as the previous chapter. The results are presented with separate x and y coordinates as explained in section 6.5.

7.4.1 Centre of Mass Results for Second $ak = 0.314$ Breaker

Figure 7.35 shows the centre of mass motion following a second $ak = 0.314$ breaking wave. Unlike the results for the single breaking wave, the initial values are not zero. This is because the first breaking wave has already disturbed the centre

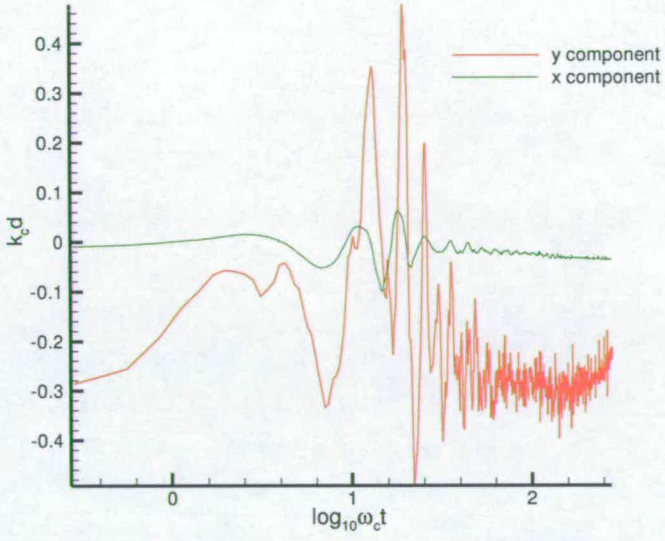

Figure 7.35: Centre of mass against time for second ak = 0.314 breaker

of mass from the origin position. The sharp peaks and troughs around $log_{10}\omega_c t = 1$ are caused by the breaking wave.

The x component, representing depth, remains approximately constant following breaking, decreasing slightly with the relationship

$$k_c d_x = -2.59 \times 10^{-2} log_{10}\omega_c t + 2.26 \times 10^{-2} \tag{7.66}$$

As with the result for the single $ak = 0.314$ breaker, the centre of mass moves against the wave direction, ending upstream of the origin position.

The change in centre of mass position caused by the second breaking wave is

discussed at the end of the section.

7.4.2 Centre of Mass Results for Second $ak = 0.320$ Breaker

Four sample results for the centre of mass motion after a second $ak = 0.320$ are presented in this section. The first graph is shown in figure 7.36.

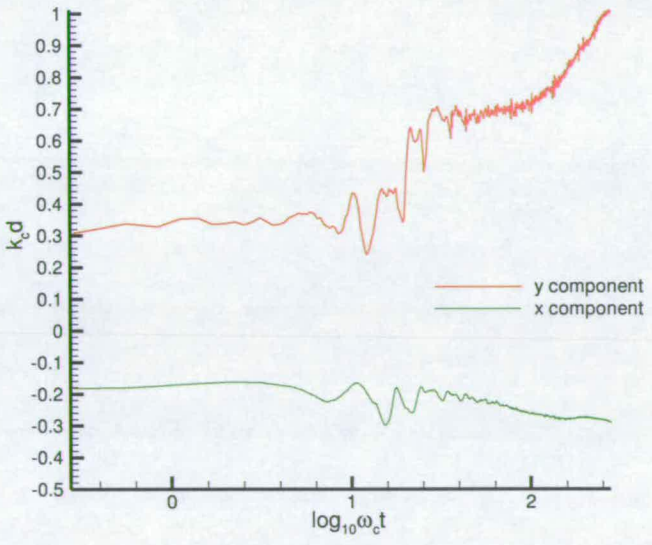

Figure 7.36: Centre of mass against time for second ak = 0.320 breaker (first example)

The depth component,x shows a steady decrease between $log_{10}\omega_c t = 1.2$ and the end of the experiment with a gradient of -8.11 $\times$ 10^{-2}. The y component shows a period of slow movement downstream between $log_{10}\omega_c t = 1.1$ and 1.6 followed by a region of increased movement until the end of the experiment. The relationship between position and time in these regions are:

$$k_c d_{log_{10}\omega_c t=1.1-1.6} = 1.47 \times 10^{-1} log_{10}\omega_c t + 4.28 \times 10^{-1} \tag{7.67}$$

$$k_c d_{log_{10}\omega_c t=1.6-end} = 7.92 \times 10^{-1} log_{10}\omega_c t - 9.17 \times 10^{-1} \tag{7.68}$$

A very similar trend is shown in the graph presented in figure 7.37, also for a second $ak = 0.320$ breaker.

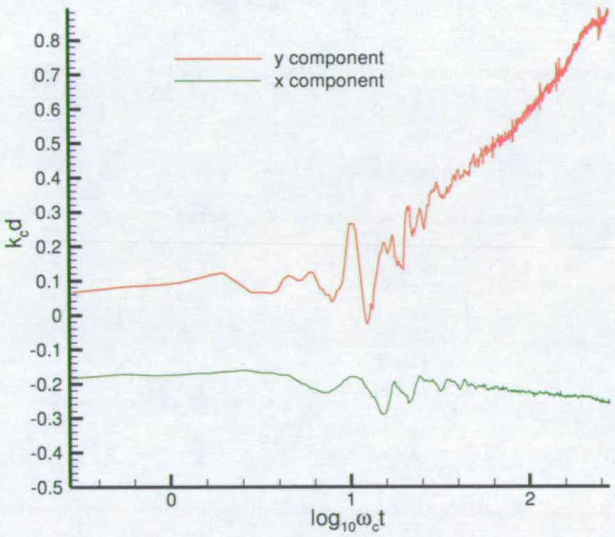

Figure 7.37: Centre of mass against time for second ak = 0.320 breaker (second example)

Once again, the depth increases steadily following the second breaking wave. The downstream movement of the centre of mass is more uniform for this experiment, increasing with the relationship:

$$k_c d_y = 5.58 \times 10^{-1} log_{10}\omega_c t - 5.53 \times 10^{-1} \tag{7.69}$$

between $log_{10}\omega_c t$ equals 1.2 and the end of the experiment.

The third graph in this section, figure 7.38, shows a sharper rise in the y component, although the final values are very similar.

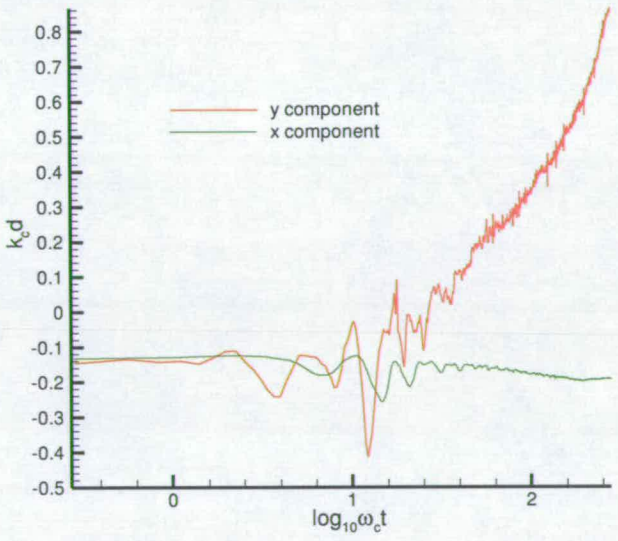

Figure 7.38: Centre of mass against time for second ak = 0.320 breaker (third example)

The gradient of this line between $log_{10}\omega_c t = 1.4$ and the end of the experiment is 8.33×10^{-1}. The depth increases over the course of the experiment with the relationship:

$$k_c d_x = -5.03 \times 10^{-2} log_{10}\omega_c t - 7.82 \times 10^{-2} \tag{7.70}$$

The final graph representing the centre of mass motion after a second $ak = 0.320$ breaker is presented in figure 7.39.

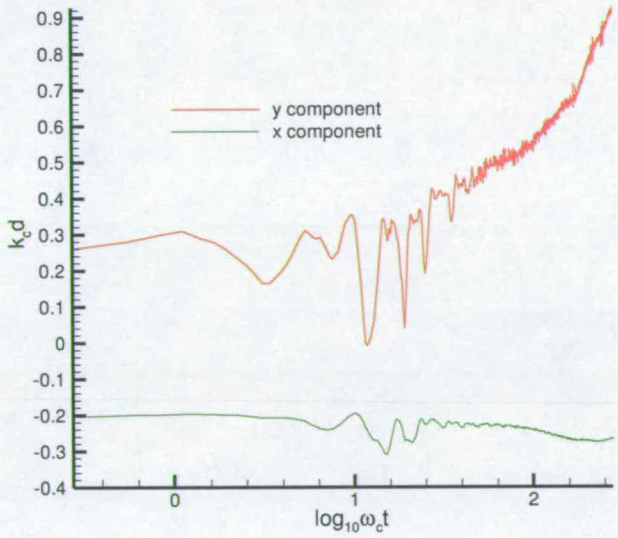

Figure 7.39: Centre of mass against time for second ak = 0.320 breaker (fourth example)

The graph is very similar to figure 7.36, with the depth increasing slowly whilst the downstream motion shows two regions with different speeds. Between $log_{10}\omega_c t = 1.2$ and the end of the experiment the depth component has the following linear approximation:

$$k_c d_x = -5.43 \times 10^{-2} log_{10}\omega_c t - 1.44 \times 10^{-1} \tag{7.71}$$

The y component of the centre of mass has the linear approximations:

$$k_c d_{ylog_{10}\omega_c t=1.4-2} = 3.24 \times 10^{-1} log_{10}\omega_c t - 8.86 \times 10^{-2} \tag{7.72}$$

$$k_c d_{ylog_{10}\omega_c t=2-end} = 1.15 log_{10}\omega_c t - 1.89 \tag{7.73}$$

7.4.3 Centre of Mass Results for Second $ak = 0.327$ Breaker

Four results are also presented for the centre of mass motion following a second $ak = 0.327$ breaking wave. The first is shown in figure 7.40.

Qualitatively the graph appears very similar to the results in the previous section. However, the y component of the centre of mass reaches a far greater distance downsteam than in the $ak = 0.320$ examples. The linear approximation for the y component between $log_{10}\omega_c t$ equals 1.2 and 2 is given by

$$k_c d_y = 7.21 \times 10^{-1} log_{10}\omega_c t - 2.17 \times 10^{-1} \tag{7.74}$$

After $log_{10}\omega_c t$ the plot levels out until the end of the recording.

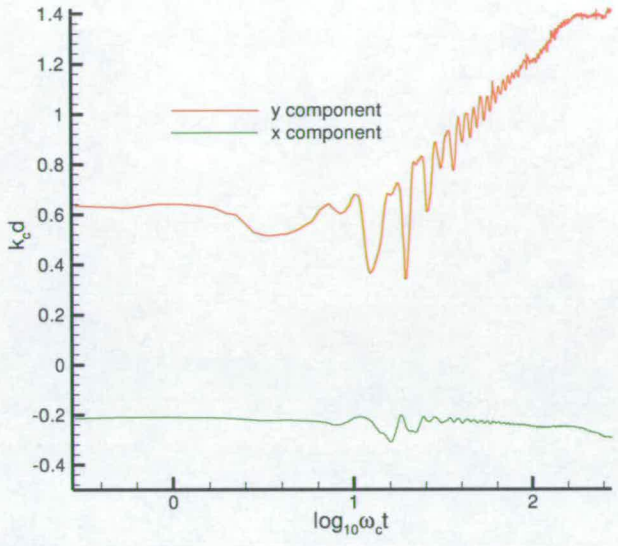

Figure 7.40: Centre of mass against time for second ak = 0.327 breaker (first example)

The depth increases with a gradient of -7.16 $\times$ 10^{-2} between $log_{10}\omega_c t = 1.4$ and the end of the experiment.

Figure 7.41 presents another example of the centre of mass motion of the dye following a second $ak = 0.327$ breaker.

This graph shows very similar centre of mass motion to the previous result. The relationships between $k_c d$ and time for both x and y components are shown in equations 7.75 and 7.76, for $log_{10}\omega_c t = 1.4$ to the end of the experiment.

$$k_c d_x = -1.50 \times 10^{-1} log_{10}\omega_c t + 2.45 \times 10^{-2} \tag{7.75}$$

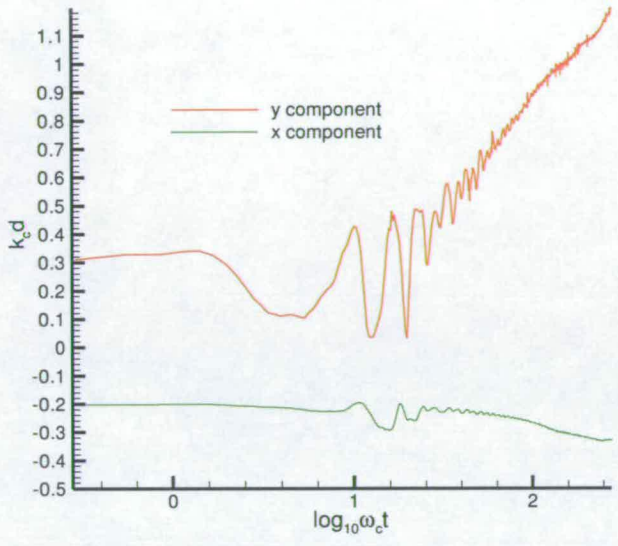

Figure 7.41: Centre of mass against time for second ak = 0.327 breaker (second example)

$$k_c d_y = 6.98 \times 10^{-1} log_{10}\omega_c t - 5.24 \times 10^{-1} \tag{7.76}$$

The third graph in this section, figure 7.42, is very similar to figure 7.41. The initial value for the y component is larger than in the previous two results, and therefore the final value is also much larger. The relative increase in downstream position of the centre of mass will be discussed in section 7.4.4 . The depth also starts at a lower value than the previous results for an $ak = 0.327$ breaker.

A steady period of linear increase can be identified between $log_{10}\omega_c t = 1.4$ and the end of the experiment for both x and y components. The relationships

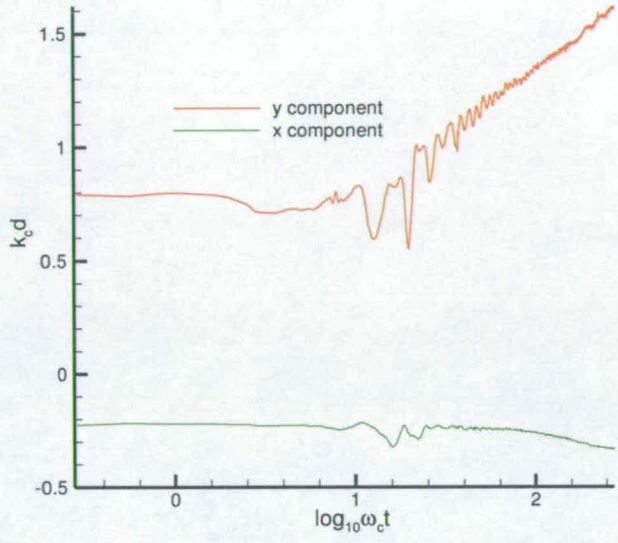

Figure 7.42: Centre of mass against time for second ak = 0.327 breaker (third example)

in this region are given by:

$$k_c d_x = -1.24 \times 10^{-1} log_{10}\omega_c t - 2.57 \times 10^{-2} \tag{7.77}$$

$$k_c d_y = 5.91 \times 10^{-1} log_{10}\omega_c t + 1.64 \times 10^{-1} \tag{7.78}$$

The final centre of mass graph is presented in figure 7.43.

Once again, a period of steady growth $log_{10}\omega_c t = 1.4$ and the end of the experiment can be identified. During this time, the linear approximations are

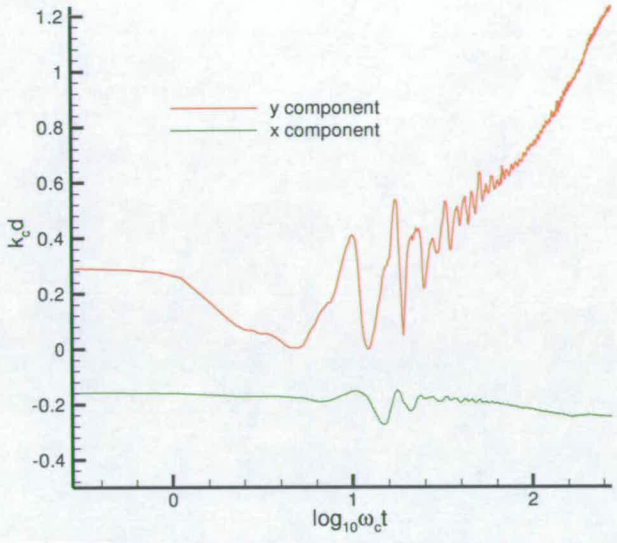

Figure 7.43: Centre of mass against time for second ak = 0.327 breaker (fourth example)

$$k_c d_x = -7.63 \times 10^{-2} log_{10}\omega_c t - 6.79 \times 10^{-2} \tag{7.79}$$

$$k_c d_y = 9.04 \times 10^{-1} log_{10}\omega_c t - 1.02 \tag{7.80}$$

7.4.4 Centre of Mass Results Summary

The results for the three different breaker amplitude presented here show the different nature of the centre of mass motion. The smallest breaking wave, with a non-dimensional amplitude of 0.314, resulted in the centre of mass actually

moving upstream of initial position whereas the next two larger breakers, 0.320 and 0.327, both show movement downstream with $k_c d$ values of ranging between approximately 1 and 1.5.

As mentioned previously, of obvious importance is the change in centre of mass position caused by the second breaker. The clearest way to do this is to compare the initial and final values of each component for the presented graphs. These are shown in tables 7.4 and 7.5.

ak value (fig#)	Initial x ($k_c d$)	Final x ($k_c d$)	Difference
0.314	-0.009	-0.036	-.027(-300%)
0.320 (7.36)	-0.183	-0.291	-0.108(-59%)
0.320 (7.37)	-0.184	-0.259	-0.075(-41%)
0.320 (7.38)	-0.133	-0.193	-0.060(-45%)
0.320 (7.39)	-0.205	-0.267	-0.062(-23%)
0.327 (7.40)	-0.215	-0.294	-0.079(-37%)
0.327 (7.41)	-0.204	-0.330	-0.126(-62%)
0.327 (7.42)	-0.225	-0.333	-0.108(-48%)
0.327 (7.43)	-0.159	-0.247	-0.088(-55%)

Table 7.4: Change in x coordinate of centre of mass

The small initial x value of the $ak = 0.314$ breaker makes the final result difficult to interpret but it is possible to calculate average percentage increases in depth for the other two amplitudes. The $ak = 0.320$ breakers show a average depth increase of 42% and the $ak = 0.327$ breakers 50.5%. Although the sample size is small, and further results should be taken, this definately implies that larger breakers will cause a greater increase in the average depth of the film after dispersion.

The change in downstream position for the centre of mass is shown in table 7.5.

ak value (fig#)	Initial y ($k_c d$)	Final y ($k_c d$)	Difference
0.314	-0.286	-0.223	-.063(-28%)
0.320 (7.36)	0.307	1.010	0.703(229%)
0.320 (7.37)	0.066	0.874	0.808(1224%)
0.320 (7.38)	-0.146	0.863	1.009(-)
0.320 (7.39)	0.261	0.927	0.666(255%)
0.327 (7.40)	0.636	1.412	0.776(122%)
0.327 (7.41)	0.311	1.194	0.883(284%)
0.327 (7.42)	0.794	1.609	0.815(103%)
0.327 (7.43)	0.293	1.233	0.940(321%)

Table 7.5: Change in y coordinate of centre of mass

In this case it is more meaningful to compare the absolute, rather than percentage, differences. The average absolute difference for the breakers with non-dimensional amplitudes of 0.320, is 0.797. For breakers with non-dimensional amplitudes of 0.327, it is 0.854. The larger breaker size implies a greater increase in centre of mass motion downstream of the breaking point.

Further results would have to be taken for a range of breaking waves with amplitudes between 0.314 and 0.327 to provide more accurate data, although the initial indications show a relationship between breaker size and increased centre of mass motion.

7.4.5 Comparison Between Single and Double Breaking Wave Centre of Mass Results

The single breaking wave results showed a very clear link between breaker amplitude and centre of mass position, as shown in figure 6.31. The limited range of second breaker results make a comparison with this result difficult. The second breaker results show that centre of mass depth is approximately doubled by the $ak = 0.327$ breaking wave, and increased by 40% by the $ak = 0.320$ breaking wave. This shows that further breaking waves do cause greater movement in the centre of mass.

7.5 Dispersion Results for Second Breaker

The dispersion was calculated is the same manner as the single breaking wave experiments in section 6.6. Plots of $log_{10}\sigma_x k_c$ and $log_{10}\sigma_y k_c$ against $log_{10}\omega_c t$ are shown in figure 7.44.

The horizontal standard deviation, shown in the left figure, starts at a very small value. This fits closely with the final value from the single breaker experiment in figure 6.32. After the disturbance caused by the second breaking wave the coefficent decreases further in a similar manner to the single breaking wave experiments.

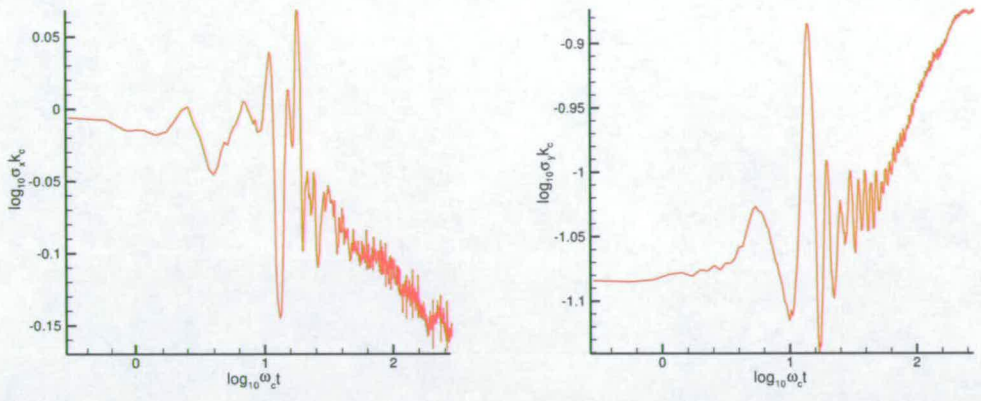

(a) (b)

Figure 7.44: (a)X and (b) Y standard deviation for a second $ak = 0.320$ breaker

The vertical standard deviations, shown in the right figure, is also very similar to the graph presented in figure 6.32. Following the second breaking wave the standard deviation increases as the vertical spread of the dye becomes larger, confirming the previous depth and area results.

As with the results presented in Chapter 6, the horizontal and vertical standard deviations show no direct amplitude dependance, even though such a dependance is found in the depth and area results. The plots are very similar in form to those for the single breaking waves.

7.6 Fractal Dimension Results for Second Breaker

The final quantity measured was the fractal dimension. As discussed in section 6.7, the calculation for the box counting dimension is sensitive to the value of the

threshold used for analysis. As with section 6.7 the threshold for each experiment was set by carefully examining each image to decide on the background levels.

Figures 7.45 to 7.47 show the box counting dimensions of the dispersion caused by each of the three amplitudes used for the second breaker experiments.

Unlike the single breaking wave results the box counting dimension for the second breaking wave experiments doesn't start at 1, as the initial wave has already started the dispersion.

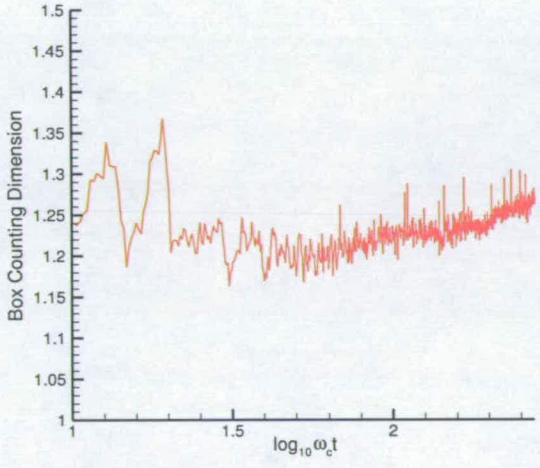

Figure 7.45: Box counting dimension of outline of dispersion caused by a second ak = 0.314 breaker

For the $ak = 0.314$ result, shown in figure 7.45, the fractal dimension grows steadily between $log_{10}\omega_c t = 1.5$ and the end of the experiment, reaching a final value of approximately 1.25. This is almost identical to the result for a single breaking wave presented in figure 6.35.

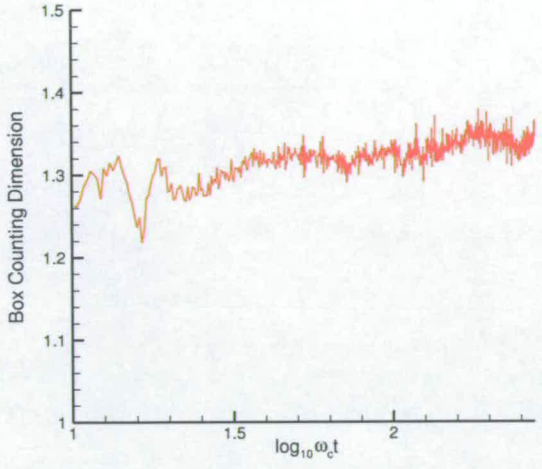

Figure 7.46: Box counting dimension of outline of dispersion caused by a second ak = 0.320 breaker

The next graph, figure 7.46, shows the calculated box counting dimension of the outline of the dispersing dye after a second $ak = 0.320$ breaker. The fractal dimension remains almost constant around 1.3, raising only slightly as the experiment continues. This is larger than the single breaker result, but nearer to the results of Schlicke [67] for a similar sized breaking wave.

The final graph is shown in figure 7.47 and represent the box counting dimension measured after a second breaking wave with a non-dimensional amplitude of 0.327. As mentioned previously this was the largest breaking wave that could be used for the two breaker experiments without significant amounts of dye leaving the lightsheet downstream of the recording area.

After the initial peaks and troughs caused by the breaking wave the box

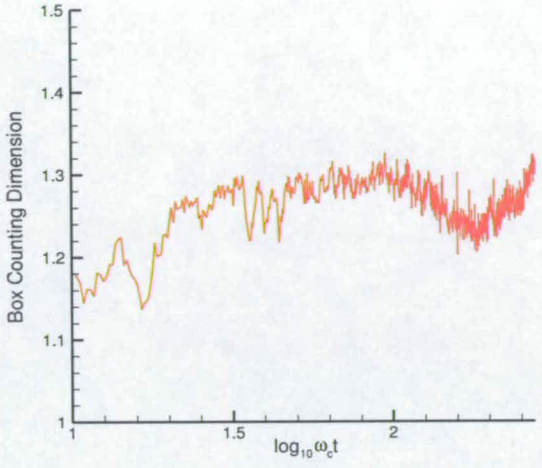

Figure 7.47: Box counting dimension of outline of dispersion caused by a second ak = 0.327 breaker

counting dimension levels off at around 1.3 between $log_{10}\omega_c t = 1.5$ and 2. Between $log_{10}\omega_c t = 2$ and 2.3 it decreases slightly before returning to around 1.3 at the end of the experiment.

As suggested by the larger amplitudes in the single breaking wave experiments, the extra energy provided by an extra breaking wave in this case does allow the mixing to reach the levels required to produce a more complex outline. However, the similarity of the box counting values for both the $ak = 0.320$ and 0.327 breaking waves again suggests that there is a natural limit that cannot be increased upon. The fractal dimension remains approximately constant for all amplitudes, implying the second breaker does does not significantly alter the process of mixing.

7.7 Double Breaker Conclusions

In this chapter the effect of a second breaking wave on the dispersion process was examined for three different non-dimensional breaking wave amplitudes, 0.314, 0.320 and 0.327.

The first results presented were on the maximum depth reached by a range of concentration values following the second breaking wave. The results showed that the second breaking wave increased the depths reached by all concentrations. Further investigation is required to discover how much of this is due to the second breaking wave and how much is due simply to a long time scale. Periods of almost constant maximum depth for the larger concentrations implied that the mixing caused by the second breaking wave in some cases did not affect the dye at that depth for the majority of the time of the experiment.

The next section looked at the area covered by the dispersing dye. For the smallest breaking wave, with an ak value of 0.314, it was shown that the second breaking wave increased the area covered by the smaller concentrations by around 50% but reduced the area of the largest concentration by between 25 and 30%. Concentrations around 0.005% remained approximately the same in area after the second breaker. As the breaker size increased, the percentage increase in size of the small concentrations decreased and the concentration level remaining constant also decreased.

It was shown that larger breaking waves will caused a greater movement of the film as a whole, moving further downstream and to a greater depth. The small range of breaker amplitudes limits the conclusions that can be drawn, but early indications have shown potential for further investigation would be worthwhile.

As with the single breaking wave results, the standard deviation of the film showed no dependance on breaking wave amplitude although the box-counting dimension increased for the larger two breaking wave amplitudes.

Combining the results obtained for all five measurement provides an initial understanding of the movement of the dispersing dye after a second breaking wave.

Chapter 8

Conclusions and Further Work

8.1 Review of Subject

Surface films are present in many places around the world, whether caused naturally or man-made. They affect the environment both as pollutants and by damping capillary waves and therefore potentially inhibits gravity wave production. These films will spread on the water's surface, but due to their surfactant nature, will not readily mix beneath the surface.

One of the main causes of dispersing surface films are breaking waves. As waves grow, they becoming increasing non-linear with steeper crests. These crests eventually break and entrain air and surface water beneath them. When this breaking occurs where a surface film is present, the film is broken up and carried

under the surface.

The purpose of this research was to investigate this mixing for both isolated breaking waves, and pairs of breaking waves, over a range of amplitudes. The surface film was created using a methanol/rhodamine solution, which was an adequate approximation to a surfactant. The film was spread evenly on the surface and then broken by a breaking wave of known amplitude. The subsequent dispersion was then recorded either immediately or following a second breaking wave of identical amplitude.

8.2 Experimental Technique

The technique of Planer Laser Induced Fluorescence was used for all experiments. A plane of laser light, created by a Scanning Beam Box, was created in the middle of the wave tank equidistant from each wall. The fluorescence of the illuminated dye was recorded on two CCD cameras at 20 frames per second for approximately one minute following either the first or second breaker.

These images were then computationally prepared for analysis by removing the effects of variation in lightsheet intensity, calibration with known concentrations and joining into a single image. Each experiment produced 1000 such images.

These images were then processed using custom software. The measured

parameters for both single and double breaking wave experiments were:

- Depth reached as a function of concentration and amplitude
- Area covered as a function of concentration and amplitude
- Centre of mass motion as a function of amplitude
- Dispersion coefficents and exponents
- Fractal dimension of dye-water interface

A comparison was also made between the single and double breaking wave results to determine the effect of a second breaking wave.

8.3 Summary of Results

8.3.1 Maximum Depth

The single breaking wave results showed a clear link between breaking wave amplitude and the maximum depth reached by the lower concentrations, around 0.001% to 0.005%. This was because the large energy involved in larger breaking waves provided more eddies and turbulence to carry the dye to greater depths.

For the larger concentrations, 0.01% to 0.015% and above, the trend was rather different. The depth reached grew with increasing spilling breaker size,

but began to decrease once the transition to plunging had occured, around an ak amplitude of 0.330. This was because the larger breaking waves now caused the higher concentrations to be dispersed, instead of simply carried to greater depths.

This is a significant discovery as it shows that milder sea conditions may pose the greatest threat to organisms living near the water's surface.

The second breaking wave results showed that further breaking waves may not directly affect the maximum depths reached by larger concentrations initially and simply provide further energy to continue the process of dispersion.

8.3.2 Area

The single breaking wave results showed a similar dependance on the type of breaking wave for higher concentrations. The largest spilling breakers were responsible for the greatest areas of higher concentrations, whilst the plunging breakers were responsible for a decrease in area for 0.001% and above.

The smallest concentrations were dispersed to greater areas proportionally to the breaker size.

The area covered by the dye following a second breaking wave showed a significant decrease at higher concentrations. The smaller breaking waves increased the area of concentrations up to approximately the 0.0075% band whilst the larger breakers showed reduction of levels nearer the 0.004% level.

Again, this shows that smaller, spilling, breaker may actually cause a greater threat to the environment. Whilst larger plunging breakers cause the general area of the dispersing pollutant to increase, the spilling breakers result in the largest areas of higher concentration.

8.3.3 Centre of Mass Motion

A clear link between breaking wave amplitude and centre of mass motion was discovered for isolated waves.

Whilst this link was difficult to quantify for the second breaker experiments, it was shown that further breaking waves do cause greater centre of mass motion.

8.3.4 Dispersion

For both single and double breaking wave experiments it was shown that non-dimensional breaking wave amplitude had little effect on the standard deviation of the dye patch. The results were similar for both sets of experiment, with only the starting values differing.

8.3.5 Fractal Dimension

The box-counting method of measuring fractal dimension showed the evolution of complexity of the dye-water boundary. It was shown that the results were very sensitive to the threshold value used to determine what was considered to be the boundary.

For both sets of experiments, the smallest breaking waves had the lowest fractal dimensions with the larger waves approaching values of 1.3 or 1.4. It was shown that once this value had been reached it remained approximately constant, implying that there is a natural limit to the scales of mixing that can occur.

8.3.6 Summary of Overall Findings

It has been shown that the dispersion of surface polutants caused by large spilling breakers present potentially the greatest threat to organisms living near, or depending, on the water's surface. These breaking waves disturb the film sufficently to mix it beneath the surface, but without the addition energy required to disperse the higher concentrations. The effect of subsequent similar sized breakers does not greatly help to dilute these levels but simply translated the mixing further downstream.

Large plunging breakers offer the best method of dispersion, reducing the area and depth of highest concentrations and diluting the pollution faster than smaller

waves. The effect is increased by further breaking waves.

8.4 Comparison with Previous Work

Previous work has been carried on isolated breaking waves by Schlicke [67] and Rapp and Melville [59]. The work presented by Schlicke in 2001 looked in detail at only breaking waves with an ak amplitude of 0.324. The results presented in this thesis for amplitudes of 0.320 and 0.327 compare favourable with the results presented by Schlicke. A larger range of experiments are shown in this thesis, with greater detail shown to the different concentration values and effect of amplitude.

Rapp and Melville used food dye to study the dispersion caused by a single breaking wave with amplitude of 0.352. As such, they produced no concentration information or amplitude comparisons but had a greater emphasis on energy flux. The work in this thesis offers an extension of Rapp and Melville's initial experiments by providing a wider range of amplitudes with specific concentration information.

8.5 Future Work

The work shown in this thesis should represent the beginning of further research into this field. A large amount of time was spent in the initial set-up and improve-

ment of the experiment technique and time was lost due to unforeseen events. Therefore, it was not possible to persue the statisical approach that was prefered. Ideally, the number of repeats for every experiment should be increased to remove, as much as is possible, the random effects of the experiment. The PLIF results have presented many interesting relationships that will need a greater depth of experimentation over a wider range of amplitude to investigate further. Investigation of second or multiple breaking waves for larger amplitudes would provide significant extra data to this area of study.

Also, the results presented concentration mainly on the initial and final values of the qualities measured, specifically when examining the centre of mass. Future experimental work should consider the evolution of the quantities over time in greater detail.

The initial plan of the research was to compare the dispersion on single breaking waves in deep water with breaking waves on a shallow beach. However, problems installing the beach into the wave tank prevented this research and caused significant delays. Studying and comparing the dispersion under shallow water breaking waves would have obvious merit and provide a greater understand of dispersion of polutants nearer to the coast. It would also be a benefit to consider the use of salt water, rather than fresh, in these experiments.

The study of the dispersion of surfactant films by breaking waves is essential. It will increase our knowledge of the fate of the massive amounts of pollutants

released into the environment every year and hopefully contribute to greater measures to deal with and prevent the damage they cause. There is a great opportunity and need for further research.

Appendix A

Sample Images from Experiment

This appendix contains sample images from an breaking wave with an ak value of 0.346.

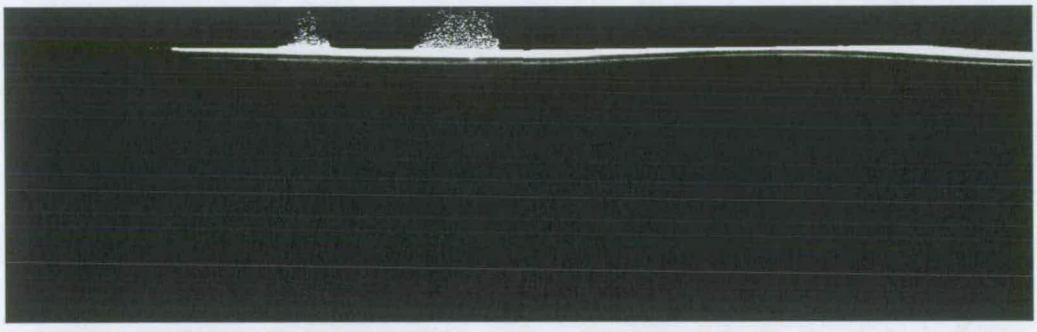

Figure A.1: Half a second before breaking

Initially the water's surface is calm and the dye is undisturbed. The beginning of the breaking wave can be seen on the right hand side of the first image. Surface reflections cause a pair of small bright patches above the waterline. These are

not significant, as the analysis program ignores pixels above the MWL.

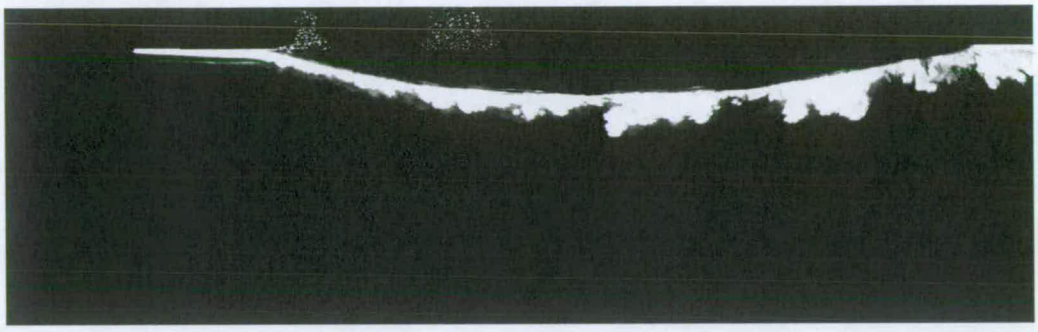

Figure A.2: Two and a half seconds after breaking

Just after the wave has broken, the dye is mixing below the surface, with most areas still at too high a concentration to register exactly.

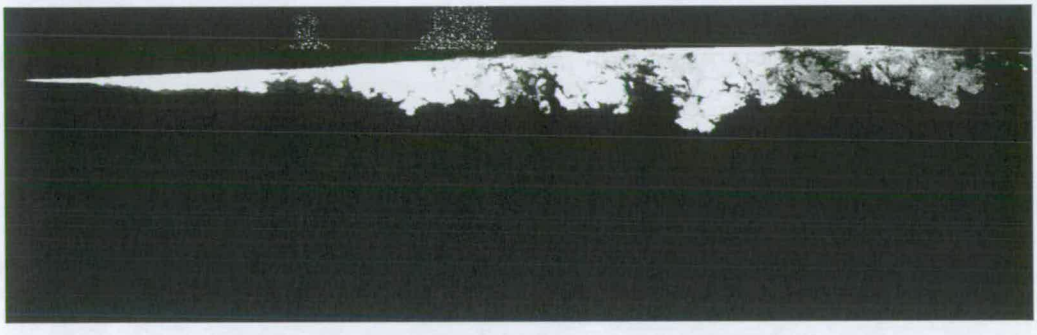

Figure A.3: Four seconds after breaking

Four seconds after the breaking, most of the surface motion has died down and mean water level returns to the same level as prior to breaking. There are still large areas of concentration greater than 0.02%.

Ten seconds after breaking the water surface is completely calm and the mixing is fueled by the motion beneath the surface. The areas of higher concentration

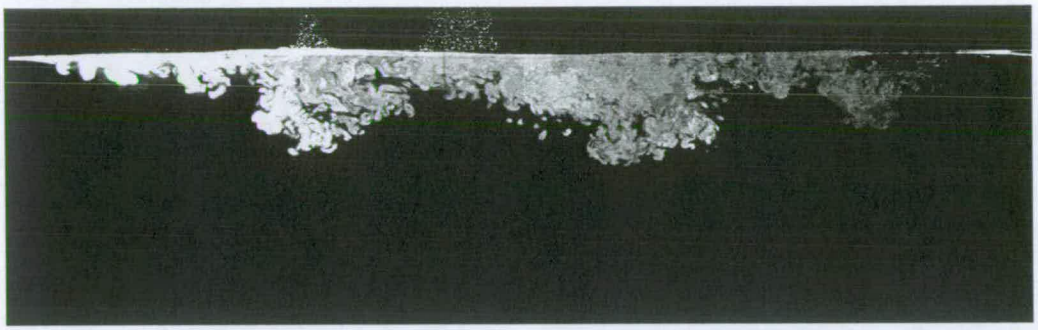

Figure A.4: Ten seconds after breaking

are mainly at the far left of the images, downstream of the breaking point, while the remainder of the dispersion is largely uniform in concentration.

Figure A.5: Fifteen seconds after breaking

A small patch of dye appears detached on the right of the image, driven downwards by a specific eddy. This patch may still be attached to main body of mixing in a plane not illuminated by the laser.

The dye begins to leave the field of view of the cameras and the distinction between medium and low concentrations becomes more obvious.

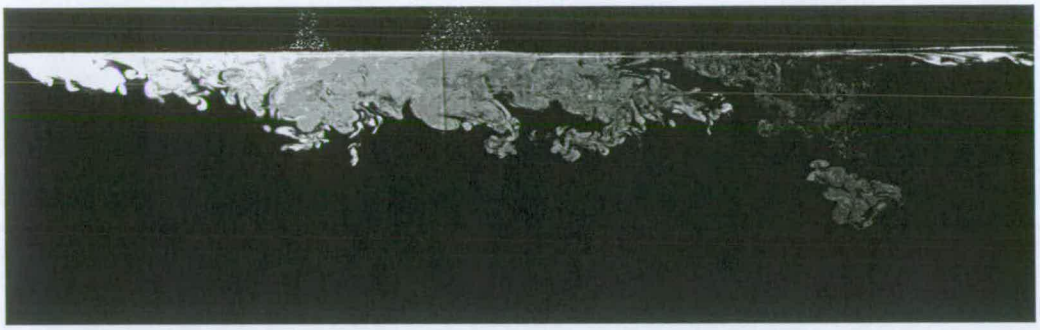

Figure A.6: Twenty seconds after breaking

Figure A.7: Twenty-five seconds after breaking

Finally, there is a clear distinction between concentrations, with the higher values on the left on the image, gradually decreasing until the lower concentrations on the far right drop below measureable values.

Figure A.8: Thirty seconds after breaking

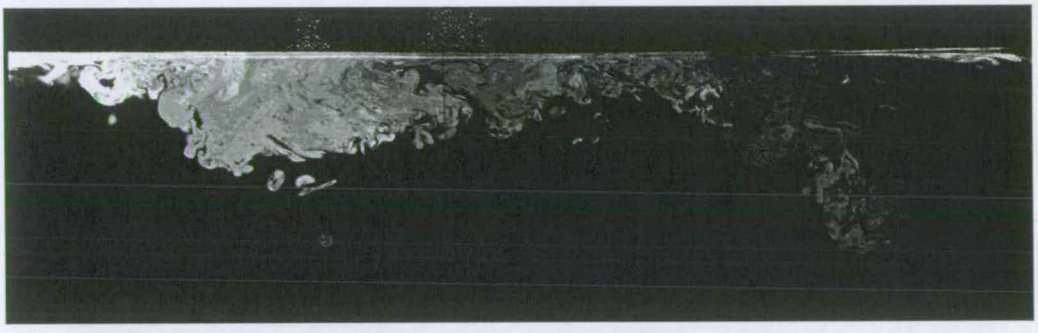

Figure A.9: Thirty-five seconds after breaking

Figure A.10: Forty seconds after breaking

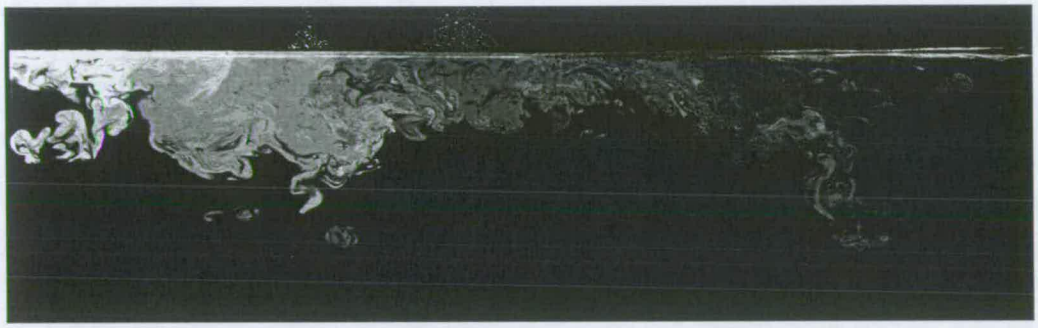

Figure A.11: Forty-five seconds after breaking

Appendix B

Single Breaking Wave Area Results

This appendix contains the area results for a single breaker, as discussed in section 6.4.

Breaker amplitude	Area ($log_{10}k_c^2A$)
0.314	-0.053
0.320	0.046
0.327	-
0.333	0.108
0.339	-
0.346	-
0.352	0.203

Table B.1: 0.0005% Area results

Breaker amplitude	Area ($log_{10}k_c^2A$)
0.314	-0.060
0.320	-0.007
0.327	-
0.333	0.100
0.339	-
0.346	-
0.352	0.203

Table B.2: 0.001% Area results

Breaker amplitude	Area ($log_{10}k_c^2A$)
0.314	-0.170
0.320	-0.032
0.327	-
0.333	0.084
0.339	0.301
0.346	0.379
0.352	0.123

Table B.3: 0.0015% Area results

Breaker amplitude	Area ($log_{10}k_c^2A$)
0.314	-0.233
0.320	-0.052
0.327	-
0.333	0.061
0.339	0.242
0.346	0.305
0.352	0.075

Table B.4: 0.002% Area results

Breaker amplitude	Area ($log_{10}k_c^2A$)
0.314	-0.306
0.320	-0.078
0.327	-
0.333	0.043
0.339	0.171
0.346	0.242
0.352	0.013

Table B.5: 0.003% Area results

Breaker amplitude	Area ($log_{10}k_c^2A$)
0.314	-0.427
0.320	-0.129
0.327	0
0.333	-0.109
0.339	0.084
0.346	-0.167
0.352	-0.364

Table B.6: 0.004% Area results

Breaker amplitude	Area ($log_{10}k_c^2A$)
0.314	-0.506
0.320	-0.219
0.327	-0.127
0.333	-0.231
0.339	-0.191
0.346	-0.637
0.352	-0.568

Table B.7: 0.005% Area results

Breaker amplitude	Area ($log_{10}k_c^2A$)
0.314	-0.652
0.320	-0.349
0.327	-0.378
0.333	-0.621
0.339	-0.803
0.346	-1.123
0.352	-0.929

Table B.8: 0.0075% Area results

Breaker amplitude	Area ($log_{10}k_c^2A$)
0.314	-0.838
0.320	-0.434
0.327	-0.620
0.333	-0.922
0.339	-1.342
0.346	-1.452
0.352	-1.184

Table B.9: 0.01% Area results

Breaker amplitude	Area ($log_{10}k_c^2A$)
0.314	-0.972
0.320	-0.481
0.327	-0.826
0.333	-1.141
0.339	-1.791
0.346	-1.648
0.352	-1.508

Table B.10: 0.0125% Area results

Breaker amplitude	Area ($log_{10}k_c^2A$)
0.314	-1.151
0.320	-0.580
0.327	-1.069
0.333	-1.465
0.339	-2.088
0.346	-1.962
0.352	-1.640

Table B.11: 0.015% Area results

Appendix C

Single Breaking Wave Dispersion Results

This appendix contains the standard deviation graphs for single breaking waves as discussed in section 6.6.

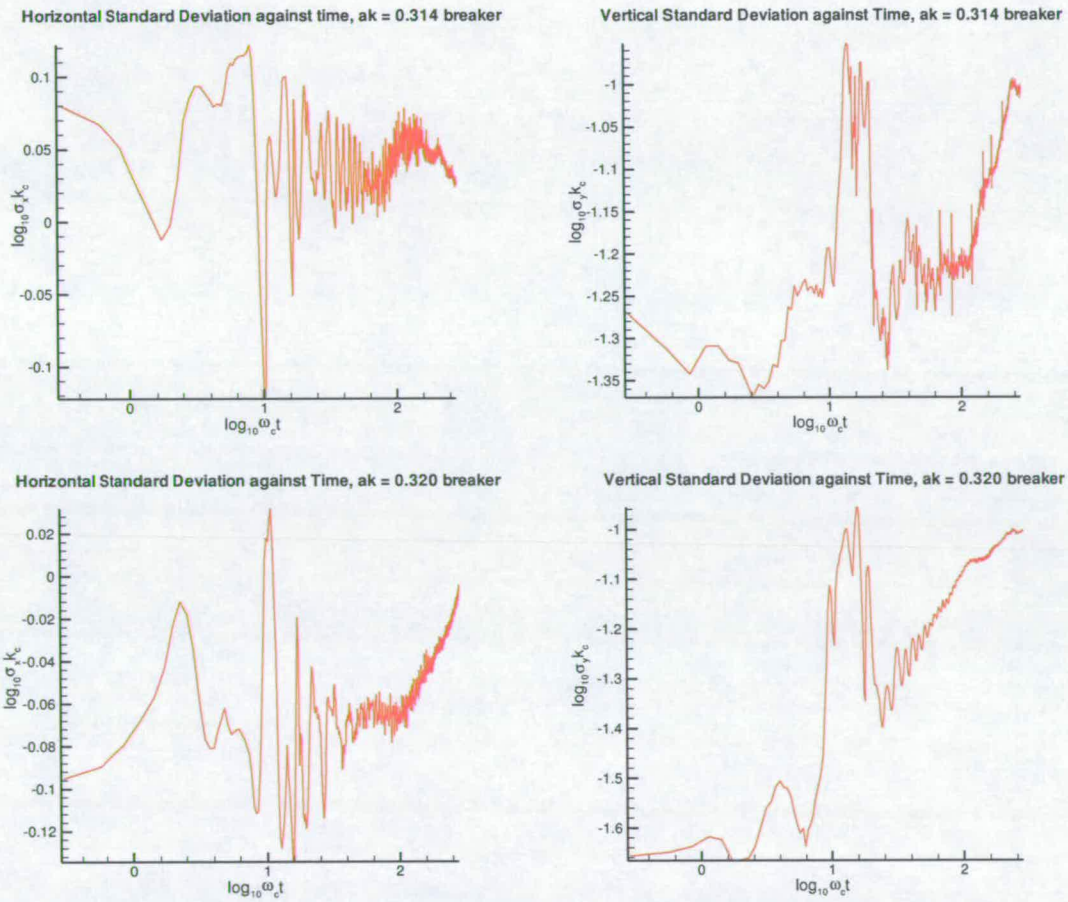

Figure C.1: Standard deviations for single breakers

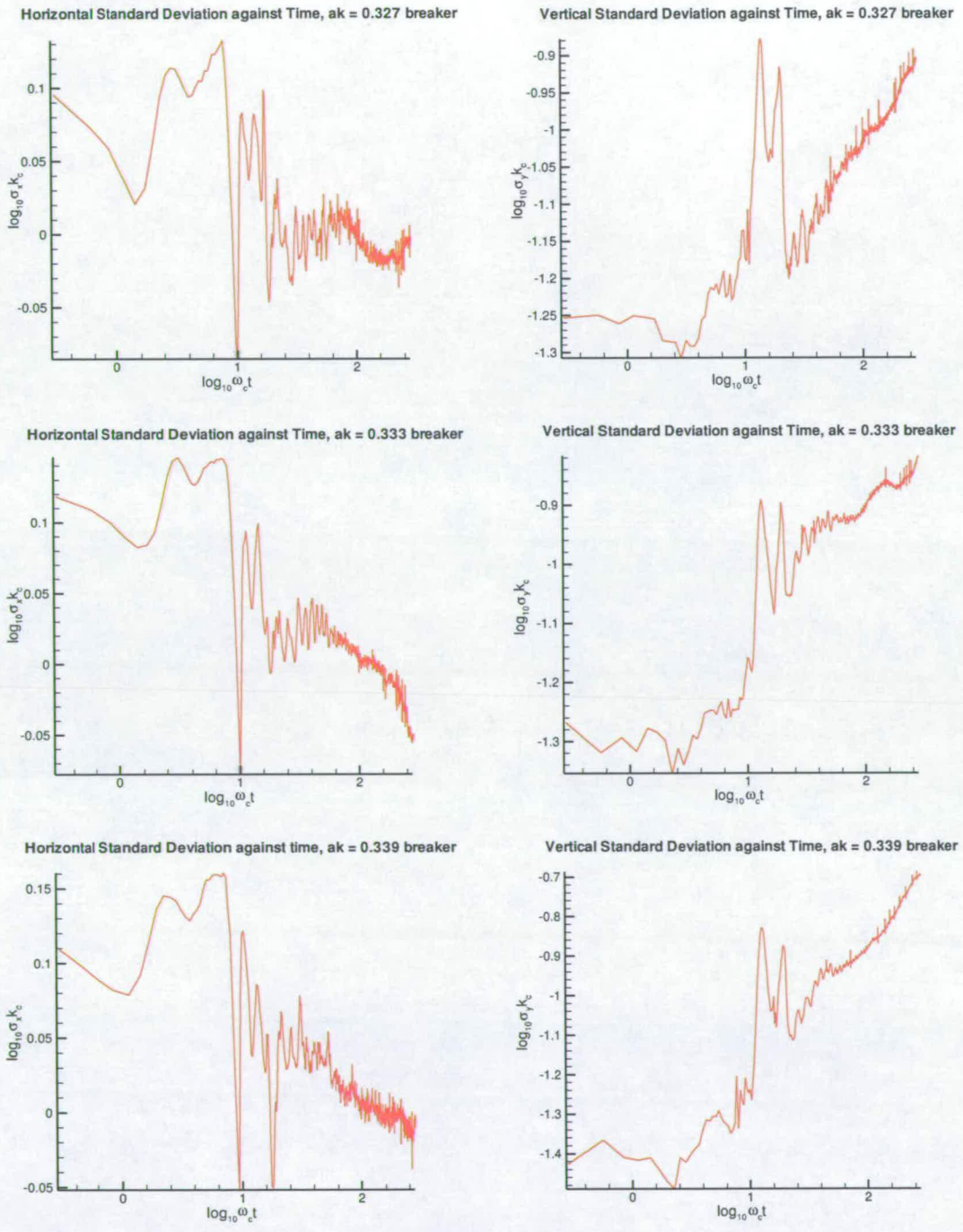

Figure C.2: Standard deviations for single breakers (continued)

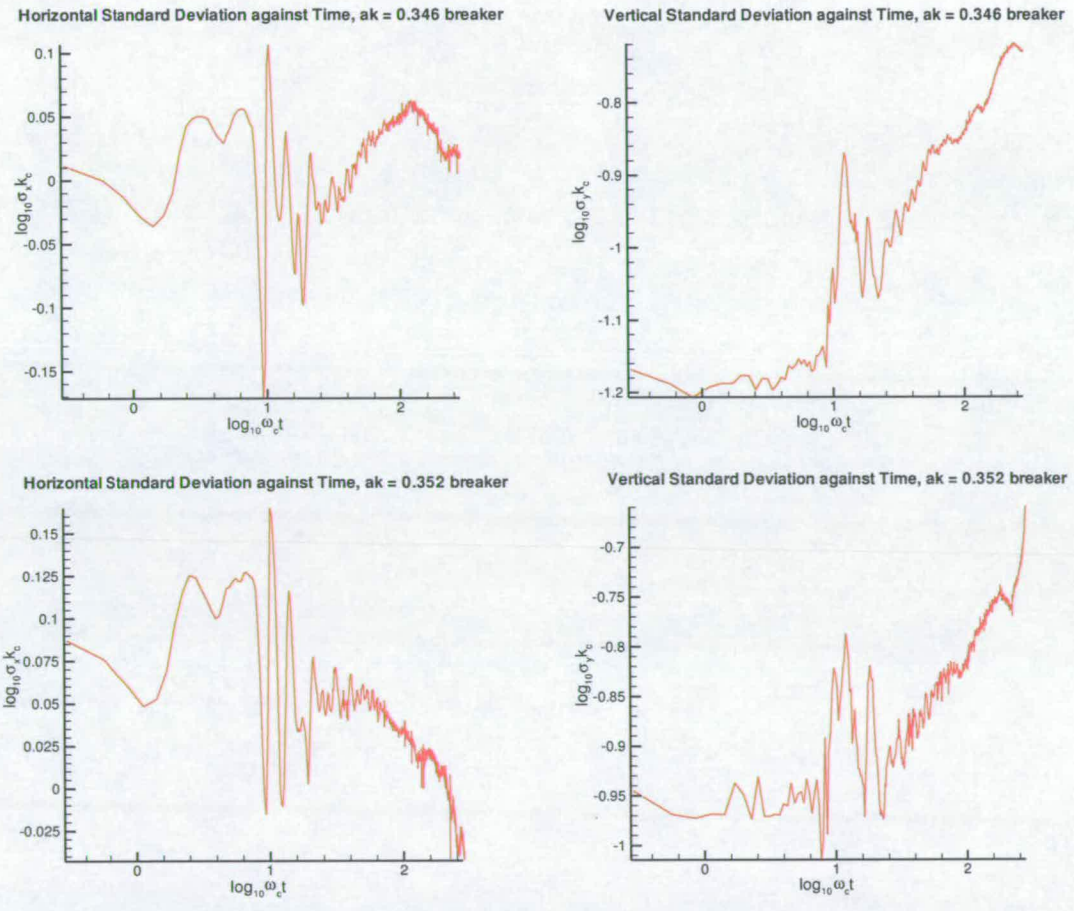

Figure C.3: Standard deviations for a single breakers (continued)

Appendix D

Published Papers and Conference Presentations

Published Papers

"Measuring the dispersion of a surface layer by breaking waves using planer laser induced fluorescence" J. Opt. A 6:627-634, 2004.

INSTITUTE OF PHYSICS PUBLISHING JOURNAL OF OPTICS A: PURE AND APPLIED OPTICS

J. Opt. A: Pure Appl. Opt. **6** (2004) 627–634 PII: S1464-4258(04)72269-2

Measuring the dispersion of a surface layer by breaking waves using planar laser induced fluorescence*

Alan E Marson, Ted Schlicke[1] and Clive A Greated

James Clerk Maxwell Building, The University of Edinburgh, The King's Buildings, Mayfield Road, Edinburgh EH8 9EZ, UK

E-mail: alan@ph.ed.ac.uk

Received 13 November 2003, accepted for publication 20 February 2004
Published 29 April 2004
Online at stacks.iop.org/JOptA/6/627
DOI: 10.1088/1464-4258/6/6/019

Abstract

Surface films can be found all over the world, from the algae blooms of the Mediterranean to oil or sewage pollution near harbours and cities. In this paper the experimental method of planar laser induced fluorescence is used to measure how breaking waves disperse these films.

The method for preparing and extracting quantitative results from laboratory experiments is presented with sample results for depth, area and fractal dimension from mild spilling breakers. Two cases are examined, a single isolated breaker and an identical breaking wave occurring 32 s after an initial breaker has disturbed the film.

Keywords: dispersion, surface films, breaking waves, planar laser induced fluorescence, breakers, spilling, plunging, fractal dimension, box counting dimension

(Some figures in this article are in colour only in the electronic version)

1. Introduction

Surface films can be seen in most ports or harbours. Although the largest causes of surfactants (materials whose properties change at fluid interfaces) are natural [4], substances such as oil and detergent are common sights around waterways used by man. These chemicals lower the surface tension and are spread horizontally by a number of factors. One of the main causes of mixing these films into the body of the water is breaking waves. In these experiments the dispersion of a surface layer of methanol mixed with dye is studied to examine the effect of more than one breaking event on a surface film.

2. Experimental set-up

2.1. Experimental facilities

Whilst the subject of this work is to be applied to natural conditions it was considered impractical to carry out research in the field. Therefore all the experiments are performed in a laboratory wave tank in the James Clerk Maxwell Building of The University of Edinburgh. The tank is 9.77 m long and 0.4 m wide with a working water depth of 0.75 m. The waves are generated at one end by a computer controlled paddle and an absorbing vertical foam beach at the far end prevents reflections.

Breaking waves are created using superposition of linear waves co-ordinated by a dedicated computer running wave software, as described in section 2.2. Planar laser induced fluorescence (section 2.3) experiments are carried out on a thin layer spread on the water surface in the manner described in section 2.4, and illuminated using a scanning beam box (SBB) and argon ion laser (section 2.5). The experimental set-up is shown in figure 1, adapted from [13].

2.2. Creation of waves

Breaking waves are generated by superposition using a band-limited spectrum of frequencies. These waves can be classified by the non-dimensional wave slope, ak_c, where a is the amplitude of the waves and k_c is the wavenumber of the central

* Presented at the Rank Prize Fund Mini-Symposium on Optics in Fluid Dynamics, Meteorology and the Atmosphere, held at Grasmere, UK, on 12–15 August 2002.

[1] Present address: The University of Auckland, Private Bag 92019, Auckland 1020, New Zeland.

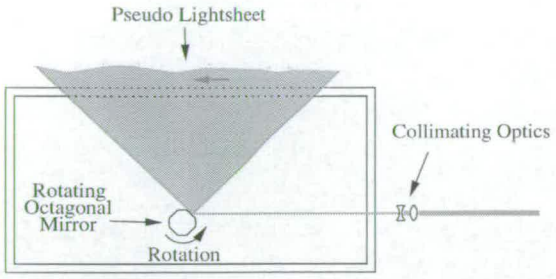

Figure 2. Scanning beam box.

interpretation of concentration maps. Applying the film slowly using a syringe enables precise control over the volume of the film and floats placed on the water's surface control the area covered. The film spreads evenly over the surface to a thickness of 4×10^{-6} m, of the order of a few hundred molecules. A compromise must be made between a film thin enough to be genuinely similar to a surfactant and representative of the field, whilst being thick enough to measure experimentally and track the concentration once dispersed.

2.5. Scanning beam box

Illumination for the PLIF is provided by a scanning beam box (SBB). The SBB consists of collimating optics and a rotating octagonal mirror. The beam passes through a pair of lenses to narrow it to 1 mm diameter before striking one of the facets of the octagonal mirror. As the mirror rotates, the angle of reflection changes and the beam is swept across an arc, as shown in figure 2. The mirror in this case rotated at 150 Hz, creating 1200 sweeps s^{-1}. This is sufficiently fast to produce a constant lightsheet.

2.6. Cameras

A pair of Pulnix TM9701 CCD cameras were used to record the fluorescence. As the ratio of width to height for the mixing process was approximately 2:1, the most efficient coverage is obtained by using two cameras side by side. The cameras have full-frame interline transfer arrays 768 by 484 pixels in size. Digital cameras were used rather than wet film to vastly increase the speed of processing and analysing the data.

The recording time was limited by the amount of RAM available in the computer. Using a PC with a Viper Quad frame grabber and custom software with 1 GB of RAM it was possible to store 2000 images. Images were captured at 20 frames s^{-1} for 50 s.

3. Preparation of images

Before any images can be analysed they have to be pre-processed. This is done in three stages: correcting for lightsheet variation and background; setting up concentration bands and joining the twin images together. All processing is done computationally.

3.1. Lightsheet correction

Because the lightsheet created by the SBB is diverging there is a decrease in intensity at the edges of the sheet. This can be seen (exaggerated in brightness for clarity) in figure 3.

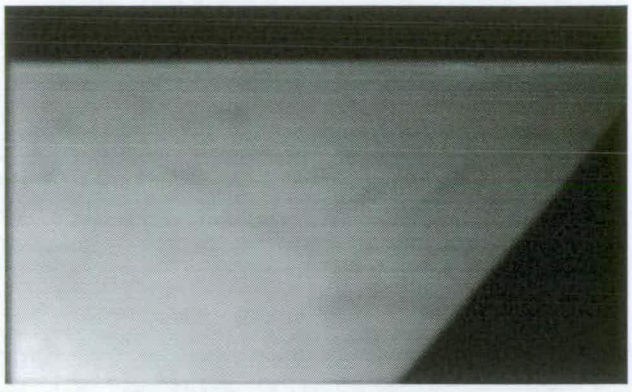

Figure 3. Lightsheet variation.

Table 1. Table of concentration and pixel values.

Concentration (%)	Pixel level
0.02^{+}	255
0.015–0.02	233
0.0125–0.015	212
0.01–0.0125	191
0.0075–0.001	170
0.005–0.0075	148
0.004–0.005	127
0.003–0.004	106
0.002–0.003	85
0.0015–0.002	63
0.001–0.0015	42
0.0005–0.001	21
0.0005^{-}	0

Background images are recorded for both cameras after the experiment has been completed and the dye has been thoroughly mixed. Each experimental image is loaded into the computer memory and every pixel is scaled according to the background image using the following formula:

$$\text{Level} = \frac{\text{Raw level}}{\text{Background level}}\text{Scale}. \qquad (1)$$

The scale factor is chosen to ensure the final image is neither too bright nor too dark, with the smallest concentrations corresponding to nearly black and the largest measured concentrations white.

3.2. Calibration

The following stage in pre-processing is to calibrate the images. In order to account for camera noise and other small variations in intensity on the image, each pixel is set into a concentration band. As the cameras record in eight-bit grey scale, the brightness value for each pixel ranges from 0 to 255. The values and corresponding concentrations can be seen in table 1.

The intensities can be linked to the concentrations using a *calibration vessel* which contains each of the concentrations listed above. By recording an image of the vessel and calibrating each intensity to correspond to the values in table 1, as seen in figure 4, intensities can be directly connected with concentrations for analysis.

in equation (3). For normal Brownian motion $H = \frac{1}{2}$, implying a completely random walk. Using a 1D analogy, a particle starting at the origin can move ± 1 on every time step. For a completely random walk, each movement is entirely independent of the last step. Conversely, if $H < 0.5$ the particle is more likely to make the move opposite to what it did at the last step and if $H > 0.5$ it is more likely to move in the same direction again. The former is known as subdiffusive, or antipersistent, while the latter is known as superdiffusive, or persistent.

The random nature of turbulence means that a specific Hurst exponent of greater or less than 0.5 does not necessarily imply the entire process is sub-or superdiffusive. Therefore, the Hurst exponent will be referred to as a dispersion exponent.

The dispersion exponent and diffusion coefficient can be calculated by taking the logarithm of equation (6) to give

$$\log \sigma = H \log t + H \log(2D) \tag{7}$$

then graphing $\log \sigma$ against log t where the gradient of the slope will be H and the diffusion coefficient given by $\frac{10^{\frac{c}{H}}}{2}$ where c is the intercept.

4.6. *Fractal dimension*

The aim of calculating the fractal dimension is to quantify the activity of the mixing in addition to measuring the dispersion coefficients. A fuller description of the method and concepts can be found in the work of Catrakis *et al* [1] and Prasad and Sreenivasan [9], both of which involve similar turbulent mixing.

The film spreading on the surface of the water creates in essence a 2D object. The intercept between the lightsheet and film is a 1D line. Prior to breaking, the cameras record the straight line intercept. However, once the wave has dispersed the film the outline becomes more complicated. It is no longer one dimensional but does not completely fill the 2D plane of the lightsheet. Therefore it can be described in fractal terms with a dimension somewhere between one and two.

There are many definitions of dimension [12]. The most widely used is the topological dimension, D_t, where D_t is always an integer: zero for a dot, unity for an arc, two for a surface etc. One of the most common other definitions is the *Hausdorff* dimension, D_H. For a full definition see the work of Saupe *et al* [12]. The *Hausdorff* definition can be modified to the *box counting* dimension, D_B, which is far more practical and useful from a computational perspective.

To calculate D_B the image under inspection is covered by a grid, for the case of these $2D_t$ images a square grid, of side length r, and the number of individual grid elements containing a section of outline, N, is counted. The process is then repeated for a range of grid sizes, ideally from approximately the size of the image down to an individual pixel. N and r are related to the *box counting* dimension by

$$\log N = D_B \log\left(\frac{1}{r}\right) + \log H. \tag{8}$$

Therefore D_B can be measured by plotting $\log N$ versus $\log(\frac{1}{r})$.

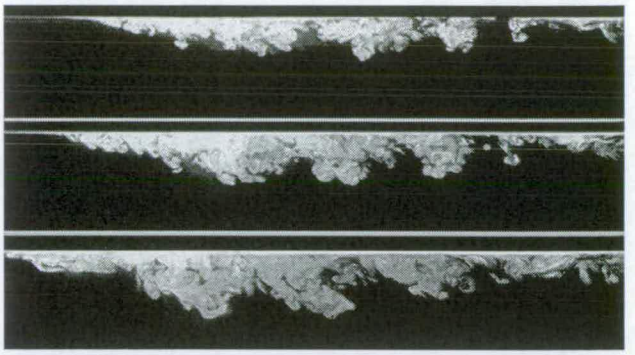

Figure 5. Dye dispersing after 0.320 breaker; 10, 20, 40 s.

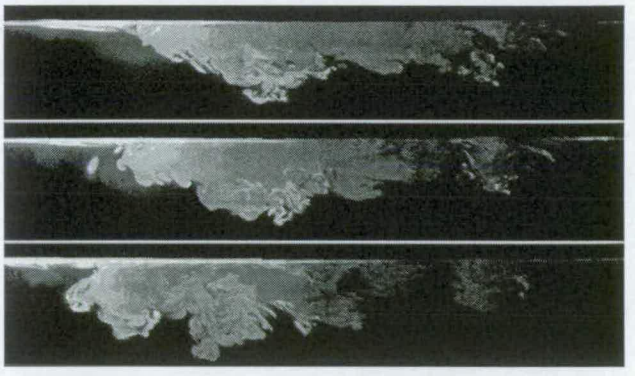

Figure 6. Dye dispersing after a second 0.320 breaker; 10, 20, 40 s.

5. Results

Two waves are looked at in this paper, both with an ak value, defined in section 2.2, of 0.320. These waves are mild spilling breakers, where the crest becomes unstable and spills down the front of the wave.

Sample images from the single breaker taken at 10, 20 and 40 s after breaking can be seen in figure 5, where white represents the highest concentration.

Single isolated breakers are uncommon under natural conditions, therefore the effect of a second breaker is also examined. The second breaker was created exactly 32 s after an initial unrecorded breaker with identical characteristics. Example images can be seen in figure 6.

Experiments have been carried out for a range of wave amplitudes from mild spilling to steep plunging. The results for only the mild spillers are presented here.

Depth, area and fractal dimension results are presented with a comparison between the single and double breakers.

5.1. *Depth*

The maximum depth reached for just three concentrations, for improved clarity, is graphed below in figures 7 and 8. These logarithmic plots are non-dimensionalized with respect to the central wavenumber k_c and its angular frequency ω_c. The breaking event itself occurs at 1 on the non-dimensionalized time axis in both cases. The origin in figure 8 would correspond to a non-dimensional time value of approximately 2.25 in figure 7. This applies to all graphs.

The depth is measured from the mean water level, which creates the large initial motion in the graph. The main region of interest in both figures is the region between 1.1 and 2.4 on the

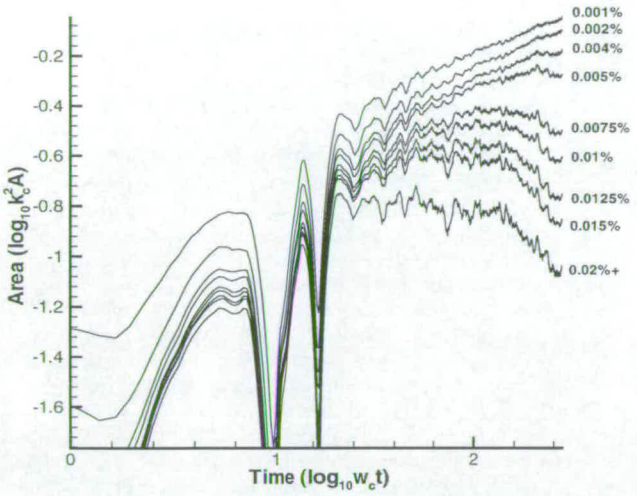

Figure 9. Area against time for a single $ak = 0.320$ breaker.

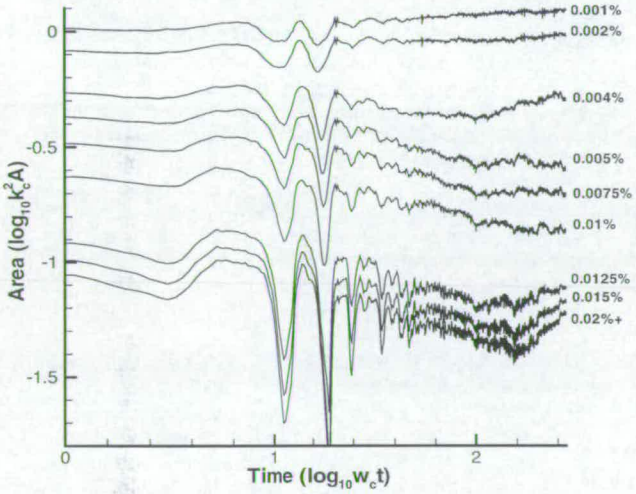

Figure 10. Area against time after a second $ak = 0.320$ breaker.

Again, the end of the single-breaker results maps favourably to the start of the second wave. The areas do not change as significantly as in figure 9, although the general trends are continued to a much lesser extent. However, there is a significant departure at $\omega_c t = 2.2$. This corresponds to the plume mentioned in section 5.1. It appears to be formed from an area with a concentration significantly higher than 0.02% which spreads into measured values.

An important conclusion can be drawn between the increasing depth and comparatively constant total area. The dye tends to move in the wave direction, spreading downwards but also narrowing in width, as can be seen in figure 6. This is confirmed by the centre of mass motion results, not presented in this paper. A second breaker has the effect of transferring the position of the dye but not greatly increasing the speed of the mixing.

5.3. *Fractal dimension*

The fractal dimension of the boundary between the dye and water was calculated using the *box counting* method described in section 4.6. The images are prepared to leave just the outline of the dispersion then the procedure is carried out with ruler lengths between one and the vertical variance. The relationship between $\log N$ and $\log \frac{1}{r}$ can then be calculated computationally to give the fractal dimension for that individual image. This process is repeated for all 1000 images.

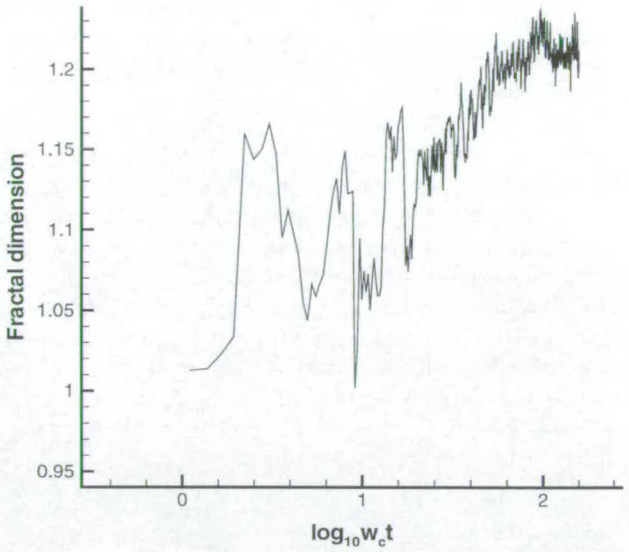

Figure 11. Fractal dimension against time for a single $ak = 0.320$ breaker.

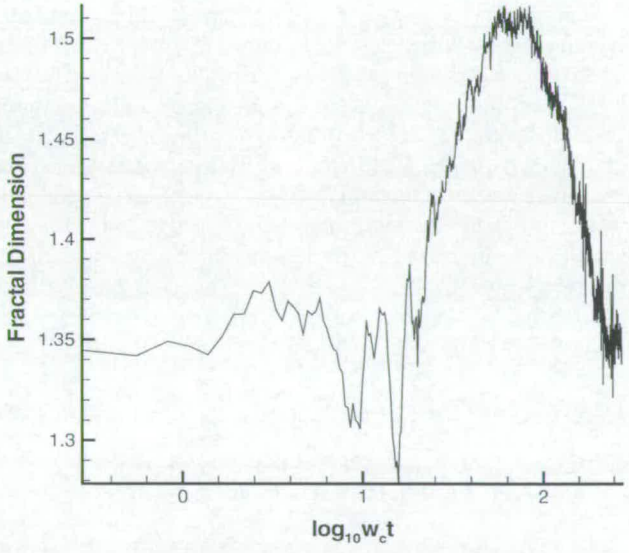

Figure 12. Fractal dimension against time after a second $ak = 0.320$ breaker.

The graphs of fractal dimension against time can be seen in figures 11 and 12.

Prior to breaking in figure 11 the dimension is approximately unity, the dye remaining at rest on the surface. Following breaking the dye patch increases rapidly in area and the fractal dimension grows to a value of approximately 1.22. This is far lower than suggested by the work carried out by Schlicke [13] using a slightly larger breaking wave. Increasing fractal dimension is caused by increasing complexity in the outline of the image. This is related to the development of small

Conference Presentations

Ranks Prize Funds Mini-symposium on Optics in Fluid Dynamics, Meteorology and the Atmosphere, Grasmere, England. *Measurement of the Dispersion of Surface Films by Breaking Waves using LIF.*, 12-15th August 2002.

4th International Symposium on Particle Image Velocimetry, Goettingen, Germany. *Measurement of the Transition from 2D to 3D motion after wave breaking using Dual-Plane Particle Image Velocimetry.* 17-21 September 2001.

14th Annual Scottish Fluid Mechanic Meeting. University of Glasgow, Glasgow. *Breaking Waves and the Dispersion of Surface Films.* 30th May 2001.

Bibliography

[1] P. S. Addison. *Fractals and Chaos.* I.O.P., 1997.

[2] J. Aitken. *On the Effect of Oil on a Stormy Sea.* Proc. Roy. Soc. Edin., 12:56-75, 1883.

[3] W. Alpers and H. Huhnerfuss. *The Damping of Ocean Waves by Surface Films: A New Look at an Old Problem.* J. of Geo. Res., 94:C5, 6251-6265, 1989.

[4] N. F. Barber. *Water Waves.* Wykeham Pub., London, 1969.

[5] D. R. Basco. *A Qualitative Description of Wave Breaking.* J. Water, Port, Coast. and Ocean Eng. 111(2), 1985.

[6] J. A. Battjes, T. Sakai. *Velocity Field in a Steady Breaker.* J. Fluid Mech.,111: 421-437, 1981.

[7] BBC News report. *Action Urged Over Giant Wave Threat* http://news.bbc.co.uk/1/hi/uk/966968.stm, 11/10/2000.

[8] P. Bonmarin. *Geometric Properties of Deep-Water Breaking Waves* J. Fluid Mech, 209:405-433, 1989.

[9] Ch. Bruker. *3-D PIV via Spatial Correlation in a Color-Coded Light-Sheet* Exp. in Fluids, 21, 1996.

[10] J. M. Buick, I. G. Morrison, T. S. Durrani, C. A. Greated. *Particle Diffusion on a Three-Dimensional Random Sea* Exp. in Fluids, 30, 2001.

[11] H. J. Catrakis, R C Aguirre and J Ruiz-Plancarte. *Area-volume Properties of Fluid Interfaces in Turbulence: Scale-Local Self-Similarity and Cumulative Scale Dependence* J. Fluid Mech. 462: 245-54. 2002

[12] M. Chaplin *Water Structure and Behaviour* http://www.sbu.ac.uk/water/.

[13] K.-A. Chang and Liu, P. L.-F. *Velocity, Acceleration and Vorticity Under a Breaking Wave* Phys. Fluids, 10(1), Jan 1998.

[14] J. Cullen. *A Study of Brass Instrument Acoustics using an Artifical Lip Reed Mechanism, Laser Doppler Anemometry and Other Techniques.* Ph.D. Thesis, University of Edinburgh, 2000.

[15] R. David, A Fall and O. Lecoq. *Derivation of supersaturation during precipitation from the mixing pattern of an inert tracer in the same device: case of partially premixed food streams.* Chem. Sci. Eng, 58(2003) 5079-85.

[16] R. G. Dean and R. A. Dalrymple. *Water Wave Mechanics For Engineers ans Scientists* World Scientific, 1993.

[17] L. Debnath. *Nonlinear Water Waves.* Academics Press, London, 1994.

[18] S. Deusch and T. Dracos. *Time Resolved 3D Passive Scalar Concentration-Field Imaging by LIF in Moving Liquids.* Meas. Sci. Tech, 12:188-200, 2001.

[19] S. Deusch, H. Merava, T. Dracos, P. Rys. *Measurement of Velocity and Velocity Derivatives Based on Pattern Tracking in 3D LIF Images.* Experiments in Fluids, 29:288-401, 2000

[20] T.P. Dewhirst. *Multiple CCD Array D.P.I.V.* Ph.D. thesis, University of Edinburgh, 1998.

[21] L. Ding, D. M. Farmer. *Observations of Breaking Surface Waves Statistics.* J. Phys. Ocean., 24:1368 - 87, 1993.

[22] D. G. Dommermuth, D. K. P. Yue, W. M. Lin, R. J. Rapp, E. S. Chan, W. K. Melville. *Deep-water Plunging Breakers: a Comparison Between Potential Theory and Experiments.* J. Fluid Mech., 189:423-442, 1988.

[23] H. Du, R. A. Fuh, J. Li, A. Corkan and J. S. Lindsey *PhotochemCAD: A Computer-Aided Design and Research Tool in Photochemistry.* Photochemistry and Photobiology,68, 141-142, 1998.

[24] K. Dysthe, G. Rovner and Y. Rabin. *Damping of Capillary Waves by Polymeric Monolayers - Comparison with Hydrodynamic Theory.* Journal of Physical Chemistry, 90:3894-3895, 1986.

[25] G. A. Edgar. *Measure, Topology and Fractal Geometry.* Springer-Verlag, 1990.

[26] N. Emarat. *Particle Image Velocimetry Experiments on Surf-Zone Breaking Waves.* Ph.D. thesis, The University of Edinburgh, 2000.

[27] J. Feder. *Fractals.* Plenum Press, New York, 1988.

[28] H. B. Fischer, E. J. List, R. C. Y. Koh, J. Imberger, N. H. Brooks. *Mixing in Inland and Coastal Waters.* Academic Press, Inc., 1979.

[29] B. Franklin. *Of the Stilling of Waves by means of Oil.* Philosophical Transactions, 64:445-460, 1774.

[30] F. Franks. *Water.* Royal Society of Chemistry, Paperbacks Series, 1984.

[31] C. J. Galvin. *Breaker Type Classification on Three Laboratory Beaches.* J. of Geo. Research, 73(12):3651-3659,1968.

[32] G. Gartell, E. J. List and C. D. Winant. *Diffusion and Dispersion in Coastal Waters.* ASCE Journal of Hydroraulic Engineering, 116:1158-79, 1990.

[33] A. Gilpin. *Environmental Impact Assessment.* Cambridge University Press, 1995.

[34] R. M. Harrison. *Pollution: Causes, Effects and Control* The Royal Society of Chemistry, 1996.

[35] K. Herterich and K. Hasselmann. *The Horizontal Diffusion of Tracers by Surface Waves.* J. of Phys. Ocean., 12:704-11, 1982.

[36] P. A. Hwang, D. Xu and J. Wu *Breaking of Wind-Generated Waves: Measurements and Characteristics* J. Fluid Mech, 202:177-200, 1989.

[37] B. R. Kerman and L. Bernier. *Multifractal Representation of Breaking Waves on the Ocean Surface.* J. Geo Research, 99(C8),16:179-96, 1994.

[38] H. Lamb *Hydrodynamics* 6th Edition, Cambridge University Press, 1952.

[39] Pengzhi Lin and Philip L.-F. Liu. *Turbulence Transport, Vorticity Dynamics, and Solute Mixing under Plunging Breaking Waves in Surf Zone.* J. of Geo. Research, 103(C8):15677-15694,1998.

[40] S. Lovejoy. *Area-perimeter Relation for Rain and Cloud Areas.* Science, 216:185-187, 1982.

[41] E. H. Lucassen-Reynolds and J. Lucassen *Properties of Capillary Waves* Advances in Colloid and Interface Science, Elsevier Pub. Company.

[42] J. Lucassen. *Effect of Surface-Active Material on the Damping of Gravity Waves: A Reappraisal* Journal of Colloid and Interface Science, Vol 85(1), 1992.

[43] J. K. Mallory. *Abnormal Waves on the South Coast of South Africa.* Int. Hydro. Rev. 51(2): 99-129 1974

[44] B. Mandlebrot. *How Long is the Coast of Britain?* World Treasury of Physics, Astronomy and Mathematics.,1991.

[45] B. Mandlebrot. *A Multifractal Walk Down Wall Street.* Sci. Amer., 1999.

[46] A. E. Marson, T. Schlicke and C.A. Greated. *Measurement of the Transition from 2D to 3D Motion after Wave Breaking Using Dual-Plane Particle Image Velocimetry* 4th International Symposium on P.I.V., Goettingen, Germany, Sept 2001.

[47] J. L. Marson. *Personal Communication*

[48] Material Safety Data Sheet. *Material Safety Data Sheet for Rhodamine B.* http://www.jtbaker.com/msds/englishhtml/r5400.htm.

[49] Methanex. *Environmental Production and Biodegradation of Methanol.* http://www.methanex.com/fuelcells/environment/biodegradation.pdf

[50] G. P. Mocke. *Structure and Modeling of Surf Zone Turbulence due to Wave Breaking.* J. Geo R. 106(C8). 17,039-57, 2001.

[51] A. S. Ndumu, L. T. Dougan, P. S. Addison, W. M. C. McKenzie and R. Hunter. *Fractal Cracking of Concrete: Parameterization of Spatial Diffusion.* J. of Eng. Mech. 125(6), 1999.

[52] J. V. Pastor, J. J. Lopez and J. E. Julia. *Planar Laser-Induced Floures-cence Fuel Concentration Measurements in Isothermal Diesal Sprays.* Opt. Express., 10(2002), 309-23.

[53] Patuxent Science Notes *DDT and Birds of Prey.* http://members.aol.com/egladvocat/patu_ddt.html.

[54] H-O. Peitgen, H. Jurgens, D. Saupe. *Choas and Fractals: New Frontiers of Science.* Springer-Verlag, 1992.

[55] D. H. Peregrine. *Breaking Waves on Beaches.* Ann. Rev. Fluid Mech. 15:149-78, 1983.

[56] R. R. Prasad and K. R. Sreenivasan. *The Measurement and Interpretation of Fractal Dimensions of the Scalar Interface in Turbulent Flows* Phy. Fluids, A 2(5), 2000.

[57] J. Pullen. *P.I.V. Applied to Wave with Surface Active Films.* Ph.D. thesis, The University of Edinburgh, 1998.

[58] *Pulnix TM9701 Camera Manual*

[59] R. J. Rapp and W. K. Melville. *Laboratory Measurements of Deep-Water Breaking Waves.* Phil. Trans. R. Soc. Lond., A 331(1622):735-800, 1990.

[60] M.Raffel, M. Gharib, O. Ronneberger and J.Kompenhans *Feasibility Study of Three-Dimensional PIV by Correlating Images of Particles within Parallel Light Sheet Planes.* Experiments in Fluids, 19:69-77, 1995.

[61] D. Reuteler. www.visi.com/ reuteler/vinci/eddy.jpg.

[62] L. F. Richardson. *Atmospheric Diffusion on a Distance-Neighbour Graph.* Proc. R. Soc. Lond., Series An, 110:709-737, 1926.

[63] D. Rockliff. *Application of Particle Image Velocimetry to the Measurement of Non-Linear Effects Generated by High-Intensity Acoustic Fields..* Ph.D. thesis, University of Edinburgh, 2002.

[64] D. Rogers and G. Bolton King. *Wave Generation using Ocean and Wave: Version 3.61.* users manual. Edinburgh Designs Ltd, Edinburgh, 1997.

[65] *Royal Commission on Environmental Pollution: Third Report: Pollution in Some British Estuaries and Coastal Waters.* Her Majesty's Stationery office, 1972.

[66] *Royal Commission on Environmental Pollution: Eighth Report: Oil Pollution of the Sea.* Her Majesty's Stationery Office, 1981.

[67] T.Schlicke. *Breaking Waves and the Dispersion of Surface Films.* Ph.D. Thesis, The University of Edinburgh, 2001

[68] T. Schlicke and C. Greated. *Application of Dual-Plane Particle Image Velocimetry to the Measurement of Breaking Waves.* Meas. Sci. Technol. 13:1990-95, 2002.

[69] S. F. Singer [Editor]. *Global Effects of Environmental Pollution.* Symposium organised by the American Association for the Advancement of Science, Dallas, 1968.

[70] D. J. Skyner. *The Mechanics of Extreme Water Waves.* Ph.D. thesis, The University of Edinburgh, 1992.

[71] Smithsonian Institute traveling exhibition. http://seawifs.gsfc.nasa.gov/OCEAN_PLANET/HTML/peril_pollution1.html.

[72] V. L. Snoeyink and D. Jenkins. *Water Chemistry.* John Wiley & Sons, 1980.

[73] I. A. Svendsen and I. G. Jonnson. *Hydrodynamics of Coastal Regions.* Den Private Ingeniorford, Technical University, Denmark, 1980.

[74] G. I. Taylor. *Diffusion by Continuous Movements.* Proceedings of the London Mathematical Society, 20:196-212, 1922.

[75] A. Thomas. *The Interaction of an Internal Solitary Wave with Surface Gravity Waves.* Ph.D. thesis, The University of Edinburgh, 2001.

[76] Colin Thomson. Personal Communication.

[77] F. C. K. Ting and J. T. Kirby. *Dynmaics of Surf-zone Turbulence in a Strong Plunging Breaker.* Coastal Eng. 24:177-204, 1995.

[78] D. J. Tritton. *Physical Fluid Dynamics.* Oxford Sci. Pub., 2nd Edition, 1999.

[79] K. Trulson and K. Dysthe. *Freak-Waves - A Three-Dimensional Wave Simulation.* Twenty-First Symposium on Naval Hydrodynamics, 1997

[80] H. Tsunoda and M. Saruta. *Planar Laser-Induced Fluorescence Study on the Diffusion Field of a Round Jet in a Uniform Counter-Flow.* J. Turbul. 4:, 2-11, 2003

[81] J. Westerweel. *Digital Particle Image Velocimetry - Theory and Application.* Delft University Press, 1993.

[82] C. Willert, M. Raffel and J. Kompenhans. *Particle Image Velocimetry A Practical Guide.* Springer, 1998.

[83] A Wing-Keung Law and H. Wang. *Measurement of Mixing Processes with Combined Digital Particle Image Velocimetry and Planar Laser Induced Flourescence.* Exp. Therm. Fl. Sci.,22(2000), 213-29.

[84] World Meterological Organization. *The Sea-Surface Microlayer and its Role in Global Change.* Gesamp report and studies no. 59, 1995. http://www.gesamp.imo.org/no59/